

AD-A111 506

MISSION RESEARCH CORP ALBUQUERQUE NM  
ELECTROMAGNETIC CHARACTERIZATION OF A MARX PULSE GENERATOR.(U)

F/G 9/5

JUL 81 D V GIRI, F R GRAHAM

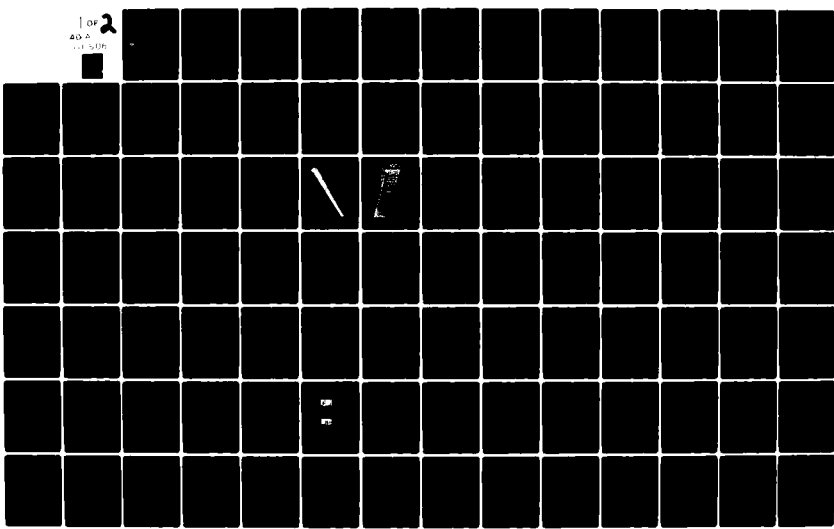
F29601-78-C-0082

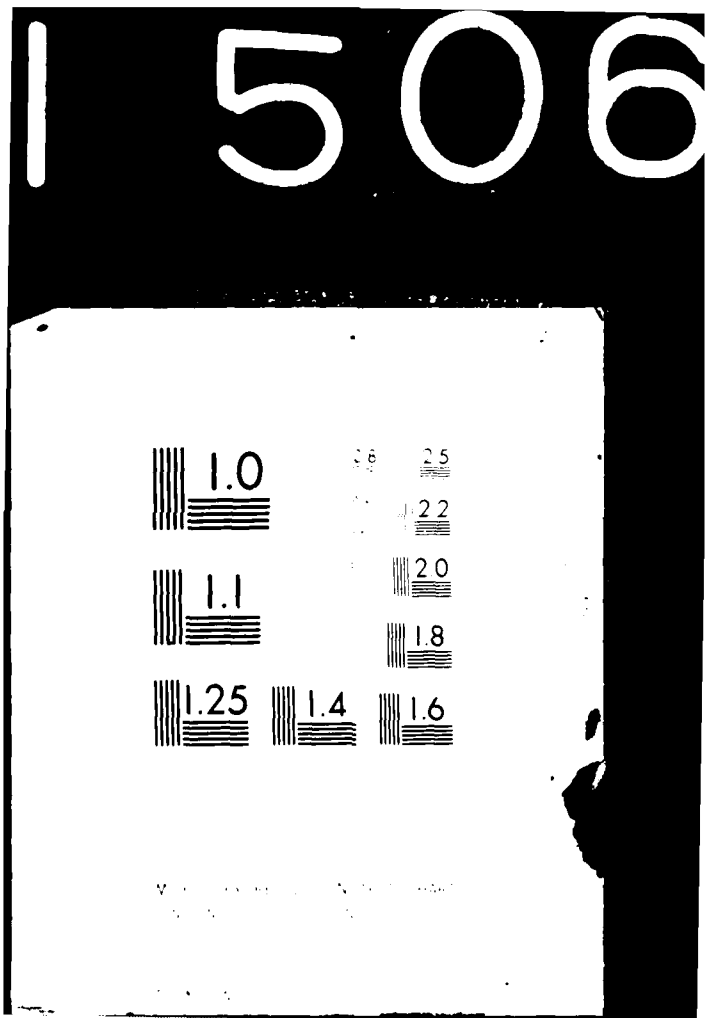
AFWL-TR-81-31

NL

UNCLASSIFIED

1 or 2  
40 A  
1150 ft





AFWL-TR-81-31

AFWL-TR-  
81-31

(1)

ADA 111506

ELECTROMAGNETIC CHARACTERIZATION  
OF A MARX PULSE GENERATOR

D. V. Giri  
F. R. Graham

Mission Research Corporation  
1400 San Mateo Boulevard, SE  
Albuquerque, New Mexico 87108

July 1981

Final Report

Approved for public release; distribution unlimited.

AIR FORCE WEAPONS LABORATORY  
Air Force Systems Command  
Kirtland Air Force Base, NM 87117

BITE fil: COPY

82 03 01 00-5

This final report was prepared by Mission Research Corp, Albuquerque, New Mexico, under Contract F29601-78-C-0082, Job Order 37630132 with the Air Force Weapons Laboratory, Kirtland Air Force Base, New Mexico. Mr William S. Kehrer (NTYEI) was the Laboratory Project Officer-in-Charge.

When Government drawings, specifications, or other data are used for any purpose other than in connection with a definitely Government-related procurement, the United States Government incurs no responsibility or any obligation whatsoever. The fact that the Government may have formulated or in any way supplied the said drawings, specifications, or other data, is not to be regarded by implication, or otherwise in any manner construed, as licensing the holder, or any other person or corporation; or as conveying any rights or permission to manufacture, use, or sell any patented invention that may in any way be related thereto.

This report has been authored by a contractor of the United States Government. Accordingly, the United States Government retains a nonexclusive, royalty-free license to publish or reproduce the material contained herein, or allow others to do so, for the United States Government purposes.

The Public Affairs Office has reviewed this report, and it is releasable to the National Technical Information Service, where it will be available to the general public, including foreign nationals.

If your address has changed, if you wish to be removed from our mailing list, or if your organization no longer employs the addressee, please notify AFWL/NTYEI, Kirtland AFB, NM 87117 to help us maintain a current mailing list.

This technical report has been reviewed and is approved for publication.

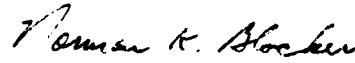


WILLIAM S. KEHRER  
Project Officer



J. PHILIP CASTILLO, PhD  
Chief, Electromagnetics Branch

FOR THE COMMANDER



NORMAN K. BLOCKER  
Colonel, USAF  
Chief, Applied Physics Division

---

DO NOT RETURN COPIES OF THIS REPORT UNLESS CONTRACTUAL OBLIGATIONS OR NOTICE ON A SPECIFIC DOCUMENT REQUIRES THAT IT BE RETURNED.

## UNCLASSIFIED

SECURITY CLASSIFICATION OF THIS PAGE (When Data Entered)

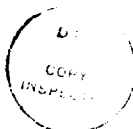
REPORT DOCUMENTATION PAGE		READ INSTRUCTIONS BEFORE COMPLETING FORM
1. REPORT NUMBER <b>AFWL-TR-81-31</b>	2. GOVT ACCESSION NO. <b>AD-A111 506</b>	3. RECIPIENT'S CATALOG NUMBER
4. TITLE (and Subtitle) <b>ELECTROMAGNETIC CHARACTERIZATION OF A MARX PULSE GENERATOR</b>	5. TYPE OF REPORT & PERIOD COVERED <b>Final Report</b>	
7. AUTHOR(s) <b>D. V. Giri F. R. Graham</b>	6. PERFORMING ORG. REPORT NUMBER <b>F29601-78-C-0082</b>	
9. PERFORMING ORGANIZATION NAME AND ADDRESS <b>Mission Research Corporation 1400 San Mateo Blvd, SE Albuquerque, New Mexico 87108</b>	10. PROGRAM ELEMENT PROJECT, TASK AREA & WORK UNIT NUMBERS <b>64711F/37630132</b>	
11. CONTROLLING OFFICE NAME AND ADDRESS <b>Air Force Weapons Laboratory (NTYEI) Kirtland Air Force Base, New Mexico 87117</b>	12. REPORT DATE <b>July 1981</b>	
14. MONITORING AGENCY NAME & ADDRESS (if different from Controlling Office)	13. NUMBER OF PAGES <b>128</b>	
	15. SECURITY CLASS. (of this report) <b>UNCLASSIFIED</b>	
	15a. DECLASSIFICATION/DOWNGRADING SCHEDULE	
16. DISTRIBUTION STATEMENT (of this Report)  <b>Approved for public release; distribution unlimited.</b>		
17. DISTRIBUTION STATEMENT (for the abstract entered in Block 20, if different from Report)		
18. SUPPLEMENTARY NOTES		
19. KEY WORDS (Continue on reverse side if necessary and identify by block number) <b>Marx Generator                          Coupled Transmission-line . tel Pulse Power EM Modeling Peaker Arm Optimization Monocone Switch</b>		
20. ABSTRACT (Continue on reverse side if necessary and identify by block number)  <b>This report reviews the electrical characteristics of the Marx pulser installed in ATLAS I (TRESTLE) facility. Various individual components of the pulser, e.g., monocone switch, central Marx column and peaker arms are studied for their electromagnetic properties. The resulting design curves and tables for peaker arm optimization are presented along with calculated pulser output waveforms for step inputs. Also included is a list of recommendations for future work.</b>		

DD FORM 1 JAN 73 1473 EDITION OF 1 NOV 68 IS OBSOLETE

UNCLASSIFIED  
SECURITY CLASSIFICATION OF THIS PAGE (When Data Entered)

## CONTENTS

<u>Section</u>	<u>Page</u>
I. INTRODUCTION . . . . .	3
II. REVIEW OF ELECTRICAL CHARACTERISTICS OF THE MARX PULSER IN ATLAS I (TRESTLE) FACILITY. . . . .	6
1 Review of Available Documentation. . . . .	7
III. A STUDY OF THE MONOCONE SWITCH . . . . .	12
1 Physical Description of the Monocone Switch. . . . .	13
2 Monocone Impedance . . . . .	15
3 Interfacing with the Marx and Peakers. . . . .	21
4 Recommendations. . . . .	21
IV. PEAKER ARM OPTIMIZATION. . . . .	25
1 Peaking Capacitor Arm Description. . . . .	28
2 Multiconductor Transmission-Line Model of Peakers and Marx. . . . .	35
3 Constraints in Multiconductor Model Leading to Two-Conductor Model . . . . .	46
4 Optimal Positioning Based on Conformal Transformation . . . . .	51
5 Numerical Results. . . . .	54
V. STUDY OF THE COUPLED TRANSMISSION-LINE MODEL . . . . .	58
1 Two Velocities . . . . .	58
2 Waveform Optimization. . . . .	59
3 Optimum Number of Peakers. . . . .	59
VI. RECOMMENDATIONS FOR FUTURE WORK. . . . .	64
REFERENCES . . . . .	68
Appendix A Analysis of Trestle Peaking Capacitors Over the Frequency Range of 1 to 100 MHz . . .	70
Appendix E Low Voltage Spring Tests . . . . .	87



Accession For	
NTIS CTR&I	<input checked="" type="checkbox"/>
DEIS TAG	<input type="checkbox"/>
University and Institutional	<input type="checkbox"/>
Journals	<input type="checkbox"/>
Books	<input type="checkbox"/>
Periodicals	<input type="checkbox"/>
Microfilm	<input type="checkbox"/>
Microfiche	<input type="checkbox"/>
Codes	<input type="checkbox"/>
Plans	<input type="checkbox"/>
Industrial	<input type="checkbox"/>
Other	<input type="checkbox"/>

A

## I. INTRODUCTION

In attempting to determine the hardening of aerospace systems to a nuclear electromagnetic pulse (EMP) environment, it is mandatory to perform system level tests using a simulated environment. For such tests, it is important that the electromagnetic field within the simulator be comparable to the EMP threat, in order to ensure a reasonable amount of confidence in the experimental results. There are a number of factors which influence the behavior of the simulated electromagnetic field including the physical design of the simulator and the design of the pulsers which provide the transient energy to the simulator.

Attention is focused on the Marx type of pulser as installed in the ATLAS I (TRESTLE) facility. Individual components of the pulser are considered for their electromagnetic properties, with the goal of presenting curves and data which would be useful for improving existing pulsers or fabricating new ones.

Traditionally, the pulsers for EMP simulators have been developed and built by researchers and practitioners of the science of high-voltage engineering. Like any other electrical source, a pulser delivers maximum energy into a matched load. In the present situation, the load is a two-parallel-plate transmission line type of EMP simulator, with a nominal input impedance that is dominated by the principal TEM mode of propagation. Although the simulator viewed as a transmission line can and does support non-TEM modes (e.g.,  $\text{TM}_{01}$  mode propagation in the ALECS facility), the input impedance of the simulator is still mainly governed by the TEM wave because the non-TEM modes (TE or TM) are evanescent near both ends of the simulator.

So fortunately, the load into which the pulser delivers transient energy is a quantity that is known fairly accurately and it is mainly resistive. For example, ATLAS I (TRESTLE) facility has a principal TEM characteristic impedance  $Z_C^{TEM}$  of 150 Ω. By replacing the simulator per se with a predominantly resistive load, one can begin to focus attention on the various pulser components.

In general, the performance characteristics (e.g., TEM, TE, TM modes in cylindrical and conical regions, field mapping, terminator effectiveness) of the simulator proper is much better known (Ref. 1) than the performance characteristics of the pulse generator. Some of the pulse power issues relating to the electromagnetic aspects of pulsers are long standing and have been identified (Ref. 2). Appendix A of Reference 2 contains a problem list relating to pulser design, nearly all of which remain to be addressed. With regards to the availability of pulser test results, they tend to be scattered in reports written by the manufacturers of the pulse generator and not readily accessible. Some sample pulser output waveforms as measured in the PTF were reproduced in Reference 3 and used in estimating the transient electric field waveform in the working volume of ATLAS I (TRESTLE) facility. The 10 to 90% rise time  $t_{10-90}$  is typically in the vicinity of 20 ns. It is noted that some of the relations between various rise time definitions have been worked out by Castillo et al.(Ref. 4). Some of the environmental improvements in the working volume of ATLAS I (TRESTLE) facility, derivable from potential pulser improvements (e.g., reducing the rise time by a factor of 0.5, 0.25) were considered in Reference 5. Subsequently, the pulse power related problems list of Reference 2 was selectively updated in Reference 6 and the two important problem areas are: (a) electromagnetic optimization of the switch geometry and (b) electromagnetic optimization of the relative orientation or positioning of Marx and peaking capacitor arms.

Under the present effort, these two problems relating to pulser design are addressed in detail. It is emphasized that by no means all of the pulse power issues have been resolved and many research studies combined with engineering modifications remain to be done. In Section II, the electrical characteristics of the Marx pulser as installed in the ATLAS I (TRESTLE) facility is reviewed. The monocone switch impedance and ways of increasing it to provide better wave transport properties are considered in Section III. Section IV deals with the peaker arm optimization study, resulting in design tables which enable one to determine the optimum positions of a given number of  $N_p$  of peaking capacitor arms. This optimization, based on the method of conformal transformation, does not, however, indicate what the optimum value of  $N_p$  should be. In Section V, a simple 2-wire coupled transmission line model is developed, and typical pulser output waveforms are computed for step function inputs for varying values of  $N_p$ . These waveforms provide a means of selecting an optimum number of peakers.

It is observed that, although the two important problems of switch geometry and peaker arm optimization are considered here, several other related issues remain for future and on-going efforts. Keeping this in mind, Section VI lists a number of recommendations for future analytical and experimental studies. The report is concluded with a list of references and two relevant appendices from previously published work, for the sake of completeness.

## II. REVIEW OF ELECTRICAL CHARACTERISTICS OF THE MARX PULSER IN ATLAS I (TRESTLE) FACILITY

The ATLAS I or TRESTLE pulser consists of two 5 MV pulser modules. One is mounted on each side of the ground plane wedge (GPW) of the simulator facility. The pulser modules are charged to opposite polarities and when fired launch an electromagnetic wave into the conic transition on each side of the GPW. When the wave propagates to the end of the GPW the two waves add across the parallel plate section of the simulator to provide the appropriate EMP environment in the working volume.

The two pulser modules are identical electrically and for the purposes of this report the characteristics of one module will be discussed. When considering only one module the simulator is also split at the plane of symmetry and the pulser module evaluated in terms of driving a  $150 \Omega$  transmission line.

With the exception of one analysis effort that was started on the peaking capacitors and not completed, all information that exists on the pulser modules has been published in the form of reports and/or drawings. All of the available reports and drawings have been reviewed for content that would be of value toward future analysis of the electrical and electromagnetic characteristics of the pulser module. It is not the intent of this report to duplicate the existing data and documentation except where necessary for a point of discussion. The reports that were reviewed are listed in Section II and a general discussion of their content presented.

In general, some work and analysis have been accomplished in the past towards identifying the cause of existing performance problems. Most of the past efforts have approached the problem by evaluating circuit models or using empirical testing. A thorough and comprehensive analysis of the pulser module as

an electromagnetic structure has not been accomplished. This type of analysis is needed to determine what improvement could be expected by various modifications to the modules.

#### 1. Review of Available Documentation

Available documentation covers the original design of the pulser modules, testing of the prototype, and the manufactured configuration of the hardware.

#### DESIGN

Only two reports are available which are related to the final design of the pulser modules. Both reports contain information that is of value toward electromagnetic analysis of the pulser module.

The MLR-294, dated 30 April 1975, was the final design analysis report covering the pulser modules. Section 3 of the report covers the pulser modules but only pages 3-1 through 3-21 may be of value in support of electromagnetic analysis. Table 3-1, page 3-5, lists the key electrical parameters of the pulser module. This table is repeated in Table 1 of this report for easy reference. Item 19 of this table was the calculated rise time of the original bicone output switch. This switch was replaced with a monocone with an impedance of 88  $\Omega$ .

The BDM/A-27-75 dated 11 March 1975 covers an equivalent circuit model of the pulser module for analysis. The circuit model was extensive and distributed to more closely approximate the real case. Many parameters of the model were varied and the predicted performance compared with actual performance measured from the prototype pulser module in the Pulser Test Fixture (PTF). The agreement between predicted and measured

TABLE 1  
PULSER MODULE ELECTRICAL PARAMETERS

1.	Marx Voltage ( $N \times V_C$ )	5.05 MV
2.	Module Voltage	5 MV Nominal
3.	Module Capacitance	3.17 nF
4.	Module Energy Storage	40.4 kJ
5.	Number of Marx Stages (N)	50.5
6.	Capacitance per Stage	0.160 $\mu$ F
7.	Energy per Stage	800 J
8.	Maximum Stage Voltages	100 kV
9.	Module Impedance	150 $\Omega$
10.	Marx Generator Inductance	5.05 $\mu$ H
11.	Total Peaking Circuit Inductance	9.4 $\mu$ H
12.	Peak Current	36.1 kA
13.	Charge Transfer per Switch	0.016 C
14.	Number of Peaking Capacitor Assemblies	4
15.	Total Peaking Capacitance (including strays)	345 pF
16.	Ratio of Marx Capacitance to Peaking Capacitance	9:1
17.	Peaking Capacitor Open Circuit Ring Period	339 ns
18.	Output Switch Closed on Rise of Peaking Capacitor Waveform at	91 ns
19.	Output Switch Risetime 10-90% (into 125 $\Omega$ )	7.3 ns
20.	Prepulse	27 %

performance appears to be fair. The results given for varying the peaking capacitance may be misleading (Page IV-38, Para. 2.2.3). Point capacitors were used in the model based on an earlier test of point capacitors versus distributed capacitors for the Marx capacitors. In this case, however, the high frequency performance of the module is strongly dependent on the characteristics of the peaking capacitors. In the real case the peaking capacitors are made of windings that look like short transmission lines at high frequencies and can severely attenuate some frequencies. Not including this into the circuit model may result in predicting better performance than can be realized. While this type of circuit model is of value for predicting electrical performance of a circuit, it does not predict electromagnetic performance very well. There are reflection and diffraction points in the module geometry that have a strong influence on high frequency performance that the circuit model analysis does not evaluate.

The MLR-483, dated November 1975, reports the results of the prototype pulser module testing in the PTF. The report includes test results with oscilloscopes for the entire test program. The performance measured in the PTF is representative of what can be expected from the pulser modules in ATLAS I (TRESTLE) facility. The PTF introduced some problems due to geometry that will not be present in the horizontal simulator. The diffraction points where the prototype attached to the ground plane and transmission line in the PTF will be different in the horizontal simulator. The point on the ground plane will be eliminated and the angle where the output transition connects to the transmission line will be reduced. These differences should result in slightly better high frequency performance of the pulser module in the ATLAS I (TRESTLE) facility. Appendix D of this report covers what was called "Low Voltage Spring Tests."

The low voltage tests evaluated the pulser geometry with the output switch and peaking capacitor simulated using metal conductors. The reflection and diffraction points within the geometry were clearly visible in the test data. Tests were accomplished with both the bicone and monocone output switch (Appendix B).

In addition, another series of reports called TRETMS exist, which provide some information that is of value in further electromagnetic analysis. The TRETMS were TRESTLE technical memorandum used to document specific problems and tests and analysis efforts during the design and test of the pulser modules. Those TRETMS of specific interest are:

Number 3 - Calculations of Circuit Values and Prepulse.

This TRETM analyzes the difference between the amount of prepulse predicted in the initial design calculations and that actually measured from the prototype pulse module during PTF testing.

Number 5 - Qualitative Comparison Between the Bicone and Monocone Output Switches with Respect to Reflections and Diffractions that May Decide Risetime Performance.

This TRETM defines the two switch geometries and identifies the discontinuities that can cause rise time degradation.

Number 11 - Experimental Investigation to Provide Test Data For Analyzing the Electrical Characteristics of the TRESTLE Peaking Capacitors.

This TRETM provides a significant amount of data on the performance of the peaking capacitors in a transmission line over the frequency range of 0.1 to 110 MHz. The data shows a severe attenuation of frequencies at about 13 MHz and 67 MHz.

Number 12 - Analysis of TRESTLE Peaking Capacitors Over the Frequency Range of .1 to 110 MHz.

This TRETM was not completed due to the author dropping out of the program as a result of an accident. However, the work that was done is included as Appendix A of this report.

Number 13 - Experimental Investigation of Output Waveform Notch.

This TRETM presents data from a series of peaking capacitor configurations on the prototype pulser. These tests were accomplished to assess the possibility of reducing the notch after peak on the output waveform by reconfiguring the peaking capacitors.

Number 16 - Analysis of the Experimental Data Concerning the Waveform Notch.

This TRETM evaluates the results of the tests reported in TRETM Number 13.

The TRETMs not mentioned previously deal with areas not related to electrical performance and would be of no value toward electromagnetic analysis.

In addition to the documentation discussed, a complete set of drawings is available at the simulator facility. These drawings document the physical configuration of the pulser modules and the geometry of the interface with the ATLAS I (TRESTLE) facility.

### III. A STUDY OF THE MONOCONE SWITCH

In Section II, the results of a review of the electrical characteristics of the various components of Marx type of EMP pulse generator was reported. This served the purpose of identifying and to some extent, documenting the salient features and the electrical parameters of various pulser components. This section will review the switch assembly and present the monocone switch analysis, in a self-contained format.

It is well known that the ATLAS I or TRESTLE pulser consists of two 5 MV pulser modules, mounted on each side of the ground plane wedge. It is immediately seen that the base of the pulser takes the form of a monocone over a ground plane. Furthermore, the entire pulser assembly, including the Marx, the peakers and the switch is effectively a section of transmission line that guides the simulation pulse. A necessary but not sufficient requirement, therefore, is that every individual section of this transmission line must have the same characteristic impedance. This is a primary criterion for minimizing the reflections in the simulation process, even before any test object is introduced in the working volume. Other considerations include ensuring minimal field discontinuities between adjacent pulser sections, as well as minimizing the back radiated, and consequently wasted, energy. In some instances, it may be impossible to meet these requirements because of mechanical or practical constraints. However, attempts must be made to minimize impedance and field discontinuities, so that the pulser can propagate and launch a simulation pulse with tolerable amounts of ringing and wasted energy. Attention will be focused on the impedance matching.

Related, relevant work in the past was reported in Reference 7. They have produced quantitative data on the TEM characteristic impedance  $Z_c$  of a tilted monocone, the EM field distribution over spherical wave-fronts, and certain upper bounds on the back radiated energy from the cone.  $Z_c$  has been computed essentially by the method of stereographic projection (Refs. 8 & 9) which reduces the 3-dimensional Laplace equation over a spherical surface to the usual 2-dimensional form. The computations are for a tilted monocone on a flat horizontal ground plane. A later section will address the utility of the reported results to the present case of the monocone at the base of the Marx pulser in ATLAS I or TRESTLE facility. Before discussing the issue of monocone impedance, the following subsection contains a physical description of the monocone switch as it is presently configured in the simulator.

#### 1. Physical Description of the Monocone Switch

Historically, the earlier design of the pulser included a bicone output switch. At the time of testing in the PTF, the rise time measured was three to four times longer than what was predicted for the bicone. After some additional testing and analysis, it was concluded that the rise time was degraded because of the bicone switch geometry and, hence, a monocone switch was designed so that it can be housed in the same fiberglass housing.

The monocone switch design is shown in Figure 1, and it consists of a single cone over a ground plane forming a monocone antenna. The half cone angle is  $20^\circ$ , which when used in

$$Z_c = \frac{Z_0}{2\pi} \ln [\cot (\theta/2)] \quad (1)$$

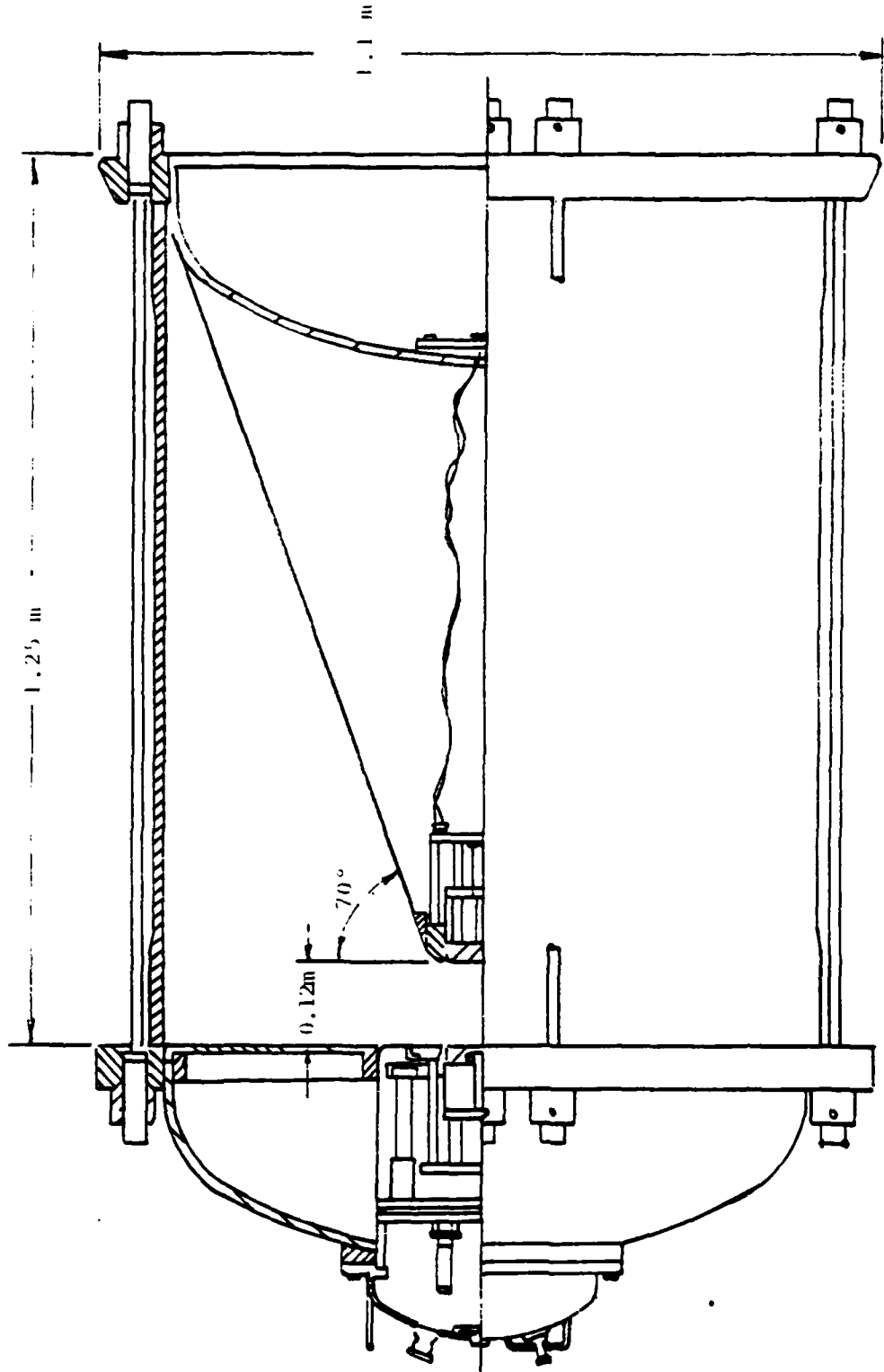


Figure 1. Schematic of the monocone output switch for the 5 MV Marx pulser.

gives a characteristic impedance of  $104 \Omega$ . In Equation (1), which is well-known (Ref. 10).

$Z_0 \equiv$  free space characteristic impedance  $\approx 120 \pi \Omega$

$\beta \equiv$  half angle of the monocone

Although, the monocone is immersed in an SF<sub>6</sub> medium, the electrical parameters ( $\epsilon_{SF_6} \approx \epsilon_0$ ;  $\sigma_{SF_6} \approx 0$ ) are similar to that of free space. This 104  $\Omega$  cone uses a modified edge/plane spark gap geometry and the switch pressure can be varied from 0 psig to 150 psig, but in practice it is held constant at 100 psig. The switch electrode extension can range from -0.09m to + 0.045m, whereas the switch gap itself has a range of 0.075m to 0.12m. The monocone switch electrode is electrically in contact with, and mechanically attached to the Marx generator and the peaking capacitor arms. The transition between the switch and the Marx/pulser assemblies is sketched in Figure 2. From a cursory examination of this transition, it is observed that even if one has an impedance match at this transition, the field mismatch can be quite large. However, as was indicated earlier, the subject of field matching is postponed until a satisfactory transmission line model is developed and analyzed for the central Marx column and the peaker arms above a ground plane. For the present, we consider the impedance related issues and ways of improving the impedance matching; i.e., how to get the cone impedance to approximately equal 150  $\Omega$ .

## 2. Monocone Impedance

A tilted monocone shown in Figure 3 was analyzed in Reference 7 for its TEM wave propagation characteristics. With reference to the figure,  $\beta$  is the half cone angle and

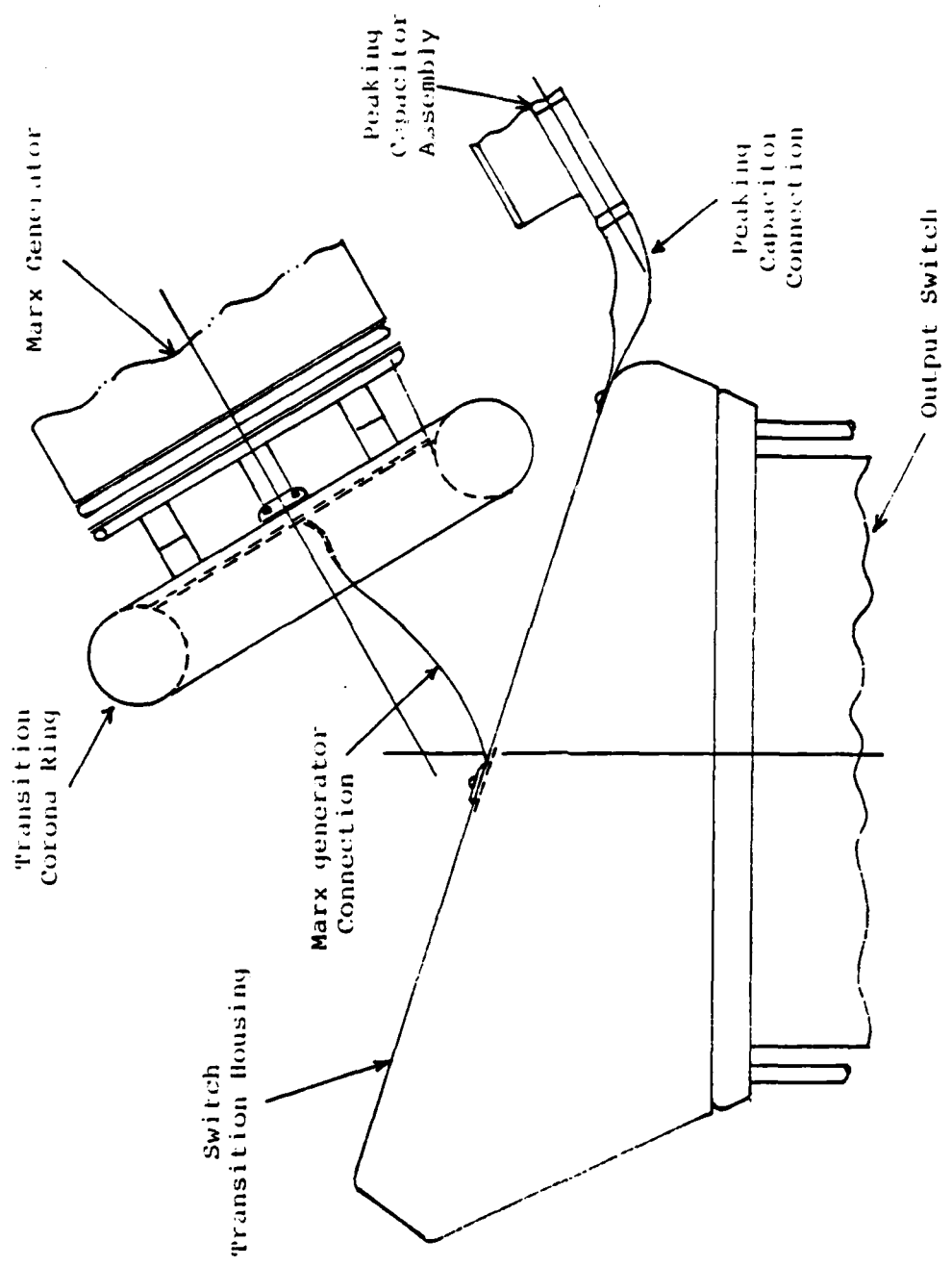
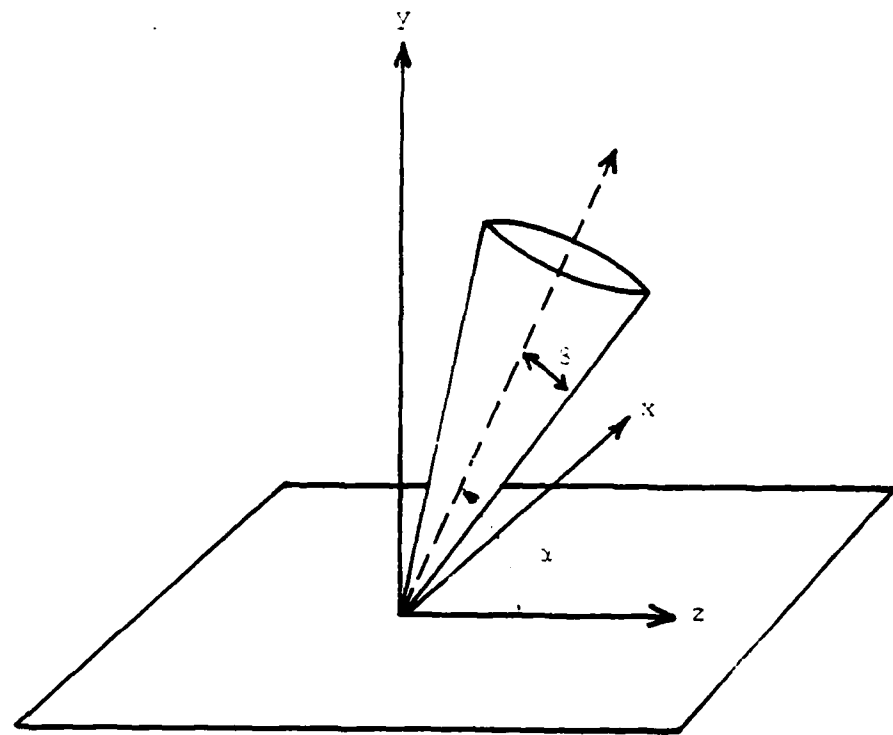
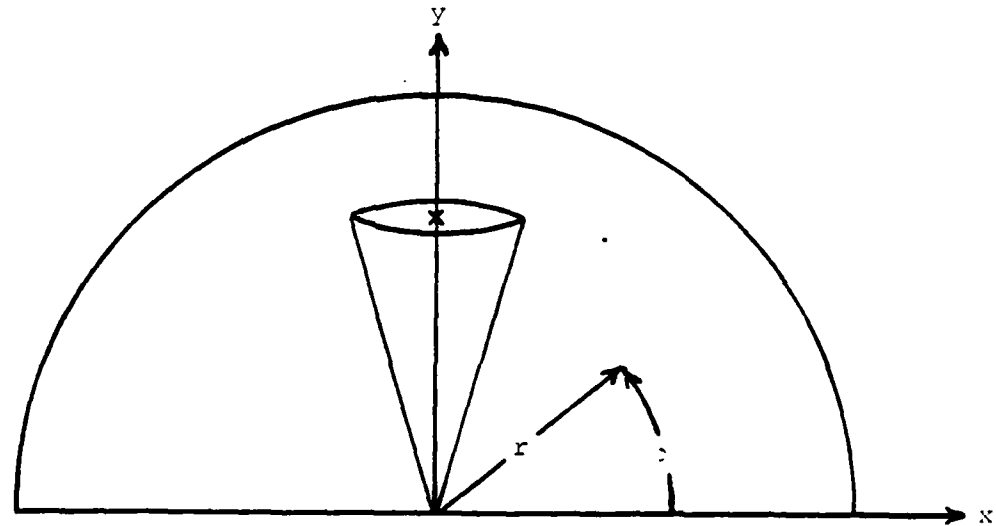


Figure 2. Schematic of the transition between the output switch and the Marx generator.



a) Side View



b) Front View

Figure 3. A tilted monocone over a horizontal ground plane.

$\alpha$  denotes the angle made by the cone axis with the ground plane. A pair of rectangular ( $x, y, z$ ) and spherical ( $r, \theta, \phi$ ) coordinate system is also illustrated. This structure is a radial transmission line and, hence, its TEM characteristics are determined by solving a surface Laplace equation over a spherical surface orthogonal to the direction of wave propagation. By using a method of stereographic projection, Reference 7 derives the characteristic impedance of such a structure to be

$$z_c^{(\text{tilted})} \approx \frac{z_0}{2\pi} \operatorname{arccosh} \left[ \frac{\sin (\alpha)}{\sin (\beta)} \right] \quad (2)$$

It is seen that, in the case of no tilt, i.e.,  $\alpha = 90^\circ$ , equation (2) reduces to

$$\begin{aligned} z_c &\approx \frac{z_0}{2\pi} \operatorname{arccosh} [\csc (\beta)] \\ &= \frac{z_0}{2\pi} \ln \left[ \csc (\beta) + \sqrt{\csc^2 (\beta) - 1} \right] \\ &= \frac{z_0}{2\pi} \ln [\csc (\beta) + \cot (\beta)] = \frac{z_0}{2\pi} \ln [\cot (\beta/2)] \quad (3) \end{aligned}$$

and this expression is consistent with earlier Equation (1). In Reference 7 the result for the  $z_c^{(\text{tilted})}$  given by Equation (2) is graphically plotted in Figure 4, and several observations can be made from this figure, and they are:

- (a) for an untilted cone (i.e.,  $\alpha = 90^\circ$ ), one requires a half angle  $\beta$  of the monocone to be  $< 10^\circ$ , in order to obtain a characteristic impedance of about  $150 \Omega$ ,
- (b) for a given half angle  $\beta$  of the monocone, the largest value of the characteristic impedance is obtained if the cone axis is normal to the ground plane,

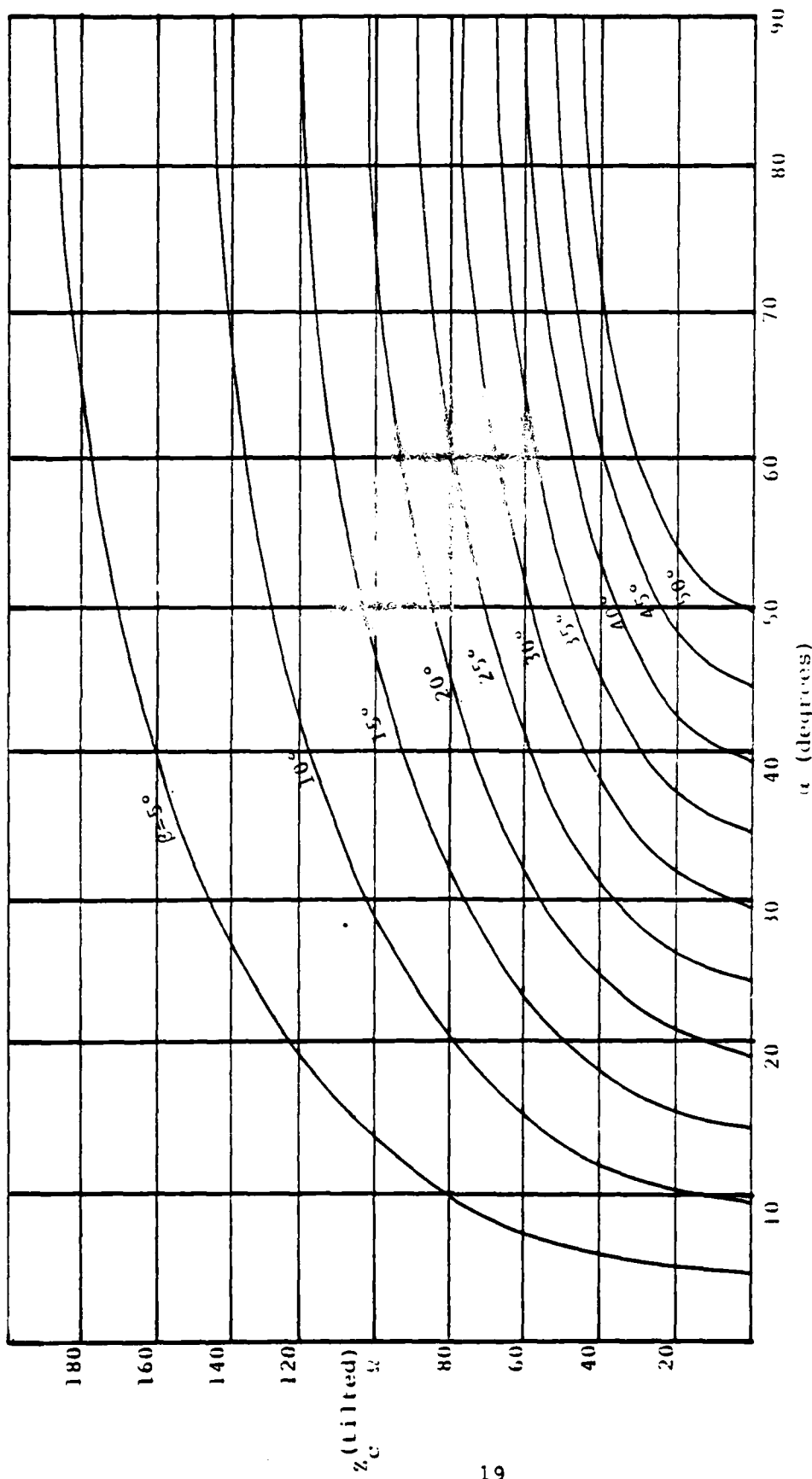


Figure 4. Characteristic impedance of a tilted monocone.

(c) same characteristic impedance value can be obtained for different sets of  $\alpha$  and  $\beta$  values; for example,  $100 \Omega$  impedance can be obtained for [ $\alpha = 14^\circ$ ,  $\beta = 5^\circ$ ] or [ $\alpha = 28^\circ$ ,  $\beta = 10^\circ$ ] or [ $\alpha = 46^\circ$ ,  $\beta = 15^\circ$ ], etc.

The last observation (c) can have an impact on the field matching considerations at the transition or interface between the switch and the Marx column. However, observation (b) is more informative and can be exploited in practice, by avoiding the tilt and getting the highest impedance value for practical  $\beta$  values. There are two conflicting requirements here, because it is meaningful to tilt the mono-cone so that it lines up better with the axis of the Marx column and thus reducing the field mismatch. But Figure 4 shows that tilting the cone (i.e.,  $\alpha < 90^\circ$ ) reduces the impedance, thus requiring smaller and smaller cone angles. One way of resolving this would be to include local ground plane variations. This will be discussed in further detail later in Section III.

Another criterion is minimizing the back-radiated energy. Once again, the formula for the fractional back-radiated power is available in Reference 7 and is given by

$$\frac{P_b}{P_t} = \frac{(1/2) \ln \left[ \frac{\cos(\beta) - \cos(\alpha) \cos(\theta_b)}{\cos(\alpha) - \cos(\beta) \cos(\theta_b')} \right]}{\operatorname{arccosh} [\sin(\alpha)/\sin(\beta)]} \quad (4)$$

where

$P_b$  ≡ power radiated in the cone between  $\theta = \theta_b$  and  $\theta = \pi$

$P_t$  ≡ total radiated power

Considering  $\theta_b = \pi/2$  and for reasonable values of  $\alpha$  and  $\beta$ , this Equation (4) estimates the back radiations of the order of 20%.

To summarize, the physical quantities of importance relating to the conical base of the simulator are(a) the characteristic impedance,(b) the fields at the switch/Marx column and switch/peaker interface, and(c) the back radiated energy. Although all these three parameters and ways of optimizing their values are all interrelated (e.g., varying  $\beta$  would affect all three of this quantities), it is fair to state that the most important parameter to optimize is the impedance.

### 3. Interfacing with Marx and Peakers

In Figure 2, a schematic diagram of the transition between the output switch and the Marx/Peaker columns was shown. This transition made of electrically inductive and mechanically thin interconnections is a source of impedance as well as field discontinuities. If the impedance of the switch is brought up to  $150 \Omega$ , then the problem would involve matching the transverse field distribution or at least, allowing for the fields to vary gradually. Such engineering modifications as replacing the thin interconnecting wire by appropriately shaped sheet metal or metalized fiberglass, should be a priority item for consideration.

### 4. Recommendations

The purpose of this paragraph is to propose modifications to the existing design configuration of the monocone output switch at the base of the Marx pulser in the ATLAS I or TRESTLE facility, with a view of improving the pulser performance. Four modifications are proposed and are individually discussed.

#### (a) Change of the Half Cone Angle $\beta$

When the change was made in 1974 from the bicone to the monocone switch configuration, due to budgetary and

other considerations, it was decided to continue using the same switch housing. This switch housing, however, consists of a steel dome, whereas the housing itself is made of fiberglass. Since the dome is metallic, it had to be of a certain minimum diameter to support the field levels. This minimum diameter leads one to the  $20^\circ$  value for the half cone angle, thus resulting in a smaller characteristic impedance value than desirable. Budgetary and other considerations aside, serious consideration should be given to fabricating a new switch housing with a fiberglass dome that can support the internal pressure as well, and with a cone half angle of about  $10^\circ$ , the desired impedance can be achieved. This, of course, would be the ideal solution.

(b) Ground Plane Variations

The switch cone, with its axis normal to the ground plane wedge makes a sharp angle with the remainder of the pulser leading to field mismatching at the interface. This calls for sloping the switch cone so as to make its field distribution better match that on the Marx column and peaker arms. As was earlier pointed out, mere tilting or sloping of the cone reduces the already low value of the characteristic impedance. One way around this problem would be to introduce or attach a second ground plane to the existing ground plane wedge. The cone axis can be maintained to be orthogonal to this tilted plane. This is schematically shown in Figure 5, which also includes a local shaping of the ground plane in the form of a hump. The shaping is such that, locally the electric field lines, normal to the tilted ground plane, are denser resulting in a higher impedance. This method could make use of the existing switch housing, but has an artificially increased value for the characteristic

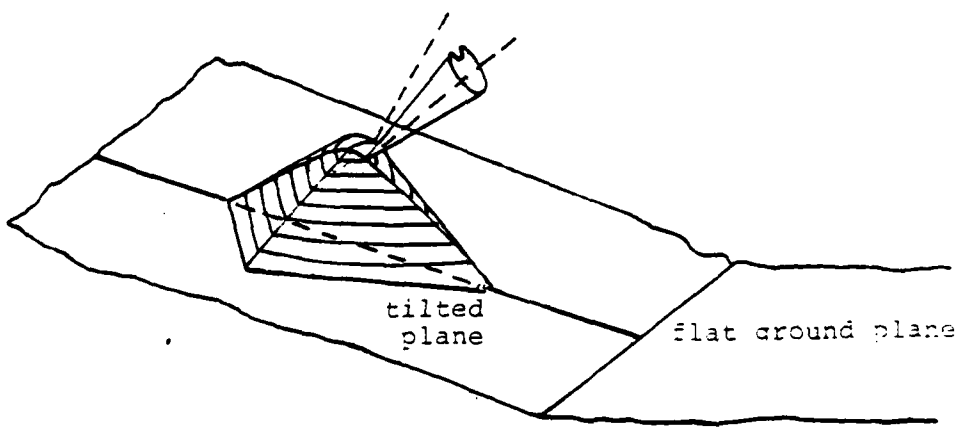


Figure 5. Local ground plane variations.

impedance. One could also attempt non circular cross sections for the cones, but a detailed theoretical solution for other shapes of the switch does not appear to be warranted at this time, since such attempts are best made in a controlled laboratory environment initially.

(c) Laboratory Experiments

If proposed modification (a) is discarded or found impractical for any reason, the next best alternative would be to consider local ground plane variations. Because of the irregular shapes of possible ground planes and, also with a view of avoiding extensive numerical computations, it is suggested that impedances of monocones over locally varying ground planes be measured in a laboratory. This would consist of appropriately driving the cone against the ground plane and making a TDR measurement of the impedance. Once the experimental set up and the measurement procedure is tested, a wide variety of local variations in the ground plane can be attempted.

It is to be emphasized that this method of ground plane variations has an inherent risk of improving the characteristic impedance at the very early times, but degrading it at later times because of the introduction of additional diffracting surfaces. Hence, the need for careful and extensive experimental trials.

(d) Switch Transition

The transition geometry along with the low switch impedance is the most serious area with respect to rise time degradation. Fortunately, this area is also the easiest part of the problem to model. It is proposed that a one-fifth scale model with sufficiently long transmission line to provide a 15 or 20 ns measurement cleartime be built. With such a model and carefully thought out experiments, the transition geometry can be optimized reasonably fast.

#### IV. PEAKER ARM OPTIMIZATION

The Marx type of pulser under consideration incorporates several (- four in the case of ATLAS I (TRESTLE) facility) peaking capacitor arms as part of its electromagnetic configuration, in delivering transient energy to the EMP simulator proper. The particular facility of interest, ATLAS I (TRESTLE), consists of a two-parallel-plate transmission line in the central region, with a wave launcher and a wave receptor on either side. The launcher and receptor conical transmission lines are formed by triangular shaped plates. While the wave receptor or the output conic section is terminated by a load impedance, the wave launcher or the input conic is driven by the electromagnetic energy source. Such a functional division of the facility is sketched in Figure 6 (Ref. 6).

The electromagnetic energy source employed in the ATLAS I (TRESTLE) facility is a pair of Marx type of pulse generators, rated nominally for a peak voltage of 5 MV each. A side view of a Marx pulser module configuration is shown in Figure 7. This configuration consists mainly of the central Marx column, the surrounding peaking capacitor arms and the monocone output switch at the base of the ground plane wedge. Each of these pulser elements has a key function in the wave transport and launching. In this section, attention is focused on the peaker arm optimization, making certain approximations; e.g., treating the Marx and the peaker arms as cylindrical conductors, with appropriate line constants. Specifically after a

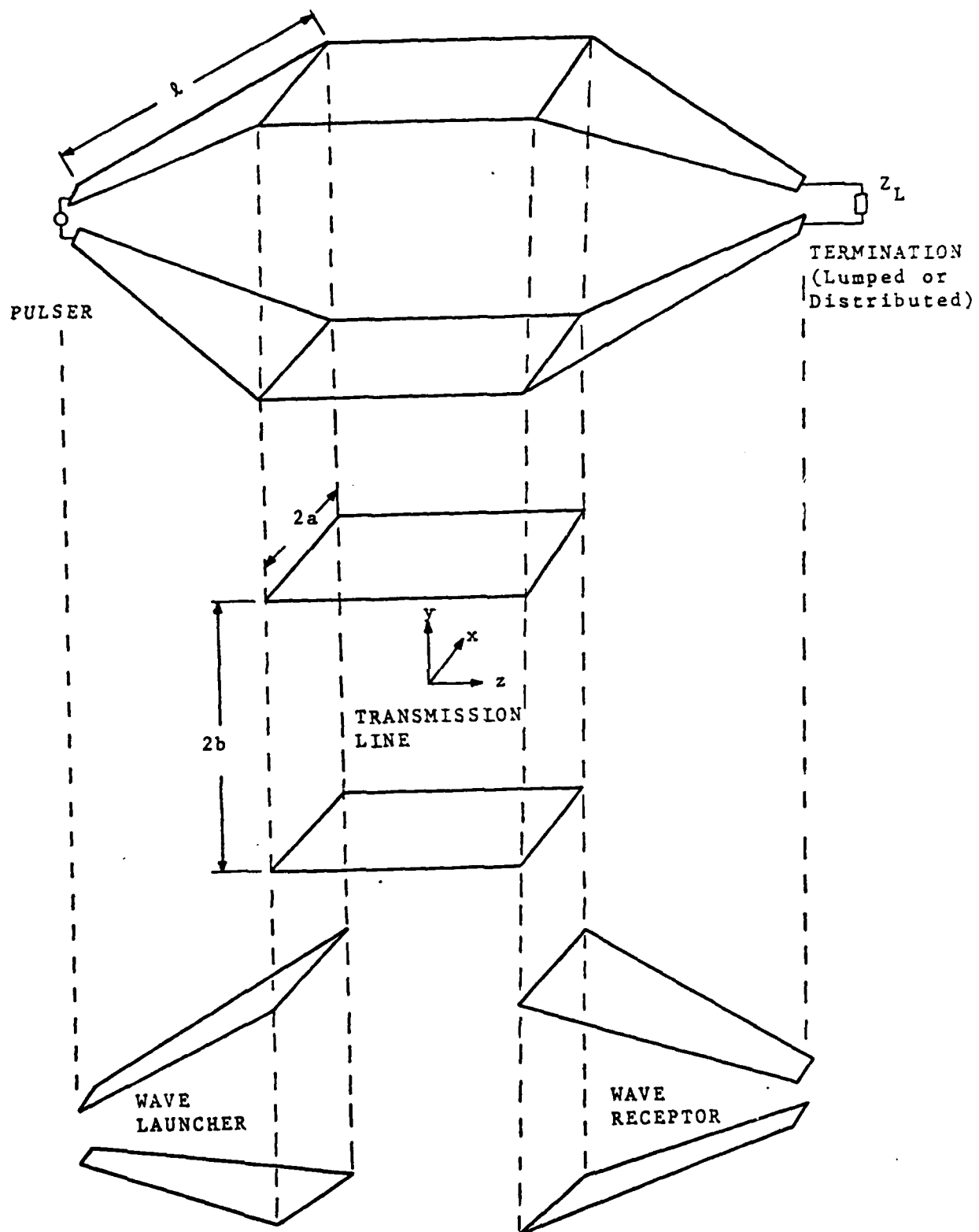


Figure 6. Schematic diagram of a parallel plate transmission line type of simulator, e.g., ATLAS.

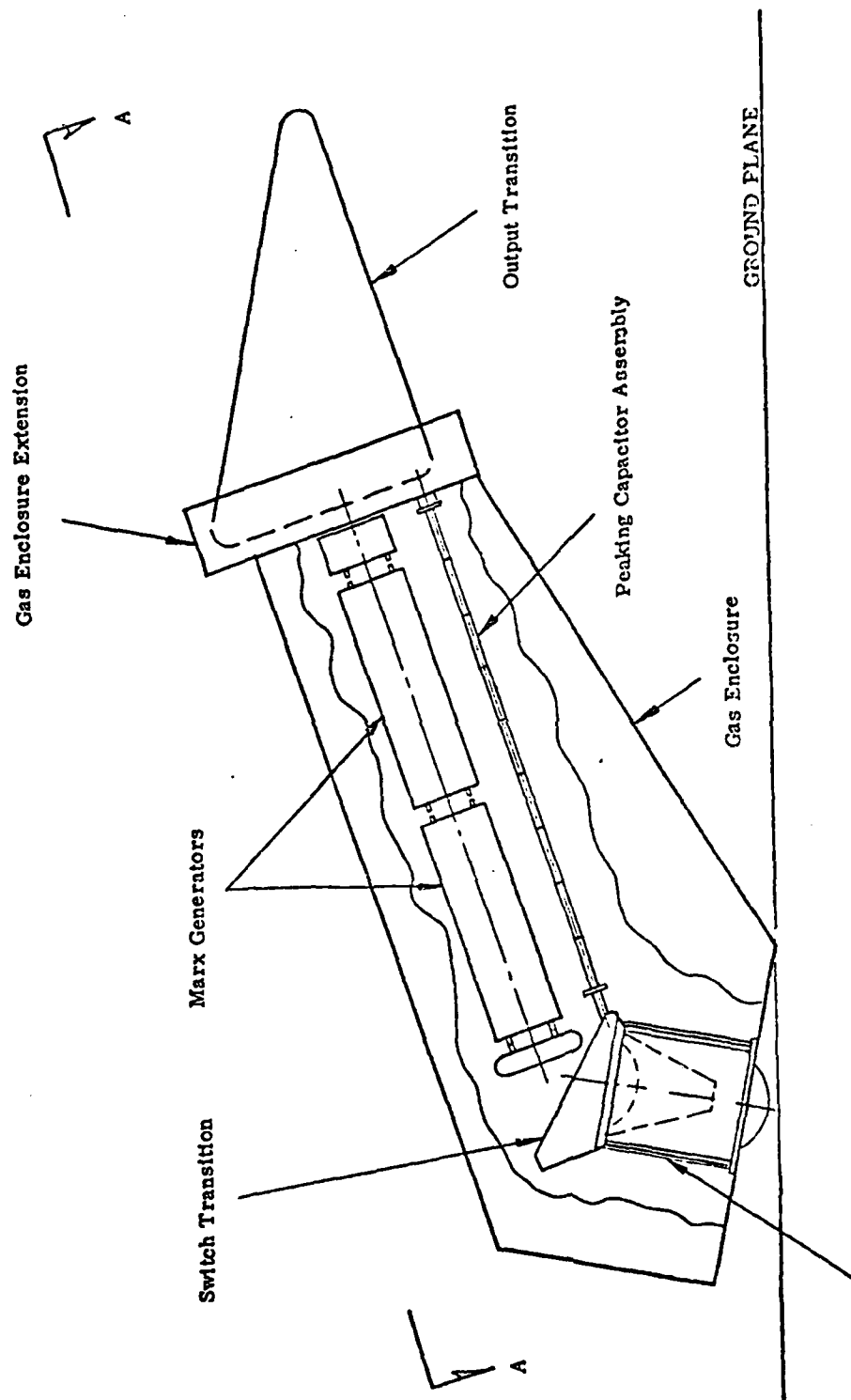


Figure 7. Marx pulser module configuration.

brief physical description of the peaker arms in Section IV we formulate a multiconductor transmission-line model for the case of  $N_p$  number of peakers along with the central Marx column, above a ground plane. This formulation is the subject of Section IV. Next, the optimum location of these peakers is sought. The constraints and approximations leading to a 2-wire model are described in Section IV. Conformal transformation of the physical plane into a complex potential plane, as described in Section IV leads to the optimum location of the given  $N_p$  peakers. In the concluding Section IV, representative numerical results are presented.

#### 1. Peaking Capacitor Arm Description

The peaking capacitor arms used in Marx pulser modules serve a two-fold function of masking the inductance of the Marx generator and providing a peaking element to aid in achieving a fast rise time pulse into a transmission line type of EMP simulator. For example, the electrical parameters of the peaking capacitor arms in the pulser module of the ATLAS I facility are listed below.

---

TABLE 2<sup>\*</sup>  
ELECTRICAL PARAMETERS OF PEAKER ARMS

---

1) Number of Peaking Capacitor Arm Assemblies	4
2) Total Peaking Capacitance (including strays)	345 pF
3) Ratio of Marx to Peaking Capacitance	9 to 1
4) Peaking Capacitor Open Circuit Ring Period	339 ns

---

\*This Table and the material relating to the physical description of the peakers are to be found in detail in Maxwell Laboratory Reports #170 of April 1972 and #294 of April 1975.

The individual capacitors used to make up the peaking capacitor assemblies are similar to those used in the TORUS system.

The individual capacitors were designed to operate at 550 kV. Therefore, a series string of nine were required to bridge the 5 MV Marx generator. Four peaking capacitor assemblies are in parallel across the Marx generator. Thus, the number of units in series,  $N_s$ , is 9; and the number in parallel,  $N_p$ , is 4.

The peaking capacitor assembly is the same length as the Marx and the voltage grading approximately the same at full voltage. Very similar voltage gradients were used in the TORUS generator, where no flashover problems were encountered. The peaking capacitor assemblies in ATLAS I (TRESTLE) facility are approximately 0.3 m from the Marx generator at the closest point, and the entire system is operated in an SF<sub>6</sub> environment. The SF<sub>6</sub> environment permits relatively close positioning of Marx and peakers. However, it should be pointed out that flashover between Marx and peakers have occasionally occurred.

The peaking capacitor arm assembly is shown in Figure 8. Each arm consists of a fiberglass angle support, nine 550 kV peaking capacitors, with PVC supports and a corona ring at the end. A single unit peaking capacitor is described below.

The unit capacitor has a plastic case (5 cm x 10 cm x 47 cm) or (2 inch x 4 inch x 18.5 inch) with electrical terminations at opposite ends and in the center of the 5 cm x 10 cm end plates, as shown in Figures 9 and 10. The terminations are designed to be mounted in a dielectric angle support to form a peaking capacitor assembly of series units.



Figure 8. Peaking capacitor arm assembly.

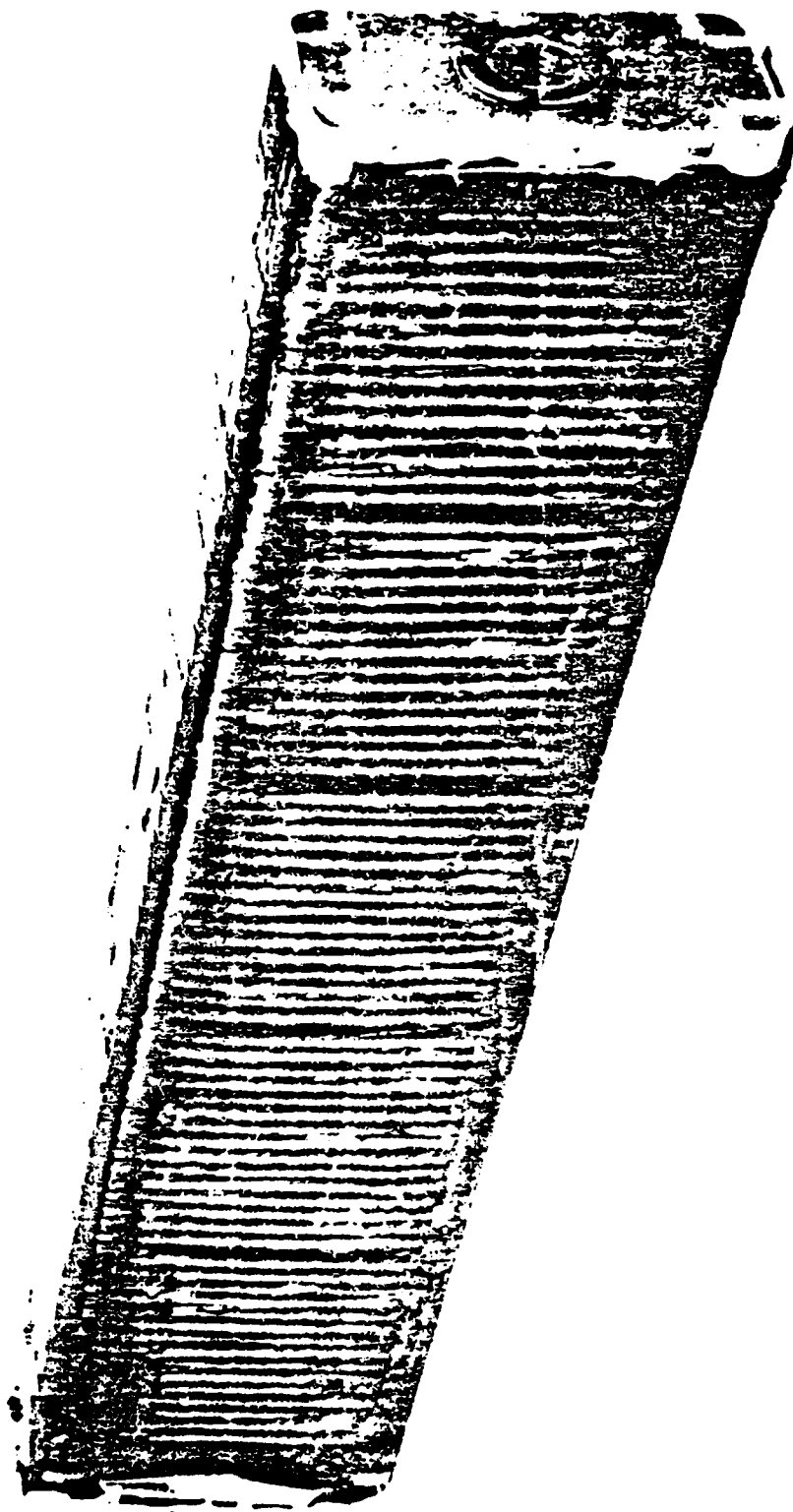


Figure 9. The unit peaking capacitor used in ATLAS I (TRESTLE) facility.

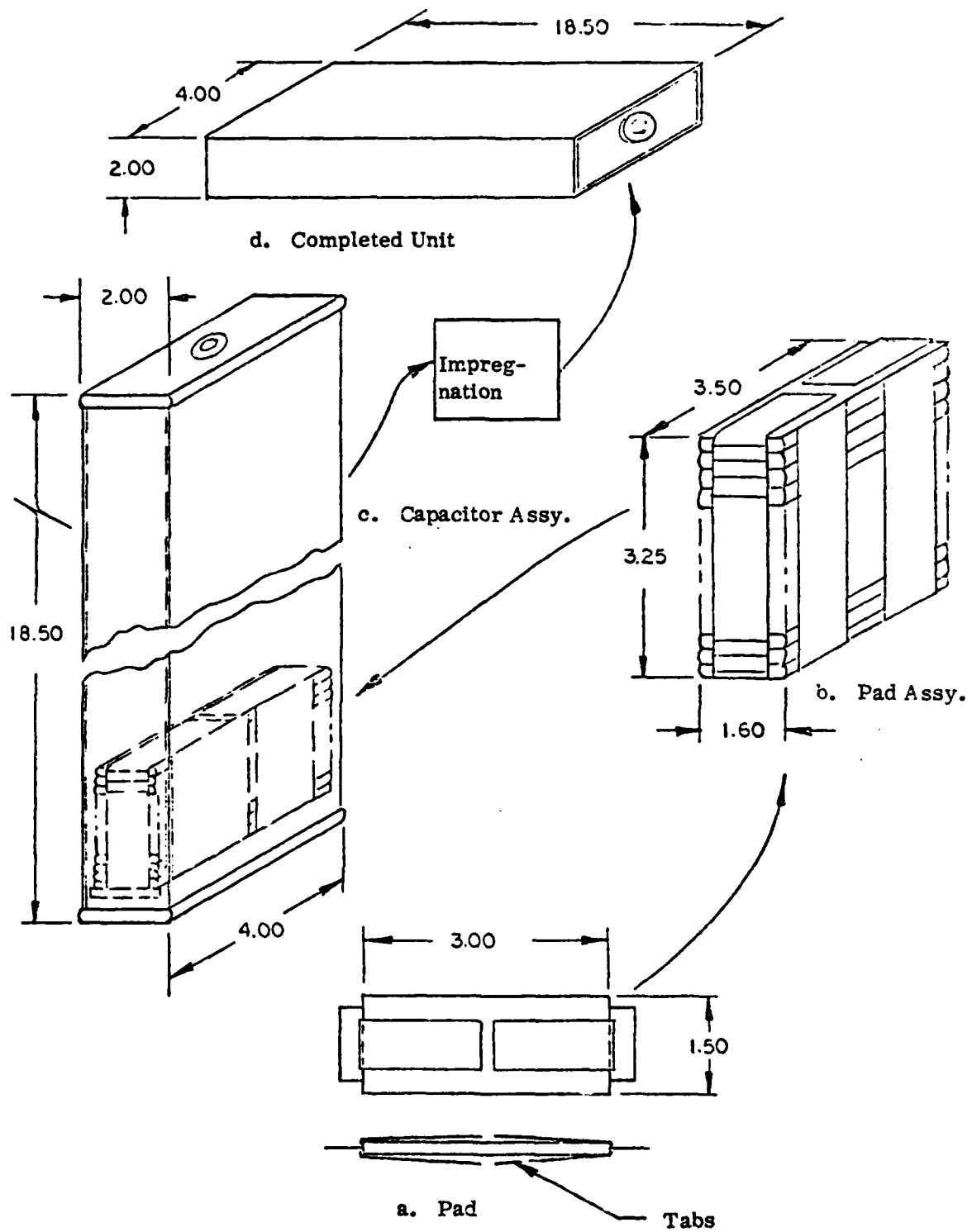


Figure 10. Peaking capacitor assembly (all indicated dimensions are in inches).

Seventy flattened capacitor pads are electrically connected in series to provide 606 pF at 550 kVDC as a unit capacitor. The pad voltage of 7143 V is impressed on a composition multilayer dielectric of three layers of 0.00025 in Kraft capacitor tissue and two layers of 0.00075 in Mylar, resulting in a dynamic dielectric stress of 2005 V/m on the tissue 3760 V/m on the Mylar. Some of the characteristics of the unit peaking capacitor are listed below.

TABLE 3  
CHARACTERISTICS OF UNIT<sup>\*</sup> PEAKER CAPACITOR

1) Capacitance	(606 ± 10%) nF
2) Voltage	550 kVDC, pulse charge
3) Inductance	300 nH
4) Voltage reversal	20% max
5) Temperature range	
(a) operating	+ 14° F to 113° F
(b) storage	- 40° F to 113° F
6) Weight	~ 7.75 lbs

\* Recall that there are 4 peaker arms in parallel, each of which has 9 unit peaker capacitors in series.

Note: 1) The above rating applies to a unit peaking capacitor operated in a pulse charge mode, while immersed in an SF<sub>6</sub> dielectric gas environment of 14-15 psia.

2) Performance rating with respect to frequency are unavailable.

The capacitor elements are convolutely wound pads, laid in tab-type construction, with both tabs projecting from the ends of the windings, then bent back on opposite sides of the flattened pad to provide double contact to the tabs of adjacent pads. This design provides double contact area in the interpad connection, equalizes the pressure over the pad flattened area, and removes cut tab ends from the active area of the dielectric, thus preventing possible failure from sharp edges of the cut tab.

The stacked pads are held in compression in a frame made of four tension rods of polycarbonate plastic threaded into an epoxy-fiberglass pressure plate floating below a top plate held in position by four plastic nuts threaded on the tension rods. Pressure adjustments after assembly and vacuum drying are accomplished by means of a plastic screw threaded through the top frame plate and bearing on the center point of the pressure plate.

The case of the peaking capacitor is in the shape of an open end tube of 0.032 in fiberglass-epoxy. The assembly of 70 pads stacked in the frames is positioned inside the case by the shape of the end plates and spacers, the dimensions of the plates and spacers conforming to the shape of the case. The end plates are secured to the case by 10 plastic screws in each end and sealed by filled epoxy cement coating the interstices between the plates and the case inner wall.

In the manufacturing process for the peaking capacitor, the operation of removing moisture and impregnation with oil is succeeded by a third step--encapsulation. The vacuum drying under heat and impregnation with oil is carried out in much the same manner as conventional capacitors. After impregnation and soaking, however, residual oil is drained from the case, under controlled

conditions, a hard vacuum is pulled to remove entrapped gas, and an encapsulant is introduced under vacuum to completely fill the space inside the case. After polymerization of the encapsulant, the result is that the capacitive elements are impregnated with a dielectric oil, they are encased in a resilient coating of encapsulant of high dielectric strength and excellent moisture resistance, the whole being protected by the plastic case, which provides a rigid support for the electrodes and precise dimensions for assembly into the peaking tubes.

From the above physical description of the peaker arm assemblies, one has to make simplifying approximations, to pursue design studies. One such approximation is to idealize the peaker arms and the Marx column by perfectly conducting circular cylinders with finite radii. One of the consequences of this assumption is in computing the characteristic impedance of the peaker array. However, even approximating the peakers and Marx column by line currents has led to useful results with less than 10% error estimates (Ref. 7). In view of this, the present approximation has even less of an impact on the accuracy of calculations.

## 2. Multiconductor Transmission-Line Model of Peakers and Marx

An important problem (Ref. 2) for which design curves are already available (Ref. 7) is the 4 peaker arm configuration sketched in Figure 11. The problem is to determine the relationship between  $x_1$ ,  $y_1$ ,  $x_2$ , and  $y_2$  by including the images of all conductors. The criteria in obtaining this relationship are:

(a) During the peaker charge cycle, i.e., before the output switch fires, the return current flows in the Marx. With reference to Figure 11,  $2(I_1 + I_2) = I_M$  and one is required to null the magnetic flux between

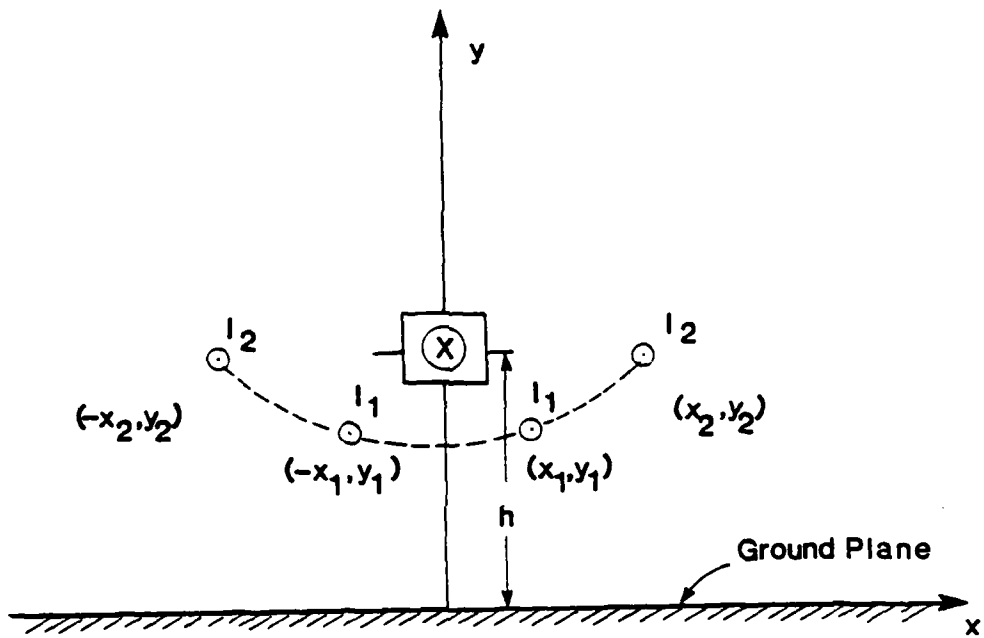


Figure 11. Four peaker arms and the central Marx column above a perfectly conducting ground plane.

the two peakers in the first quadrant, to avoid different voltages on the peaker arms.

(b) During the discharge cycle, i.e., after the output switch fires, the return current flows in the ground plane (or, equivalently, in the image conductors). With reference to Figure 11, for no net flux between peakers the Marx current  $I_M$  should be = 0. In reality, it nearly vanishes limited by the Marx inductance.

While satisfying the above two criteria, the relationship between  $x_1$ ,  $y_1$ ,  $x_2$ , and  $y_2$  falls out and the computations have been reported in Reference 7. One of their figures is reproduced here for the sake of completeness, in Figure 12. It is noted that symmetry about the  $y$  axis is maintained in the solution. The Figure 12 gives the possible locations for the second arm  $(x_2/h, y_2/h)$ , for a given location of the first arm  $(x_1/h, y_1/h)$  so that the null-flux conditions are met.

However, it is not obvious if indeed four is the optimum number of peakers. In an attempt to improve upon the available data, let us extend the above cited work to a general case of  $N_p$  peaker arms. It now suffices to seek the optimum location of the given  $N_p$  peakers. With reference to Figures 13 and 14, a distinction is made between the two cases of  $N_p$  even and  $N_p$  odd. The peakers have a radius of  $r_p$  and the central Marx column centered at  $(0,1)$  in the transverse  $x-y$  plane, has a radius of  $r_M$ . In Figure 13, the Marx conductor returns a current  $I_M$  and each of the  $N_p$  peakers is carrying a current equal to  $I_p/N$ . The ordering of peakers is done in a counterclockwise sense, so that as  $N_p \rightarrow \infty$ , the peaker numbering is continuous.

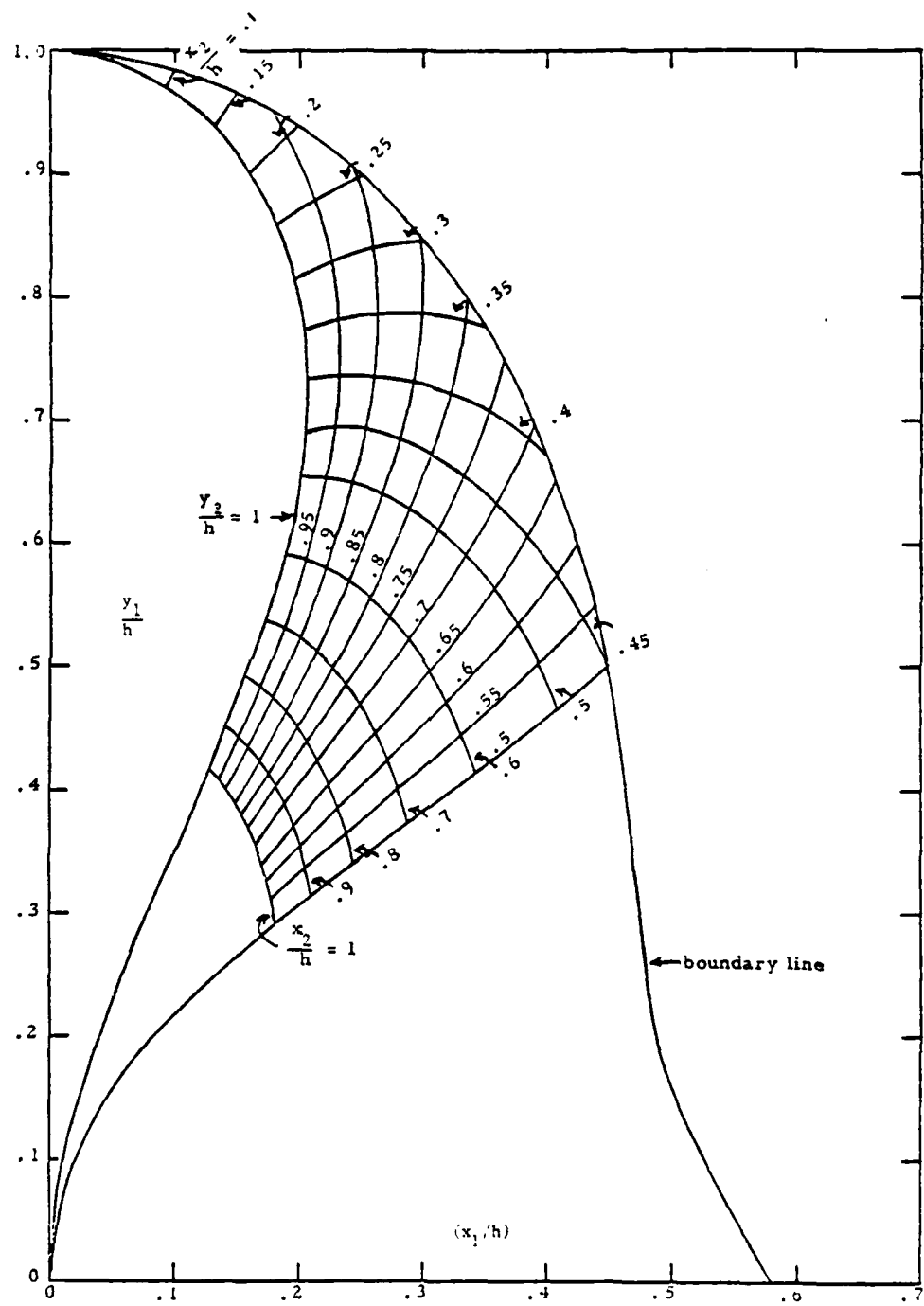


Figure 12. Arm 2 positions satisfying the two null-flux conditions.

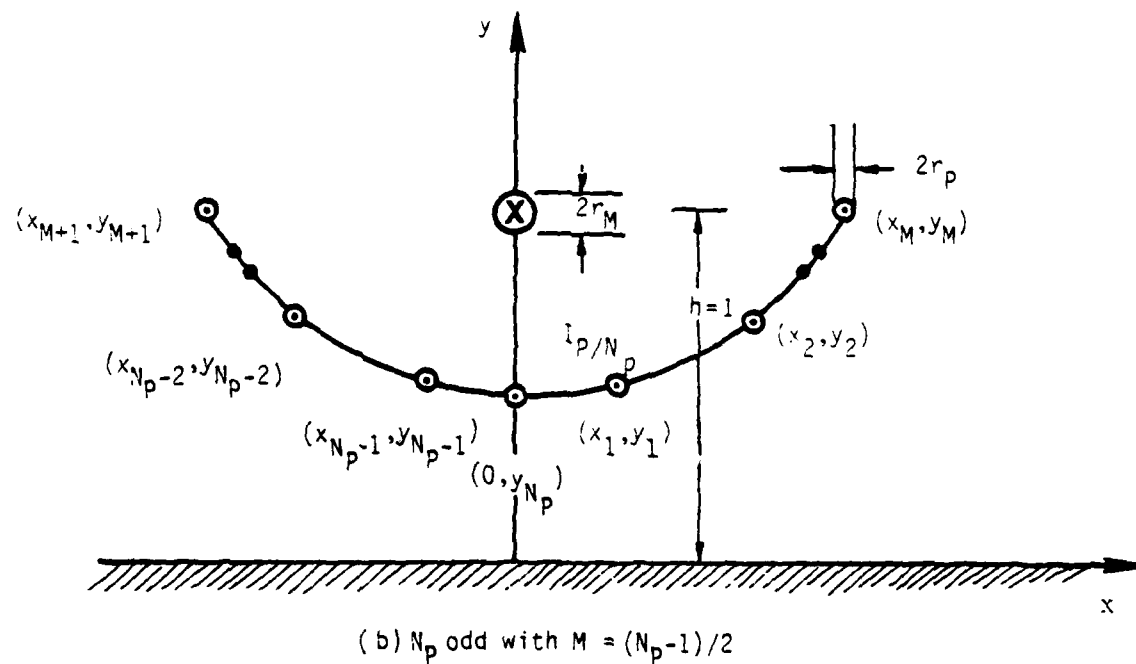
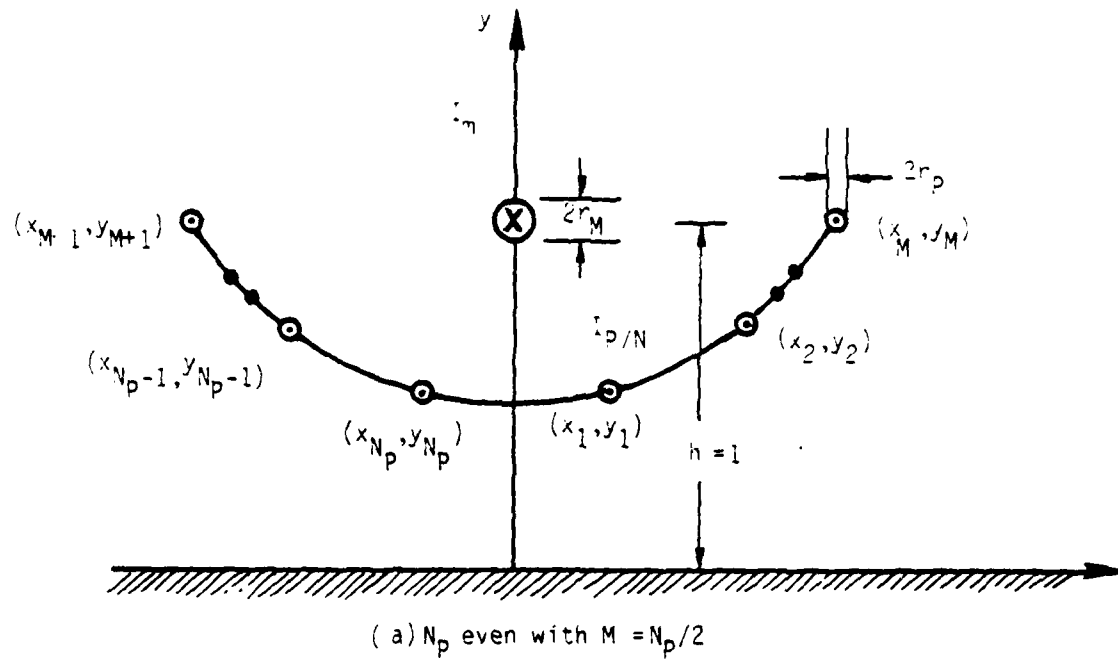


Figure 15. Modeling of the Marx column and the peakers above a ground plane, before the output switch fires.

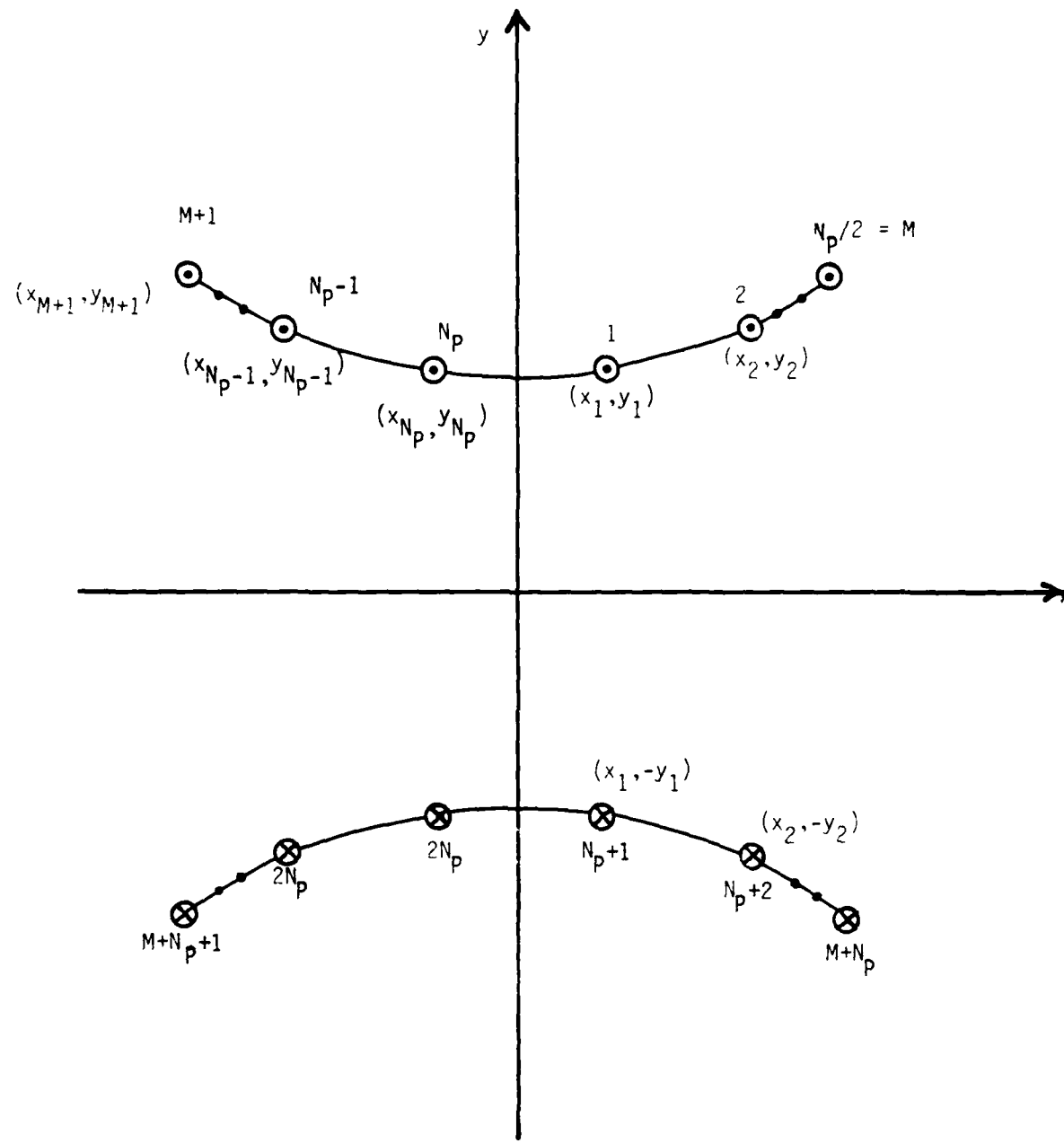


Figure 14. Return current flow in the image conductors after the output switch fires, for the case of  $N_p$  even with  $M = N_p/2$  corresponding to Figure 13a.

We note, because of symmetry

(a) for  $N_p$  even (Figure 13a)

$$x_n = -x_{N_p - n+1}; \quad y_n = y_{N_p - n+1}$$

for  $n = 1, 2, \dots, N_p$       (5)

(b) for  $N_p$  odd (Figure 13b)

$$x_n = -x_{N_p - n}; \quad y_n = y_{N_p - n}$$

for  $n = 1, 2, \dots, N_p$       (6)

In addition, the peaker arm numbered  $N_p$  is centered at  $(0, y_{N_p})$  on the y axis.

It is assumed that the given or known parameters are  $r_p$ ,  $r_M$ ,  $N_p$ , and the load impedance representing the simulator  $Z_T$  (e.g., 150  $\Omega$ ). The given system is formed by  $N_p$  conductors ( $N_p$  peakers and the Marx) and a reference conductor. Let the voltages and the currents on the  $N_p + 1$  conductors be denoted by  $V_n$  and  $I_n$ . They are related by

$$\begin{pmatrix} V_1 \\ V_2 \\ \vdots \\ V_{N_p} \\ \hline (V_{N_p+1}) \end{pmatrix} = \begin{pmatrix} z_{c_{1,1}} & \dots & z_{c_{1,N_p}} & | & z_{c_{1,N_p+1}} \\ z_{c_{2,1}} & \dots & z_{c_{2,N_p}} & | & z_{c_{2,N_p+1}} \\ \vdash & & \vdash & & \vdash \\ z_{c_{N_p,1}} & \dots & z_{c_{N_p,N_p}} & | & z_{c_{N_p,N_p+1}} \\ \hline z_{c_{N_p+1,1}} & \dots & z_{c_{N_p+1,N_p}} & | & z_{c_{N_p+1,N_p+1}} \end{pmatrix} \begin{pmatrix} I_1 \\ I_2 \\ \vdots \\ I_{N_p} \\ \hline (I_{N_p+1}) \end{pmatrix}$$

In a shorthand matrix notation, (7) can be written as

$$(V_n) = (Z_{C_{n,m}}) (I_m) \quad (8)$$

It is convenient to define a dimensionless geometric factor matrix  $(f_{g_{n,m}})$  as follows

$$(Z_{C_{n,m}}) = Z_0 (f_{g_{n,m}}) \quad (9)$$

In this notation, the inductance per unit length  $(L'_{n,m})$  and the elastance per unit length  $(C'_{n,m})^{-1}$  matrices for the  $(N_p+2)$  conductor systems are given by

$$(L'_{n,m}) = \mu_0 (f_{g_{n,m}}) \quad (10)$$

$$(C'_{n,m})^{-1} = (\frac{1}{\varepsilon_0}) (f_{g_{n,m}}) \quad (11)$$

From purely geometrical considerations, after making a thin wire or rotational symmetry approximation, one can write down the elements of the geometric factor matrix as [11],

$$f_{g_{n,n}} = \frac{1}{2\pi} \ln \left( \frac{2y_n}{r_p} \right); \text{ for } n = 1, 2, \dots, N_p \quad (12)$$

$$f_{g_{n,m}} = \frac{1}{2\pi} \ln \left( \frac{d_{n,m}^*}{d_{n,m}} \right); \text{ for } n, m = 1, 2, \dots, N_p; \\ \text{for } n \neq m \quad (13)$$

where

$y_n$  = height of the  $n^{th}$  peaker arm above ground plane

$d_{n,m}$  = distance between the centers of the  $n^{th}$  and the  $m^{th}$  peaker arm

$d_{n,m}^*$  = distance between the centers of the  $n^{th}$  image peaker arm and the  $m^{th}$  peaker arm

The remaining matrix elements are given by

$$f_{g_{n,N_p+1}} = \frac{1}{2\pi} \ln \left( \frac{d_{n,N_p+1}^*}{d_{n,N_p+1}} \right) = f_{g_{N_p+1,n}}$$

for  $n = 1, 2 \dots N_p$  (14)

by reciprocating, and lastly

$$f_{g_{N_p+1,N_p+1}} = \frac{1}{2\pi} \ln \left( \frac{2h}{r_M} \right) \quad (15)$$

Also, note that because of symmetry relationship of Equation (5) for the  $N_p$  even case, we have

$$f_{g_{n,n}} = f_{g_{N_p-n+1,N_p-n+1}} ; \text{ for } n = 1, 2 \dots N_p \quad (16)$$

$$f_{g_{n,m}} = f_{g_{m,n}} ; \text{ for } n, m = 1, 2 \dots N_p \quad (17)$$

Recalling the criteria for determining the optimum peaker arm locations, we have

(a) during the charge cycle

Marx current  $I_M$  = sum of all peaker arm currents

$$= N_p \times (I_p/N_p) = I_p \quad (18)$$

This condition of Equation (17) amounts to equal peaker response from Marx or vice versa by reciprocity. If current  $I_M$  is injected into the Marx conductor, it should lead to equal peaker currents and, consequently, Equation (7) becomes

$$\begin{pmatrix} v_p \\ v_p \\ \vdots \\ v_p \\ \hline v_m \end{pmatrix} = \begin{pmatrix} z_{c_{1,1}} & \dots & z_{c_{1,N_p}} & z_c^{(P,M)} \\ & & & z_c^{(P,M)} \\ z_{c_{N_p,1}} & z_{c_{N_p,N_p}} & z_c & \\ \hline z_c^{(P,M)} & z_c^{(P,M)} & z_{c_M} & \\ & & & I_M \end{pmatrix} \begin{pmatrix} I_p/N_p \\ I_p/N_p \\ I_p/N_p \\ / \end{pmatrix} \quad (19)$$

In the above Equation (19),

$$z_{c_{n,N_p+1}} = z_{c_{N_p+1,n}} = \text{constant } z_c^{(P,M)} \quad (20)$$

which implies

$$f_{g_{n,N_p+1}} = f_{g_{N_p+1,n}} = f_g^{(P,M)} \text{ (say)} \quad (21)$$

(b) After the output switch fires:

After the main switch fires, Marx current begins to fall off governed by its RLC time constant and the return current flows through the image peakers or, equivalently, the ground plane. It is desirable to have a uniform wave propagating on the peaker arms, i.e., equal voltages on all of the  $N_p$  peaker arms resulting in equal current flowing through the peaker conductors. If such a uniformity is achieved, the charge per unit length  $Q'_n$  on all of the peakers will also be uniform, resulting in uniform surface electric fields. By setting the Marx current  $I_M$  equal to zero and uniform peaker voltages and currents, we require

$$\begin{pmatrix} v_p \\ v_p \\ \vdots \\ \vdots \\ v_p \\ \hline v_m \end{pmatrix} = 
 \begin{pmatrix} z_c \\ \dots \\ \dots \\ z_c^{(P,M)} \\ \hline z_c^{(P,M)} & z_c^{(P,M)} \\ z_c^{(P,M)} & z_{cM} \end{pmatrix} 
 \begin{pmatrix} I_p/N_p \\ I_p/N_p \\ \hline 0 \end{pmatrix} \quad (21)$$

This implies

$$(f_g_{n,m}) = \frac{f_g^{(P)}}{N_p} (1_{n,m}) \quad (22)$$

Combining the results of the above two conditions, the geometric factor matrix is now given by

$$f_g_{n,m} \underset{(N+1) \times (N+1)}{=} 
 \begin{pmatrix} \frac{f_g^{(P)}}{N_p} & \begin{pmatrix} 1 & 1 & \dots & \dots & \dots & 1 \end{pmatrix} \\ \hline f_g^{(P,M)} & (1, 1, \dots, 1) \end{pmatrix} \quad (23)$$

This formally completes a description of the formulation of the general case of  $N_p$  peakers along with a Marx conductor above a ground plane, while invoking the theory of multiconductor transmission line. In the following section, we seek a way of reducing this system to a simpler two-conductor model which is more easily amenable to calculations.

### 3. Constraints in Multiconductor Model Leading to Two-Conductor Model

It would be desirable to represent the  $N_p$  number of peakers by a single effective conductor. This effective peaker along with the central Marx conductor forms a coupled transmission line, as illustrated in Figure 15. The advantage of such a model will be demonstrated as follows and later, a simpleminded procedure to obtain the equivalent single peaker arm will be proposed. With reference to Figure 15, the transmission line equations are

$$\frac{d}{dz} (\hat{V}_n) = -s(L'_{n,m}) \cdot (\hat{I}_n) \quad (24)$$

$$\frac{d}{dz} (\hat{I}_n) = -s(C'_{n,m}) \cdot (\hat{V}_n)$$

leading to

$$\frac{d^2}{dz^2} (\hat{V}_n) - (\gamma_{n,m})^2 (\hat{V}_n) = 0 \quad (25)$$

with  $(\gamma_{n,m}) = s\sqrt{(L'_{n,m}) \cdot (C'_{n,m})}$  and the primes indicate per-unit-length parameters.

Since additional inductance of Marx ( $L'_m$ ) is, in effect, like having a dielectric coating around the Marx, one expects the two modes of propagation in the model problem of Figure 15 to travel with different velocities of

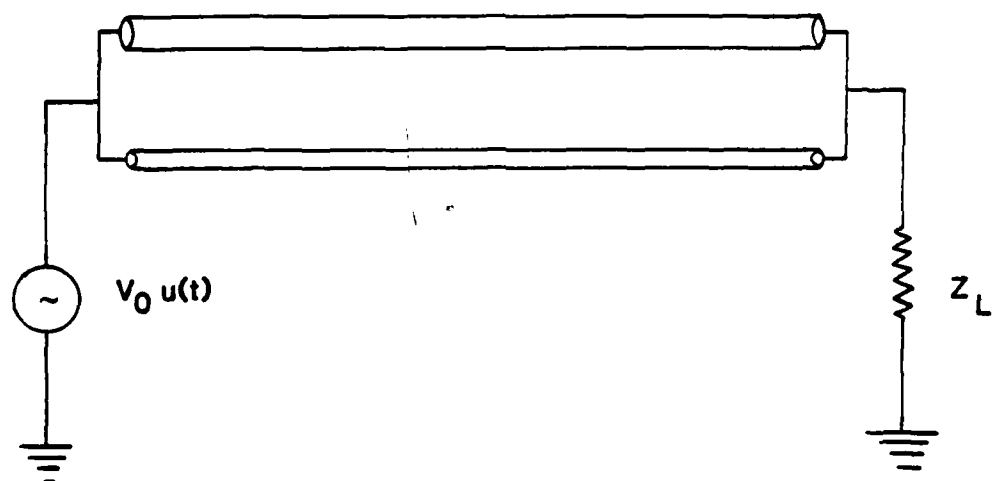
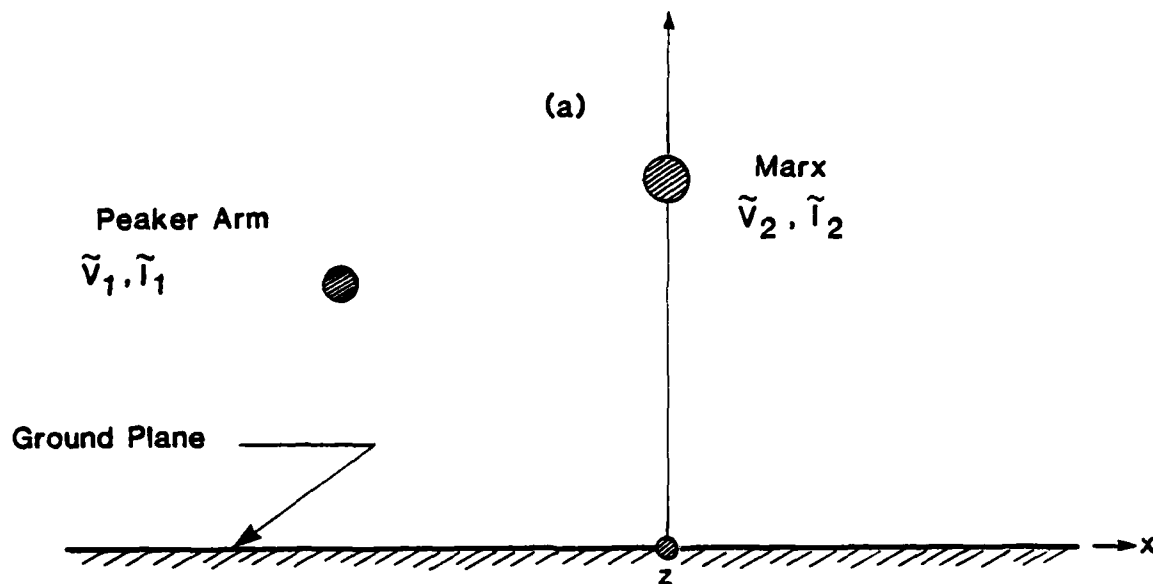


Figure 15. Coupled transmission line model for the Marx and a single peaker arm.

propagation,  $v_1$  and  $v_2$ . A knowledge of these velocities and corresponding transit times is significant in the process of optimizing the number and distribution of peaker arms.

We have

$$(L'_{n,m}) = \begin{pmatrix} L'_{11} & L'_{12} \\ L'_{21} & L'_{22} + L'_m \end{pmatrix} \quad (C'_{n,m}) = \begin{pmatrix} C'_{11} & C'_{12} \\ C'_{21} & C'_{22} \end{pmatrix} \quad (26)$$

One can show

$$(L'_{n,m}) \cdot (C'_{n,m}) = \begin{cases} (\delta_{n,m}) \frac{1}{c^2} & \text{if } L'_m = 0 \\ (\delta_{n,m} + \epsilon_{n,m}) \frac{1}{c^2} & \text{if } L'_m \neq 0 \end{cases} \quad (27)$$

where  $(\delta_{n,m})$  is the unit diagonal matrix and the error matrix  $(\epsilon_{n,m})$  is given by

$$(\epsilon_{n,m}) = \begin{pmatrix} 0 & 0 \\ 0 & L'_m \end{pmatrix} \begin{pmatrix} L'_{11} & L'_{12} \\ L'_{21} & L'_{22} \end{pmatrix}^{-1} = \begin{pmatrix} 0 & 0 \\ \frac{-L'_m L'_{12}}{\Delta} & \frac{L'_m L'_{11}}{\Delta} \end{pmatrix} \quad (28)$$

where

$$\Delta \equiv \text{determinant} = (L'_{11} L'_{22} - L'_{12} L'_{21}) \quad (29)$$

Now, the two velocities of propagation are given by  $v_i = (c/\sqrt{\lambda_i})$  for  $i = 1, 2$  where the two  $\lambda$ 's are the eigenvalues of  $(\delta_{n,m} + \epsilon_{n,m})$ , given by

$$\det (\delta_{n,m} + \varepsilon_{n,m} - \lambda_3 \delta_{n,m}) = 0$$

$$\det (\delta_{n,m}(1-\lambda_3) + \varepsilon_{n,m}) = 0$$

$$\det \begin{pmatrix} 1-\lambda_3 & 0 \\ \varepsilon_{21} & 1 + \varepsilon_{22} - \lambda_3 \end{pmatrix} = 0 \quad (30)$$

which leads to

$$\lambda_1 = 1 \text{ and } \lambda_2 = (1+\varepsilon_{22}) = \left[ 1 + \left( \frac{L'_m L'_{11}}{\Delta} \right) \right] \quad (31)$$

Thus, the two velocities are

$$v_1 = c \text{ and } v_2 = c / \left[ 1 + \frac{L'_m L'_{11}}{(L'_{11} L'_{22} - L'_{12} L'_{21})} \right] \quad (32)$$

If  $\ell$  is the total length of the Marx or peaker arms, the difference in the transit time for the two waves is therefore

$$\Delta t = (\ell/v_2) - (\ell/v_1) = \frac{\ell(v_1 - v_2)}{v_1 v_2} \quad (33)$$

At this stage, one can estimate the above quantities ( $\lambda_1$ ,  $\lambda_2$ ,  $v_1$ ,  $v_2$ , and  $\Delta t$ ) by substituting for the per-unit-length parameters. Furthermore, the two conductor model as shown in Figure 15b can also be analyzed in a straight forward manner for the voltage across the load  $V_L(t)$ , which is the pulser output waveform for an assumed step function at the input. The actual computational results are presented in later sections. From earlier considerations of equal peaker potential, we are constrained to place the peakers on an equipotential surface caused by a voltage on the Marx column with respect to the ground plane.

Returning to the question of how to choose an effective peaker conductor, a simple minded way is to choose a conductor whose  $f_g$  is the average of  $f_{g_{n,n}}$  for  $n = 1, \dots, N_p$ , and place this conductor on the same equipotential as the  $N_p$  peakers, centered on the  $y$  axis. The averaging process, then determines the radius of the effective peaker arm. For example

(a) say there are  $N_p$  peakers

$$\frac{1}{N_p} \sum_{n=1}^{N_p} f_{g_{n,n}} = f_{g_{\text{eff}}} \quad (34)$$

leading to

$$\frac{1}{N_p} \sum_{n=1}^{N_p} \ln \left( \frac{2y_n}{r_p} \right) = \ln \left( \frac{2y_e}{a_e} \right) \quad (35)$$

$$\prod_{n=1}^{N_p} \left( \frac{y_n}{r_p} \right) = \left( \frac{y_e}{a_e} \right)^{N_p} \quad (36)$$

$$a_e = \frac{r_p y_e}{\left( \prod_{n=1}^{N_p} y_n \right)^{1/N_p}} \quad (37)$$

Since  $y_e$  is determined by the particular equipotential surface being used, Equation (37) is useful in determining the effective radius of the equivalent peaker arm. This completes the description of the two-conductor model formulation.

#### 4. Optimal Positioning Based on Conformal Transformation

We shall first establish the impedance and the complex potential distribution of the Marx conductor above the ground plane. The results for this classical problem are available (Refs. 9 and 10) in the literature. For a line conductor centered at  $(0,1)$  in the physical  $z$  ( $=x+jy$ ) plane, as shown in Figure 16a, the complex potential is given by

$$w = u + jv = 2j \operatorname{arccot}(z) = \ln \left( \frac{z+j}{z-j} \right) \quad (38)$$

This corresponds to equal and opposite line charges at  $(x,y) = (0, \pm 1)$ . The equipotentials and magnetic field lines are given by constant  $u$  and the electric field lines by constant  $v$ . These contours of constant  $u$  and  $v$  are easily computed from the transformation as shown plotted in Figure 16a. The transformed or the complex potential  $w$ -plane is sketched in Figure 16b. Also note that the pulse impedance  $Z_L$ , of the transmission line is related to the wave impedance,  $Z$  by

$$Z_L = f_g Z \quad (39)$$

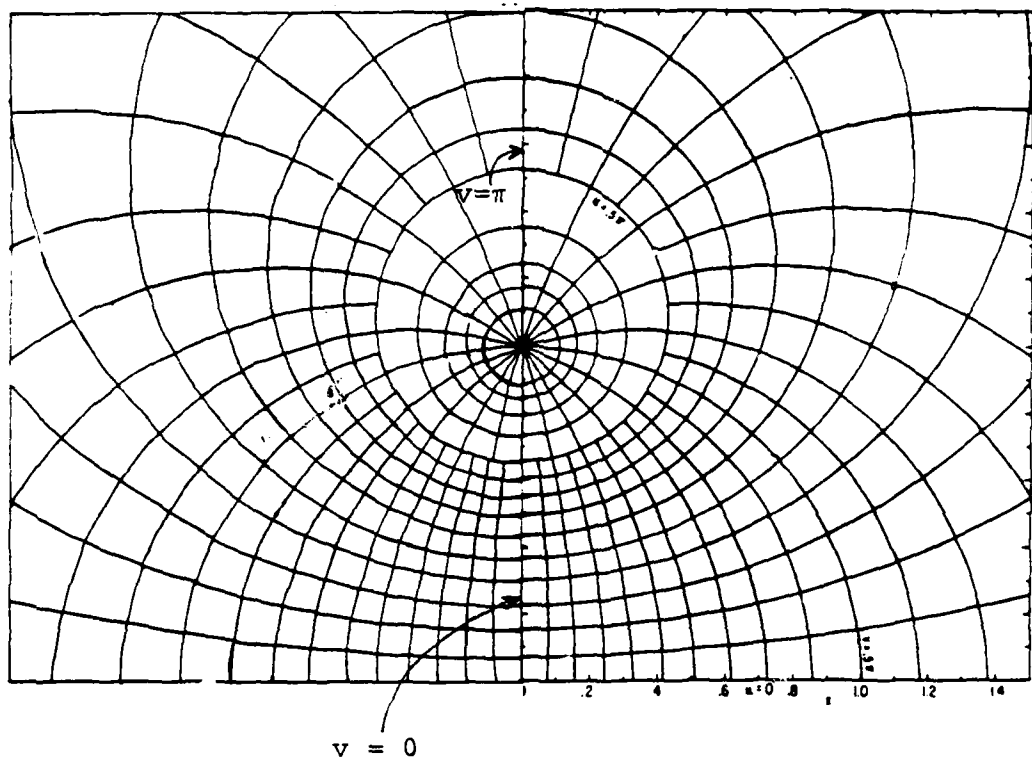
where  $f_g$  is a dimensionless geometric factor. This factor is given by

$$f_g = 2u_d / 2\pi \quad (40)$$

where  $2u_d$  is the potential difference between two wires and  $2\pi$  is the charge in  $v$  for a path circling one wire. This can also be observed in Figure 16b where the change in  $v$  around a conductor is seen to be  $2\pi$ .

If all the  $N_p$  peakers are required to be at the same potential  $u=u_0$ , this implies that the peaker arms are located on  $u=u_0$  line between  $v = \pm \pi$ . This is indicated in Figure 17 for several values of  $N_p$ . The two conditions during charge and

(a)  $z$ -plane



(b)  $w$ -plane

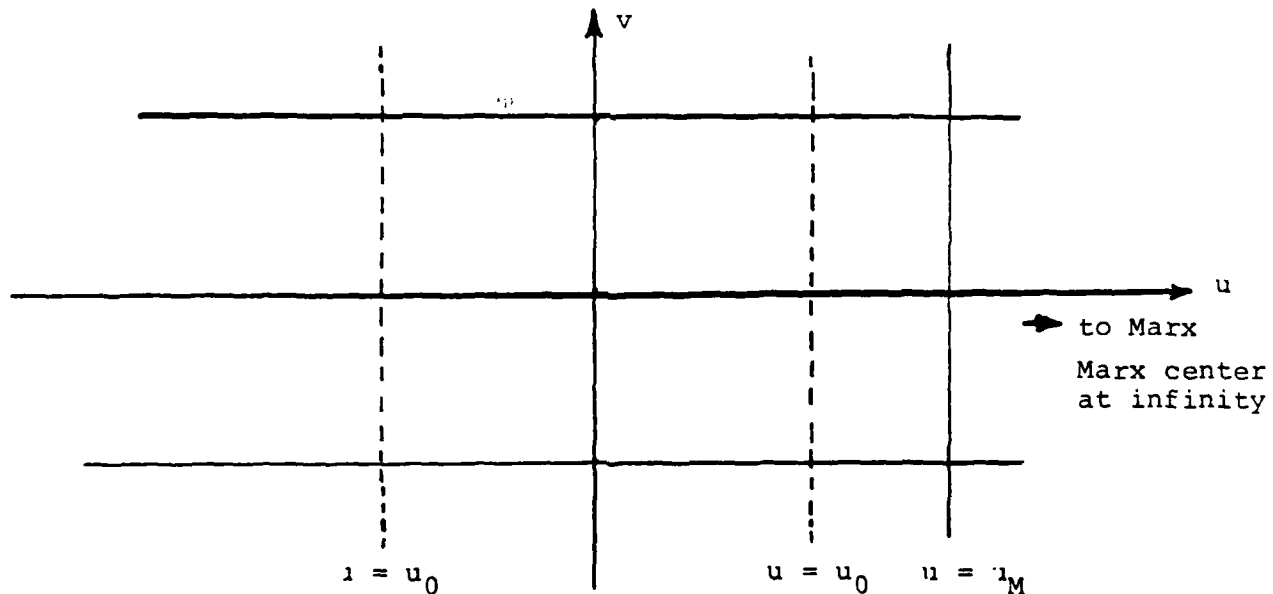


Figure 16. Conformal transformation of a single conductor (Marx column) above a ground plane.

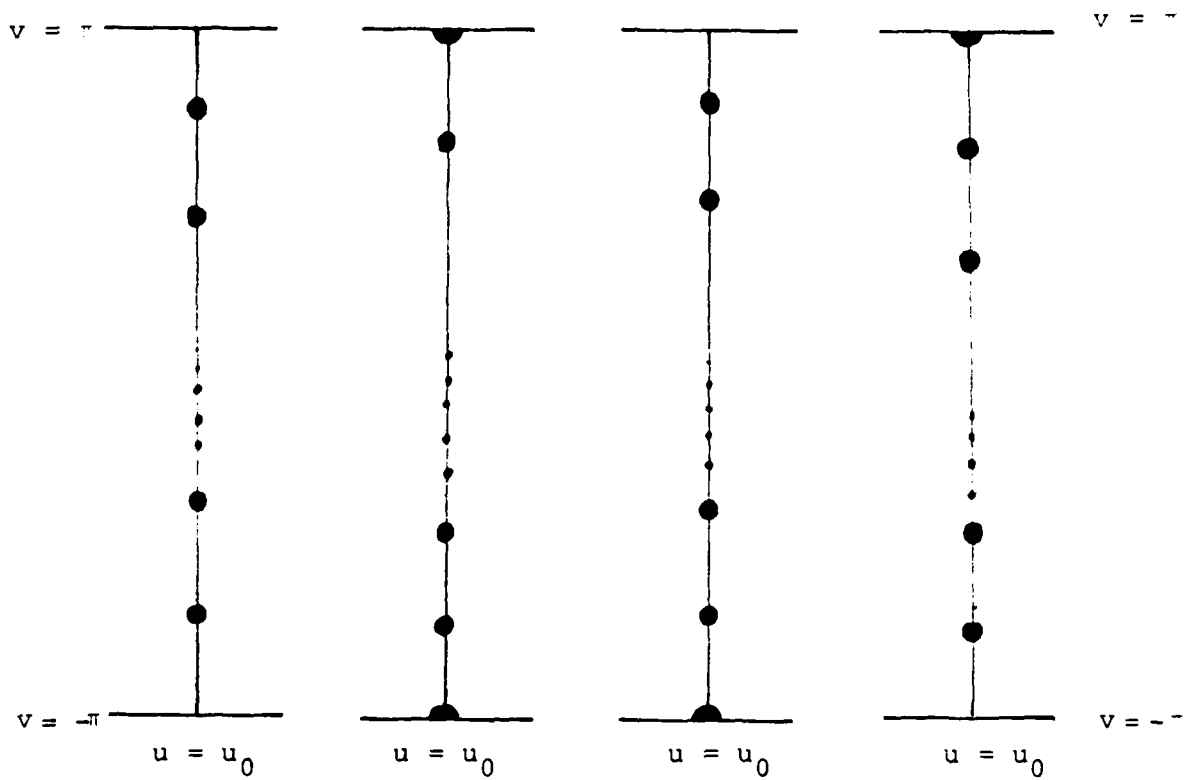


Figure 17. Possible peaker locations in the complex potential plane transformable back to the physical  $z$ -plane.

discharge cycle also implies that the peakers be located at physical locations on the constant potential surface such that the incremental change in  $v$ , between any two adjacent peakers is the same. To summarize, the peakers have to be located on constant  $u$  line but equally spaced in  $v$ -sense. For example, if one starts with  $N_p$  number of peakers, the procedure to find their optimum locations is as follows:

- (a) choose Marx center as  $(0,+1)$  in the  $z$ -plane
- (b) choose peaker to ground plane impedance say  
150  $\Omega$  (for ATLAS I or TRESTLE facility) giving  
 $f_p = 150 \Omega / 377 \Omega$ ,
- (c) choose the number  $N_p$  and radius  $r_p$  of peakers,
- (d) determine the new  $f_{p0}$  because of the number  $N_p$  of peakers. (Note that a planar approximation is adequate (Ref. 11), especially for  $N_p \leq 4$ )
- (e) on the new equipotential corresponding to  $f_{p0}$ , specify any one peaker center, say it is at  $v_0$ ,
- (f) then the remainder are at  $v_0 + (2\pi n / N_p)$

Some representative calculations, based on this procedure for the case of  $N_p = 6, 7, 8$  are presented in the following section,

##### 5. Numerical Results

In this paragraph, we shall illustrate the process of obtaining the peaker arm locations, by considering four numerical examples. Specifically, the three chosen values of  $N_p$  are 6, 7, 8. At this point, the optimum choice for  $N_p$ , itself is unknown. The question of how to select an optimum  $N_p$  will be addressed in Section V, where sample pulser output waveforms for step excitations are computed. Having been given a number  $N_p$ , the following steps enable one to obtain their location.

All linear dimensions are normalized such that the Marx center is at a height of unit distance above the ground plane. In this normalization scheme, the radius of the Marx conductor is about 0.2 and the following calculations are appropriate at a certain cross section in the transmission lines formed by Marx/peaker systems. For each of the three cases considered ( $N_p = 6, 7, 8$ ), all the peakers have initially a radius of 0.02. However, the  $N_p$  peakers are then replaced by a single equivalent peaker conductor with an effective radius of  $a_e$  and centered at  $(0, y_e)$ . The relevant equations, from earlier sections, are reproduced below.

$$\text{initial geometric factor; } f_p = z_L/z_0 \quad (41)$$

$$\text{with a corresponding initial equipotential contour } u=u_0 \\ \text{change in } f_p \text{ due to inter-peaker effects; } \Delta f_p = \Delta/(2N_p d) \quad (42)$$

$$\text{where, } \Delta \equiv \text{incremental equipotential change} = \frac{d}{\pi} \ln\left(\frac{d}{\pi r_p}\right) \quad (43)$$

$2d \equiv$  spacing between peakers

$$\text{iterated value of } f_{p1} = f_p + \Delta f_p = f_p + \left(\frac{1}{2\pi N_p}\right) \ln\left(\frac{d}{\pi r_p}\right) \quad (44)$$

$$\text{with its corresponding new equipotential } u_1 = (u_0 + \Delta u)$$

$$= u_0 + \frac{1}{N_p} \ln\left(\frac{d}{\pi r_p}\right) \quad (45)$$

Note that the peaker locations are uniquely specified if one determines the  $v_n$  for  $n = 1, 2, \dots, N_p$  when  $v_n$  is the imaginary part of the complex potential  $w = u+jv$ . Mathematically, locating that peaker arms in their optimum positions becomes one of finding the unknown  $v_n$ 's. Each  $v_n$  on the new equipotential surface  $u_1$ , corresponds to a set of values for  $(x_n, y_n)$  which are the locations of peaker centers.

The numerical results are shown in Table 4 where, the two conductor model is obtained for each of the three values of  $N_p$ . Equations (41) to (45) are used in computing the

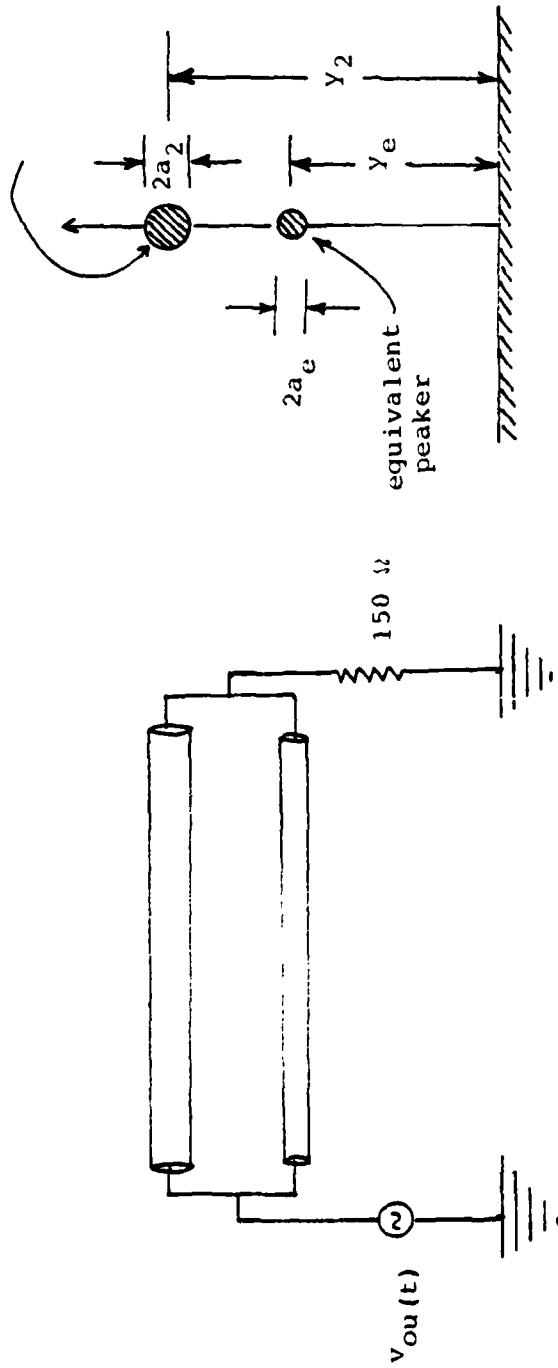


Figure 18. The two conductor model.

TABLE 4. COMPUTATION OF THE TWO CONDUCTOR MODEL

$N_p$	$y$	$a$	$f_p$	$u_0$	$\Delta f_p$	$\Delta u$	$u_1$	$y_e$	$a_c$
6	1	0.2	0.398	0.795	-0.135	-0.269	0.52	0.70	0.0148
7	1	0.2	0.398	0.795	-0.168	-0.335	0.46	0.62	0.0144
8	1	0.2	0.398	0.795	-0.190	-0.380	0.41	0.56	0.0134

parameters  $f_p$ ,  $u_0$ ,  $\Delta f_p$ ,  $\Delta u$ ,  $f_{p1}$  and  $u_1$ . These parameters are straightforward to get. However, the last two columns of TABLE 4, namely the parameters  $(a_e, y_e)$  of the equivalent peaker conductor shown in Figure 18, are somewhat involved and they are obtained graphically from Figure 16a. Knowing the new value  $u_1$  of the equipotential,  $y_e$  is easily read off the graph as the point where  $u = u_1$  intersects the y axis. Then on this  $u = u_1$  surface,  $N_p$  number of  $v_n$ 's are chosen according to

$$v_n = v_0 + (2\pi/N_p) \quad n = 1, 2, \dots, N_p \quad (46)$$

Note that because of rotational symmetry,  $v_0$  is somewhat arbitrary. In other words, once one of the peaker locations is selected, the remaining  $(N_p - 1)$  are located uniquely according to Equation (46).

$y_n$ 's are read from the graph corresponding to each  $v_n$ . The effective radius  $a_e$  of the equivalent peaker is then determined from Equation (37) reproduced below

$$a_e = r_p Y_e / \left( \prod_{n=1}^{N_p} y_n \right)^{1/N_p} \quad (47)$$

where  $r_p$  = radius of  $N_p$  speakers = 0.02 for the present.

In the following Section V, the two-conductor model computed here will be used in obtaining sample output waveforms. It is also noted that, in the actual situation at ATLAS I (TRESTLE) facility, the four peaker arms are not located in their optimum positions on an equipotential surface. It is expected that computations for reorienting the existing speakers, using the considerations outlined in this report will be done in a future effort.

## V. STUDY OF THE COUPLED TRANSMISSION-LINE MODEL

In the preceding Section IV, a coupled two-conductor-transmission-line model was developed to represent the Marx and peaker system above the ground plane. This two-conductor model will be utilized in this section to obtain sample output waveforms for the case of step excitation (Figure 18 associated with Table 4). The output voltage  $V_L(t)$  across the load  $Z_L$  ( $\approx 150 \Omega$ ) is computed using the well established code QV7TA described in Reference [15]. This code was developed to permit a transient analysis of relatively general multi-conductor transmission-line networks which are subject to either lumped source (like in the present application) or distributed field excitation. The input quantities are the geometry and the per-unit-length inductance and capacitance matrices. Since the code is based on detailed theoretical considerations of multiconductor transmission lines [12], the method of solution is not reproduced here. For the present case of two conductor transmission line, analytical approximations for  $V_L(t)$  can be obtained, but it was found efficient to simply use QV7TA for getting the load voltage (or current).

### 1. Two Velocities

Designating the equivalent peaker conductor by subscript 1 and the Marx conductor by subscript 2, the per-unit length matrices are denoted by

$$(L'_{n,m}) = \begin{pmatrix} L'_{11} & L'_{12} \\ L'_{21} & L'_{22} + L'_m \end{pmatrix} \quad (C'_{n,m}) = \begin{pmatrix} C'_{11} & C'_{12} \\ C'_{21} & C'_{22} \end{pmatrix} \quad (48)$$

As was derived earlier, the two velocities of propagation are given by

$$v_1 = c \quad \text{and} \quad v_2 = c \quad 1 + \frac{(L'_m \ L'_{11})}{(L'_{11} \ L'_{22} - L'_{12} \ L'_{21})} \quad (49)$$

It is noted that if the additional Marx inductance  $L_m'$  is neglected, the two velocities become identically equal to  $c$ , as one would expect. One can pursue this two-conductor model analytically to obtain the wave amplitudes. However, instead of this approach, for the present purposes, we have chosen to use the QV7TA code to analyze the two-conductor model, with the goal of computing the voltage  $V_L(t)$  across the load.

## 2. Waveform Optimization

The load  $Z_L$  ( $\approx 150 \Omega$ ) across which the output waveform is computed represents the simulator. Hence this waveform is indicative of the transient waveforms launched onto the simulator plates. The Figures 19, 20 and 21 respectively show the load voltage  $V_L(t)$  for the three cases corresponding to  $N_p = 6, 7, 8$ . The parameters of the equivalent peaker conductor are shown in the title of each figure. The top figures 19a, 20a and 21a are with the additional Marx inductance neglected and the bottom Figures 19b, 20b and 21b include the effect of the additional Marx inductance and the two modes of propagation.

## 3. Optimum Number of Peakers

It is clear from even a quick look at the effect of the additional Marx inductance in the bottom three figures, for the cases considered at least, this inductance has a significant adverse impact on the wave transport within the pulser system. A more careful examination of the figures also indicates that more numbers of peakers contributes to the quality of pulser output. First, the Marx and peakers are assumed to be parallel to the ground plane. In reality, they are not, indicating the need for more calculations of the present nature at other cross sections along the coupled transmission line formed by the Marx/peaker systems. Second, the Marx and peakers are modeled by cylindrical conductors. This approximation is not expected to be serious since the conformal transformation method uses line sources and the physical conductor is an equipotential surface.

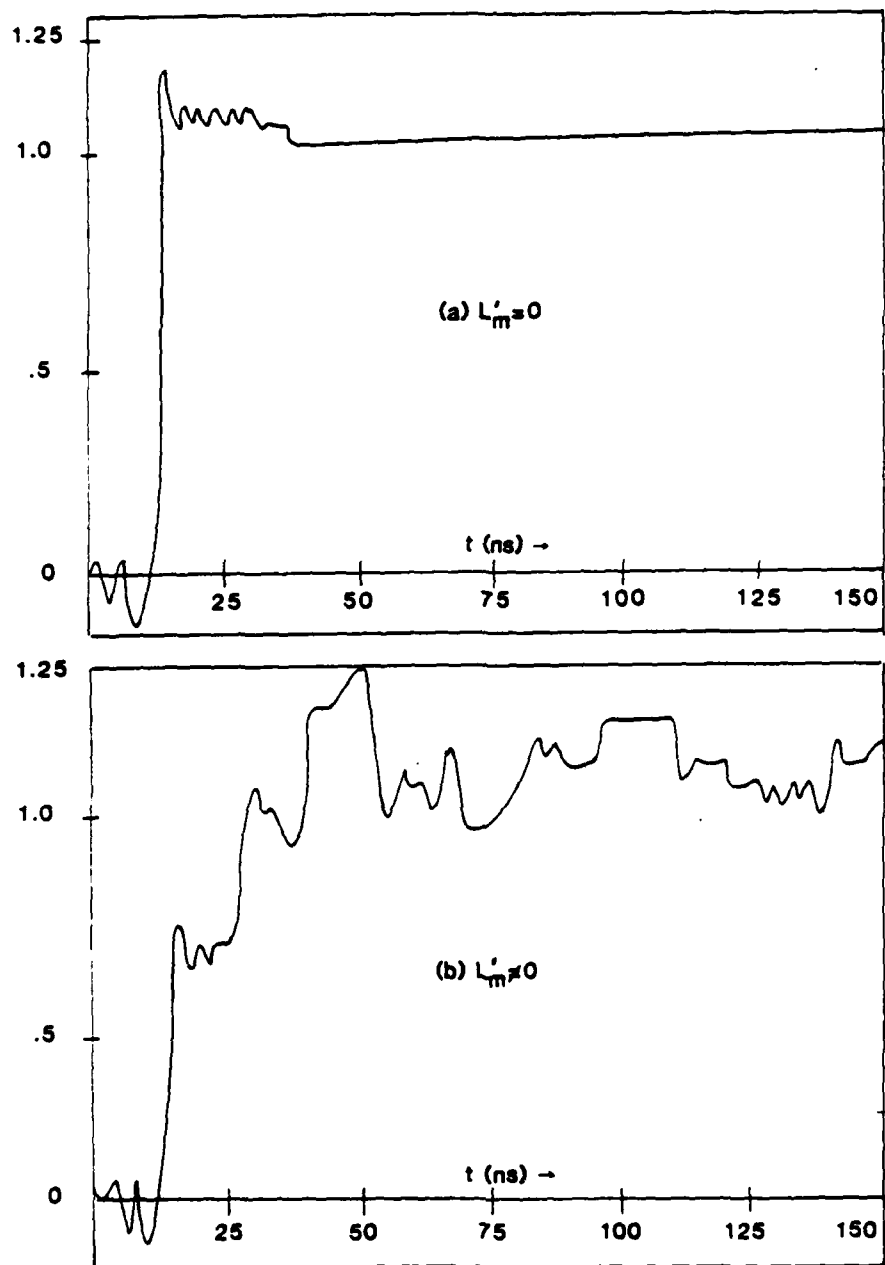


Figure 19. Pulser output  $V_L(t)$  waveform with Marx at  $(0, +1)$  and effective peaker at  $(0, .7)$  for  $N_p = 6$ .

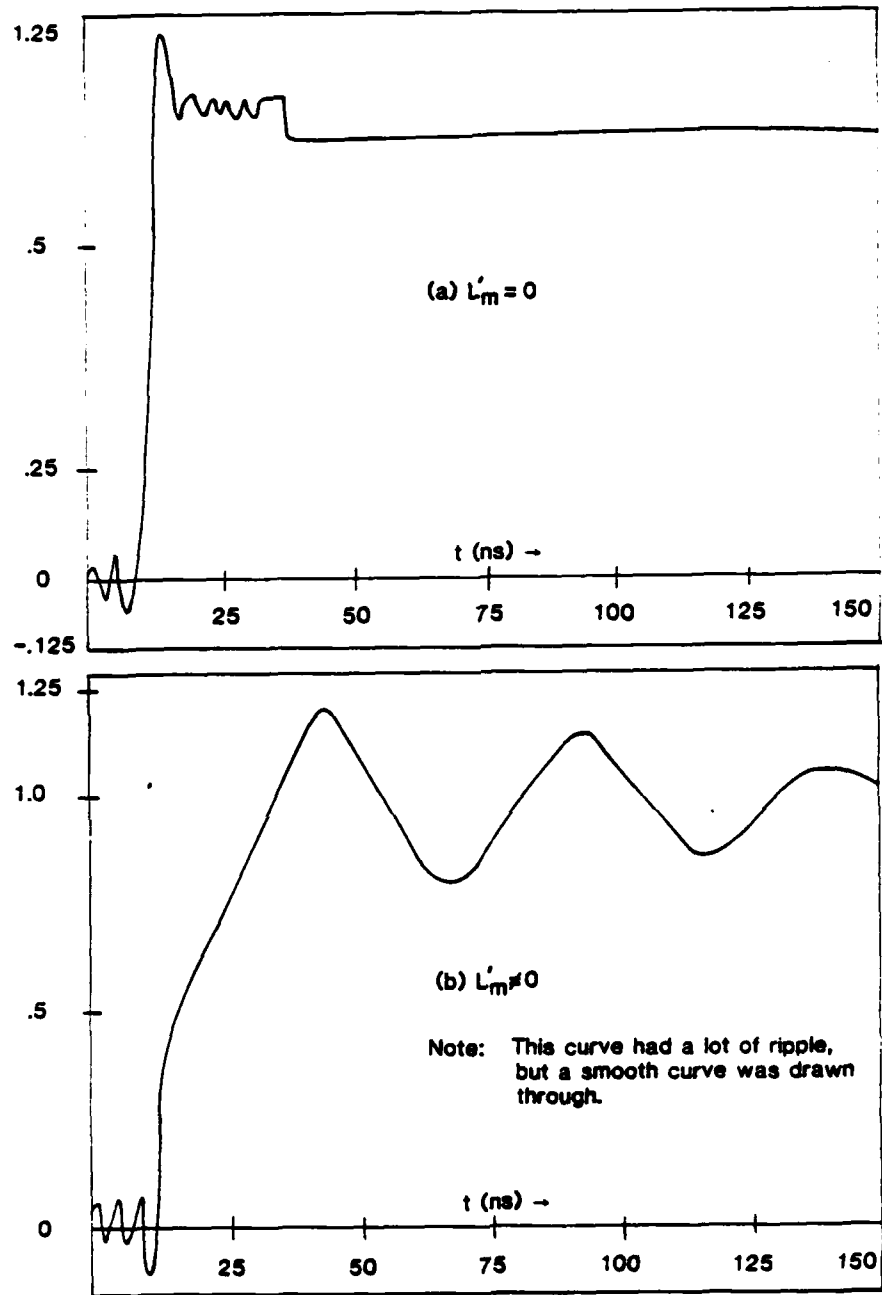


Figure 20. Pulser output  $V_L(t)$  waveform with Marx at  $(0, +1)$  and effective peaker at  $(0, .62)$  for  $N_p=7$ .

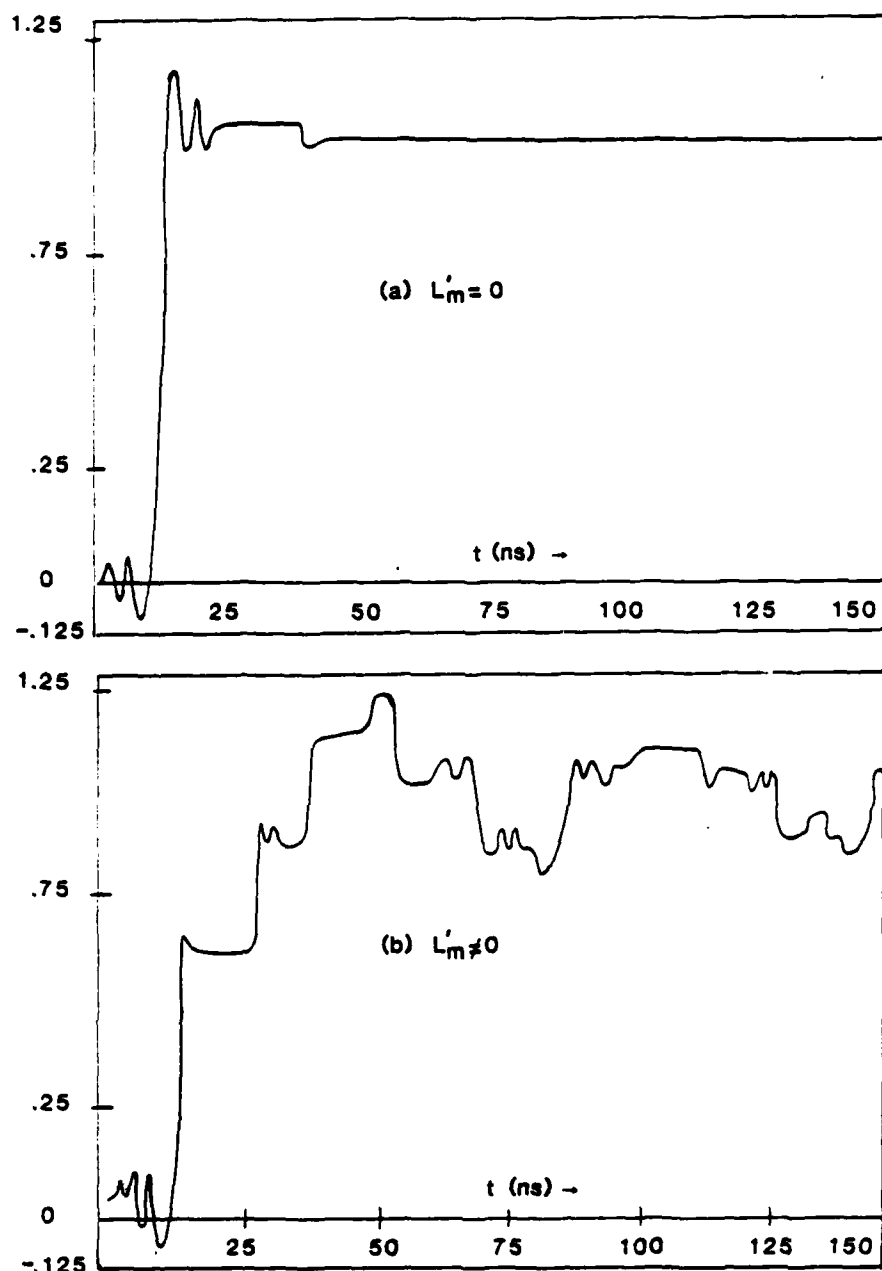


Figure 21. Pulser output  $V_L$  (t) waveform with Marx at  $(0, +1)$  and effective peaker at  $(0, .56)$  for  $N_p = 8$ .

In conclusion, it is observed that this report has placed the emphasis on developing the analytical tools for optimizing the peaker arms. The application of these methods to the actual facility parameters, coupled with some of the engineering modifications recommended in the following section, can contribute significantly to improving the pulser performance in the ATLAS I (TRESTLE) facility.

## VI. RECOMMENDATIONS FOR FUTURE WORK

The overall electromagnetic geometry of a pulser would necessarily involve impedance matching across each interface, as well as the transverse field distribution that matches as closely as is feasible to the next section of the pulser. This and other such criteria point toward a need for extensive and careful experimentation that would also bring out and resolve relevant problems. Some of the important experimental problems are listed and briefly discussed below.

### 1. Construct at PTF:

Construction of a PTF for full scale impedance hardware testing should be pursued to provide the means of testing production hardware outside the simulator facility. It would also be a valuable tool for maintenance testing of pulsers, and for refining or evaluating the performance.

### 2. Continue Analytical Studies:

In a few respects, there is a similarity of problems with the pulser and the simulator proper, while the pulser is viewed as a transmission line or wave transporting electromagnetic structure. At various interfaces, they both require analyses, leading to a better understanding of the interface properties in terms of computing (and possibly measuring) transverse field distributions, and adding compensating lumped elements or other engineering modifications to the structure. Another area, where analytical studies should continue, is to extend the calculations of the pulser output waveforms in this report, by an application of the theory of multiconductor transmission lines and associated existing computer codes [12,15]. Furthermore, carefully planned experiments often point out what further aspects of the pulser need to be analyzed.

and which other synthesis (design) concepts need to be developed.

3. Build Scale Model Pulser Components:

The modeling of the output switch and the transition can be the first in a series of modeling tasks. For example, several cones with circular and noncircular cross sections can be built and can be evaluated in mock-up experiments for their impedance as well as pulse-rise characteristics. The low impedance of the present monocone switch and the transition geometry from the output switch to the peaking capacitor arms is the most serious problem area with respect to rise time degradation. Fortunately, this area is also the easiest part of the problem to model. If one were to build a one-fifth scale model with sufficient transmission line to give 10 or 20 nanoseconds of measurement clear time, this area could be optimized reasonably fast. The cone tilt angle and ground plane shaping could be evaluated much easier on the model than on the facility. Once the optimum configuration is established, then the feasibility of modifying the facility can be carried out with more confidence.

The next addition to such an experimental study would be to add the mock-up transitions and varying them. Addition of Marx generator and peaking capacitor arms leads to difficulties in modeling, but can be done with some careful thought. The peaking capacitors could be made up of unimpregnated windings with the length of the winding adjusted to provide the same transit time characteristics as an impregnated winding. Using dry windings banded with tape instead of cased would minimize cost also. The position of the peaking capacitor arms could be easily varied in this model and the results compared to the calculations. If the correlation is good, it will validate the theoretical approach of the peaker arm optimization. Scale modeling is always a much more

cost effective approach to resolving problems than trying to reconfigure the actual hardware.

4. Electrical Characterization of Peakers

The work done years ago on peaker arm characterization (see Appendix A) should be pursued and a coaxial geometry can be considered in which the peaker arm will essentially become the inner conductor. By an application of the theory of coaxial transmission lines with lossy inner conductor, peaker arm electrical parameters can be experimentally determined at various frequencies. In this study, a lot of valuable data could also be obtained on dry capacitors at low voltage to avoid the expense of completely manufactured capacitors.

5. Explore Using Better HV Components:

Experimental evaluation of the benefits of using state-of-the-art components, e.g., better high-frequency capacitors illuminated triggering switches need to be pursued. In this regard, damping of unwanted resonances between peakers, or between Marx/peaker system, could be experimentally optimized by adding resistors or cross-strapping peakers to raise the resonant frequencies.

6. Experiments in the PTF:

After a successful optimization of components with the mock-up, the actual hardware with the modifications incorporated, should be evaluated in the PTF. This evaluation carried out at the fully rated voltage levels provides the basis for eventual modifications in the simulator facility.

7. Other Configurations:

The Marx pulser used in ATHAMAS II (or VPD II) facility wherein the central Marx column and the peaking capacitor system situated below the facility ground plane, has exhibited better rise characteristics. Of course, the

peaking capacitor in this case is a compact coaxial water dielectric store situated in the ground plane at the virtual apex of the facility morocone structure. Its low impedance in combination with its small dimensions provides for the system high frequency performance, contributing towards a pulse rise time of bettern than 8 ns.

Mock-up of such systems can be built and evaluated. Although a major reconfiguration of the pulser system in ATLAS I (TRESTLE) facility may be impractical, such studies are useful as design options, for future simulator facilities.

#### 8. Study of Pulser Arrays:

It is emphasized that pulser frequency spectrum is very important to the quality of simulation. Environmental improvements can be derived by increasing the number of pulsers (Ref. 5), in the form of two arrays (4 x 4 each). However, the pulser array geometry affects the high frequencies significantly, calling for careful paper-studies. Large pulsers and pulser arrays can not be considered (Ref. 2) as point or ideal sources for launching high frequency TEM waves on cylindrical or conical transmission line structures. One of the options that can be considered is a 4 x 4 array of the pulser modules feeding each of the two conical input transitions on the sides of the central ground plane wedge of ATLAS I (TRESTLE) facility. While this doubles the voltage for each conical transmission line, one should ailow for some high frequency degradation. Clearly, this aspect of pulser technology dealing with arrays needs further investigation.

## REFERENCES

1. C.E. Baum, "Pulse Power Problems with Respect to EMP Simulators," Pulse Power Memo 1, 5 June 1977.
2. C.E. Baum, "Electromagnetic Considerations for Pulser Design," ATLAS Memo 10, 6 April 1974.
3. C.E. Baum, D.F. Higgins and D.V. Giri, "Pulser Test Results and Preliminary Estimation of Transient Electric Field Waveforms in ATLAS I," ATLAS Memo 18, 7 October 1976.
4. J.P. Castillo, K.C. Chen and C.E. Baum, "Relation of Rise Time Definitions for Various Waveforms," ATLAS Memo 20, 4 November 1976.
5. C.E. Baum and D.V. Giri, "Environmental Improvements in ATLAS I Derivable from Potential Pulser Improvements," ATLAS Memo 21, 13 December 1976.
6. C.E. Baum, D.V. Giri and K.C. Chen, "An Overview of EM Considerations of ATLAS in the Context of Current and Future Efforts," ATLAS Memo 22, 5 January 1977.
7. R.W. Latham, M.I. Sancer and A.D. Varvatsis, "Matching a Particular Pulser to a Parallel-Plate Simulator," Circuit and Electromagnetic System Design Note 18, November 1974.
8. C.E. Baum, "The Conical Transmission Line as a Wave Launcher and Terminator for a Cylindrical Transmission Line," Sensor and Simulation Note 31, January 1967.
9. W.R. Smythe, Static and Dynamic Electricity, McGraw-Hill Book Company, Inc., New York, 1950.
10. S.A. Schelkunoff and H.T. Friis, Antennas: Theory and Practice, Wiley 1966, Section 4.6, pp. 104-106.
11. C.R. Paul and A.E. Feather, "Computation of the Transmission Line Inductance and Capacitance Matrices from the Generalized Capacitance Matrix", IEEE Trans. on Electromagnetic Compatibility, Vol. EMC-18, No. 4, pp. 175-183, November 1976.
12. C.E. Baum, T.K. Liu and M.F. Tesche, "On the Analysis of General Multiconductor Transmission-Line Networks", Interaction Note 350, November 1978.

#### REFERENCES

13. C.E. Baum, "Impedances and Field Distributions for Symmetrical Two Wire and Four Wire Transmission Line Simulators", Sensor and Simulation Note 27, 10 October 1966.
14. C.E. Baum, "Impedances and Field Distributions for Parallel Plate Transmission Line Simulators", Sensor and Simulation Note 21, 6 June 1966.
15. F.M. Tesche and T.K. Liu, "User Manual and Code Description for QV7TA: A General Multiconductor Transmission-Line Analysis Code", Interaction Application Memo 26, August 1978.

APPENDIX A

TRESTLE PULSER MODULE  
TECHNICAL MEMORANDUM  
ON  
ANALYSIS OF TRESTLE PEAKING CAPACITORS  
OVER THE FREQUENCY RANGE OF  
1 to 100 MHz

In this Appendix, TRETM-12 document, which was originally prepared by Maxwell Laboratories, in July 1974 has been included in its entirety. This document deals with the analysis of peaker arms in the frequency range of 1 to 100 MHz.

## INTRODUCTION

The peaking capacitor has been identified as a potential source of some of the performance problems observed in the prototype pulser. Therefore, a complete experimental and analytical investigation has been initiated to identify all potential problem sources within the peaking capacitors.

The output waveform from the prototype pulser as measured in the PTF is shown in Figure A.1. The problems of concern are as follows:

1. The prepulse measured is approximately 35 percent higher than predicted in the original design analysis.

While this is not a critical problem it does reduce the amplitude of the fast rise portion of the pulse, which translates to a loss of high frequency energy. The prepulse was analyzed in TRETM 3, which concluded that the prepulse could be reduced about 20 percent by shortening the peaking capacitors by a factor of 2. This design change was rejected at the time because of the voltage flashover problems discussed in TRETM 1.

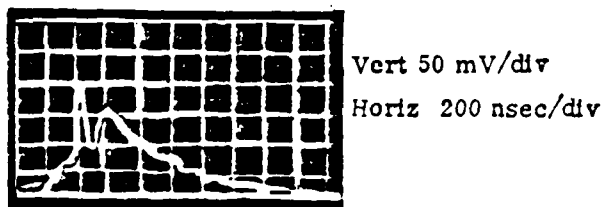
2. The severe dip in the waveform just past peak results in a significant loss of energy in the frequency domain between 10 and 20 MHz.

The dip in the waveform of Figure A.1 is typical of a peaking circuit output when the output switch is closed later than the optimum time or, where the value of the peaking capacitor is too small.

A test series covering a matrix of peaking capacitor values and switching times is being accomplished. The objective is an empirical evaluation and selection of the optimum switching time and peaking capacitor value.

The results of this testing will be reported in a separate TRETM. The initial indications are that the dip can be eliminated by increasing the value of the peaking capacitor system from 270 pF to 606 pF. However, all analysis of the circuit and

a



b



Figure A1. Pulser module output waveform.

calculations based on the circuit parameters indicate that the proper value should be 270 pF. Therefore, until this disagreement is resolved, it cannot be concluded that increasing the peaking capacitor value is the proper course of action to correct the problem.

3. The risetime is significantly slower than that required to meet the performance goals.

This problem is the one of most critical concern. Part of the risetime problem has been attributed to the geometry of the output switch and steps have been taken to improve performance in this area. The discussions covering the switch problem are presented in TRETM's 4 and 5. The change involved converting from a bicone geometry to a monocone geometry for the output switch.

The slow risetime implies the absence of high frequencies. The TRESTLE Pulse Module is designed such that the peaking capacitors form one plate of the conic transmission line between the output switch and the PTF. Therefore, to preserve the high frequencies launched by the output switch at the output of the pulser, the peaking capacitors must pass all frequencies of interest with a minimum of attenuation and delay.

It is apparent in the test data to date that the output switch spark channel is generating a sufficient risetime to achieve the pulser performance goals. It has been established that reflections in the bicone switch, and diffraction from the transition between the switch and peaking capacitors is degrading the switch risetime. It has not been determined what effect, if any, the peaking capacitors have on the risetime. This is the subject of this TRETM.

#### ANALYSIS OBJECTIVE

It is the objective of this analysis to look at the peaking capacitor in terms of performance over the frequency range of 1 to 100 MHz. The analysis will be pointed toward identifying all characteristics of the capacitor that may be related to some frequency within the range of interest. The results of

the analysis will then be compared to the results of laboratory tests conducted on the peaking capacitors. The tests conducted and data obtained are presented in TRETM 11.

The ultimate goal of the analysis is to present a firm conclusion and recommendation, with respect to whether a redesign of the peaking capacitor is necessary to meet the TRESTLE performance requirements.

#### CAPACITOR DESCRIPTION

The capacitor is a standard MLI product, Catalog Number 31261. The published characteristics are as follows:

Capacitance:	0.000606 $\mu$ F $\pm 10\%$
Voltage:	550 KVDC, Pulse Charge
Inductance:	$\sim 300$ nH
Voltage Reversal:	20%, Maximum
Temperature Range	
Operating:	14° F to 113° F
Storage:	-40° F to 113° F
Weight:	$\sim 7.8$ pounds

These characteristics are normally all that are of interest when specifying a capacitor. Performance with respect to frequency is not given, nor has it ever been analyzed. The capacitor used in TRESTLE was selected based on its use in the TORUS Pulser, where there was no apparent problem due to the peaking capacitors.

The type of construction used in the capacitor is essentially standard. The method of holding the capacitor windings together and portions of the impregnation process are unique to the TRESTLE capacitor. Some of the processes are patented by MLI.

Physically the capacitor and its internal configuration are shown in Figure A.2. The pad shown in A.2a is the basic element of the capacitor. 15 of these pads are assembled into the subassembly shown in Figure A.2b. Then 5 of the

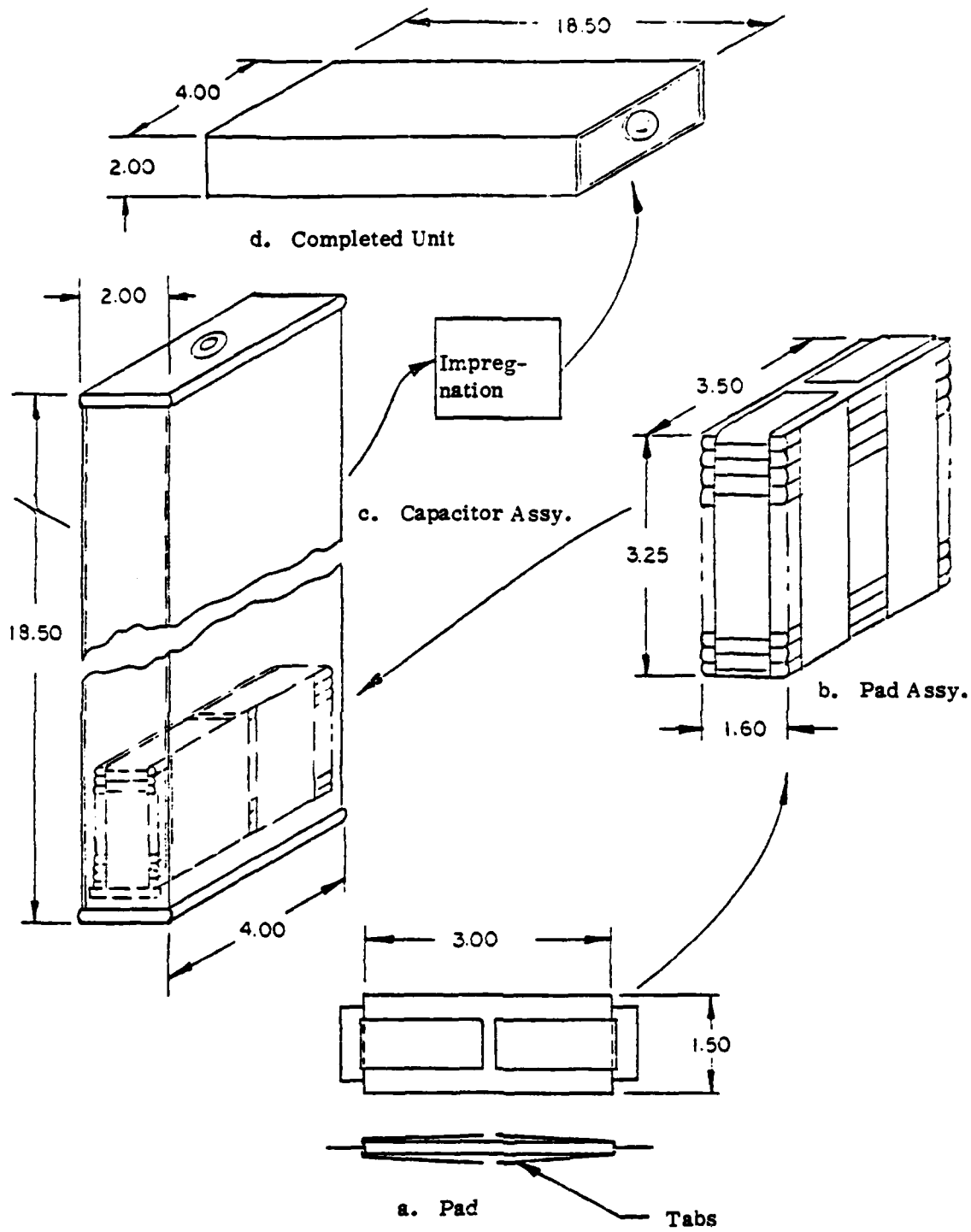


Figure A2. Peaking capacitor assembly.

subassemblies are assembled into the capacitor case as shown in A.2c. The capacitor is then put through the impregnation processes and the dimensions of the final assembly are shown in A.2d.

Thus, the capacitor contains 75 pads connected in series to achieve the final operating voltage of 550 kV.

#### ANALYSIS OF PEAKING CAPACITORS

The peaking capacitors being a part of the high frequency circuit for the pulser module must either be identified or eliminated as part of the risetime problem. Since there is not existing data on the characteristics of the peaking capacitors with respect to frequency, these must be determined before any conclusions can be drawn.

The best place to begin is with the smallest element of the capacitor, which is the basic winding or more commonly referred to as the pad.

#### CAPACITOR WINDING

To begin with, consider the winding before it is wound into a pad. Figure A.3a shows the two active foils. The dimensions of the foils and spacing between them is also given in Figure A.3a.

For some frequencies, the pad can be considered a parallel strip line. The dielectric constant,  $\sqrt{\epsilon}$ , in the strip line for this dielectric system is 4.25. The impedance of this strip line can be approximated by:

$$Z_{\text{pad}} \approx \frac{377 b}{\sqrt{\epsilon} a} \quad (\text{A.1})$$

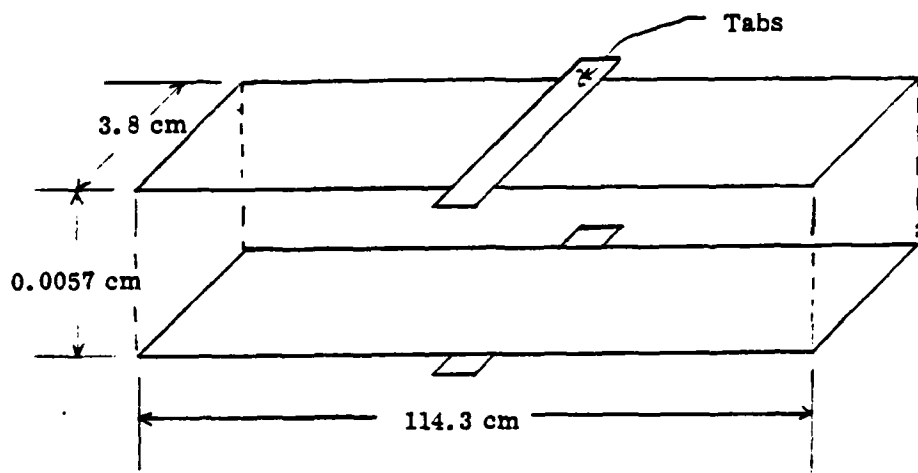
where

a = the width of the foils.

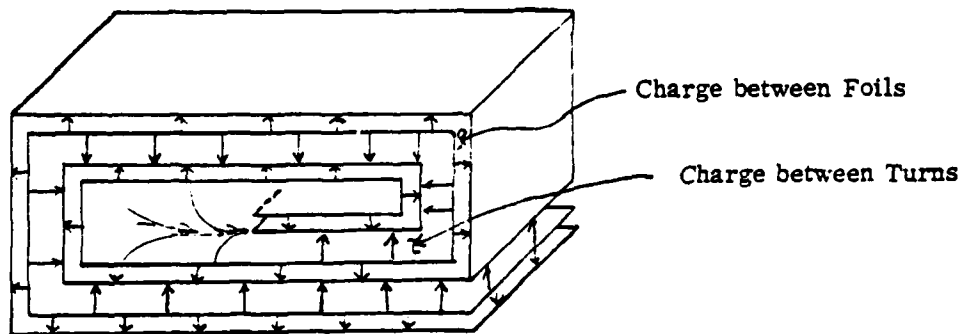
b = the separation of the foils.

$\epsilon$  = the dielectric constant between the foils.

377 = the impedance of free space.



a. Unrolled Capacitor Pad Active Foil



b. Rolled Capacitor Pad

Figure A3. Peaking capacitor characteristics.

Thus for the TRESTLE pad

$$z_{\text{pad}} = \frac{377 \times 5.7 \times 10^{-3}}{4.25 \times 3.8} \quad (\text{A.2})$$
$$= 2.7 \times 10^{-1} \text{ Ohms}$$

The electrical length of the strip line is somewhat longer than its physical length due to the dielectric constant between the foils. This also can be approximated by

$$T_l = \frac{l \sqrt{\epsilon}}{30} \quad (\text{A.3})$$

where

- $T_l$  = the transit time in nanoseconds.
- $l$  = physical length of line in centimeters.
- $\epsilon$  = the dielectric constant.
- 30 = velocity of light in cm/ns.

Thus

$$T_l = \frac{114.3 \times \sqrt{4.25}}{30} \quad (\text{A.4})$$
$$= 7.9 \text{ nsec}$$

So far the pad has been treated only as a flat strip line. The impedance and transit time of the pad are both modified by placing the tabs at the center of the line. By doing this and looking into the strip line at the middle, it now looks like a line that is half as long and half the impedance. Therefore, the strip impedance is now  $1.4 \times 10^{-1}$  ohms, and has an electrical length of about 4 nsec.

The capacitance length of the line is modified again, however, when the pad is rolled to use in the capacitor. As shown by the arrows in Figure A.3b, when the pad is rolled, another

strip line is formed between the turns of the winding. This is shown in simple schematic form in Figure A.4

The effective length of the line is modified again, however, when the pad is rolled to use in the capacitor. As shown by the arrows in Figure A.3b, when the pad is rolled, another strip line is formed between the turns of the winding. This is shown in simple schematic form in Figure A.4.

The capacitance and transit time of the pad are both approximately doubled when the strip line is rolled.

To this point, the following parameters for a single pad have been established.

$$Z_{Pad} = 1.4 \times 10^{-1} \text{ Ohms.}$$

$$T_L = 7.9 \text{ nsec.}$$

$$C_{Pad} = 45.5 \text{ nF (606 pF} \times 75 \text{ pads)}$$

Knowing  $Z_{Pad}$  and  $C_{Pad}$ , the inductance of the pad can be estimated from:

$$Z_{Pad} = \sqrt{\frac{L_{Pad}}{C_{Pad}}} \quad (\text{A.6})$$

where

$$\begin{aligned} L_{Pad} &= Z_{Pad}^2 C_{Pad} \\ &= 1.4 \times 10^{-1} \times 4.6 \times 10^{-8} \\ &= 9.0 \times 10^{-10} \text{ H} = 0.9 \text{ nH} \end{aligned} \quad (\text{A.7})$$

The parameters established so far can now be related to frequency and those frequencies identified that may be of interest.

The length of the pad as a transmission line is of special interest. The frequency at which the line represents a full wavelength is

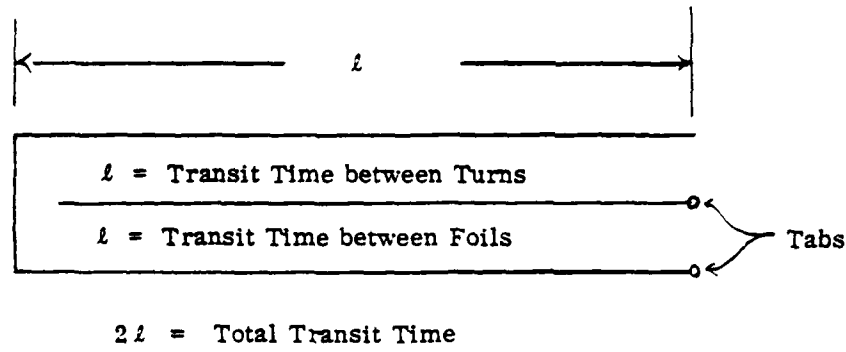


Figure A4. Schematic representation of rolled pad as transmission line.

$$\begin{aligned} f_{\lambda} &= \frac{1}{T_2} \\ &= 126.6 \text{ MHz} \end{aligned} \tag{A.8}$$

1/2 wavelength

$$\begin{aligned} f_{\lambda/2} &= \frac{1}{2T_2} \\ &= 63.3 \text{ MHz} \end{aligned} \tag{A.9}$$

1/4 wavelength

$$\begin{aligned} f_{\lambda/4} &= \frac{1}{4T_2} \\ &= 31.7 \text{ MHz} \end{aligned} \tag{A.10}$$

Another frequency of interest is the lumped element resonance of the pad inductance and capacitance.

From

$$f_{\text{Pad}} = 2\pi \sqrt{\frac{1}{L_{\text{Pad}} C_{\text{Pad}}}}$$

we have

$$\begin{aligned} f_{\text{Pad}} &= \frac{1}{2\pi \sqrt{0.0 \times 10^{-10} \times 45.5 \times 10^{-9}}} \\ &= 24.9 \text{ MHz} \end{aligned}$$

Thus, so far the following frequencies can be associated with the capacitor pads:

24.9 MHz - Lumped element resonance.  
37.1 MHz - 1/4 wavelength line.  
63.5 MHz - 1/2 wavelength line.  
126.6 MHz - full wavelength line.

It would appear from this, that for frequencies above 31.7 MHz, where the peaking capacitors begin to look like transmission lines connected in series, that its characteristics become very complex and difficult to analyze. This is further complicated by having 75 pads in each capacitor and a total of 675 pads in each peaking capacitor arm.

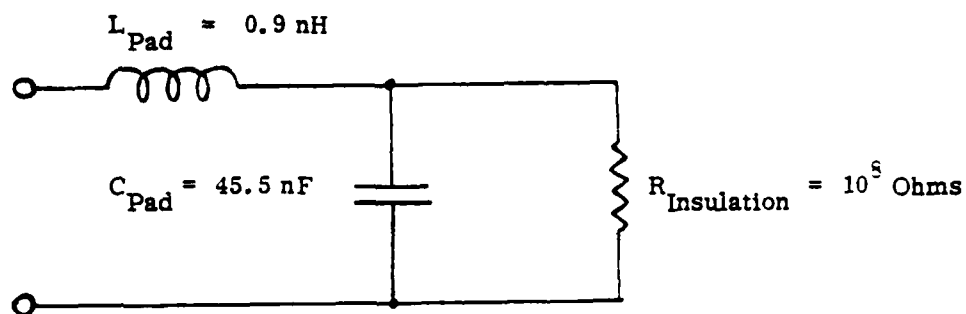
To this point, only a single pad has been considered in the analysis. The analysis so far indicates a pad could be represented as the lumped circuit shown in Figure A.5a up to frequencies of about 30 MHz. Above 30 MHz, it would be more properly represented by a transmission line as shown in Figure A.5b.

#### PEAKING CAPACITOR

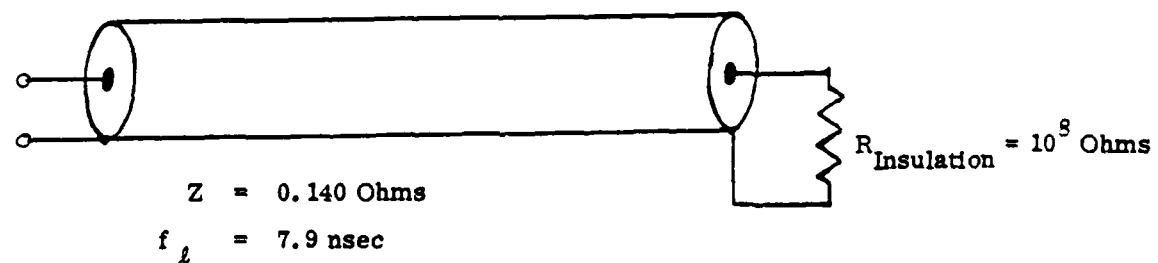
As mentioned before, a peaking capacitor is made by connecting 75 pads in series. The next step in the analysis is to determine what changes or additional characteristics may show up when this is accomplished.

For the single pad, no consideration was given to the connection tab inductance. When the pads are connected in series, this inductance is a part of the total series inductance of the capacitor. In fact, it is usually the largest inductance in the capacitor. The total series inductance of the capacitor has been established through test and measurement to be about 270 nanohenries.

The inductance of the pad was estimated at 0.9 nanohenries from the previous impedance calculation. The inductance of 75 pads in series would be 67.5 nanohenries, leaving 202.5 nanohenries unaccounted for in the capacitor. If this is assigned to the connecting tabs, it amounts to 2.7 nanohenries



a. Circuit for Frequencies below 30 MHz



b. Circuit for Frequencies above 30 MHz

Figure A5. Equivalent circuits for pad.

of tab inductance per pad. This is not an unreasonable value for the 1/2 inch tabs, and so for the time being, will be used.

The stacking of pads in series and the addition of tab inductance creates a new complexity in the analysis. Figure A.6 shows a lumped element equivalent circuit of the peaking capacitor with the inductance of the connecting tabs,  $L_{Tab}$ , between the individual pad circuits.

A condition now exists where  $L_{Pad} + L_{Tab}$  establishes another resonant frequency, which is also the resonant frequency of the total peaking capacitor,  $f_{pc}$ .

$$\begin{aligned} f_{pc} &= \frac{1}{2\pi \sqrt{(L_{Pad} + L_{Tab}) \times C_{Pad}}} \\ &= \frac{1}{2\pi \sqrt{(2.7 + 0.9) \times 10^{-9} \times 45.5 \times 10^{-9}}} \\ &= 12.4 \text{ MHz} \end{aligned}$$

(A.13)

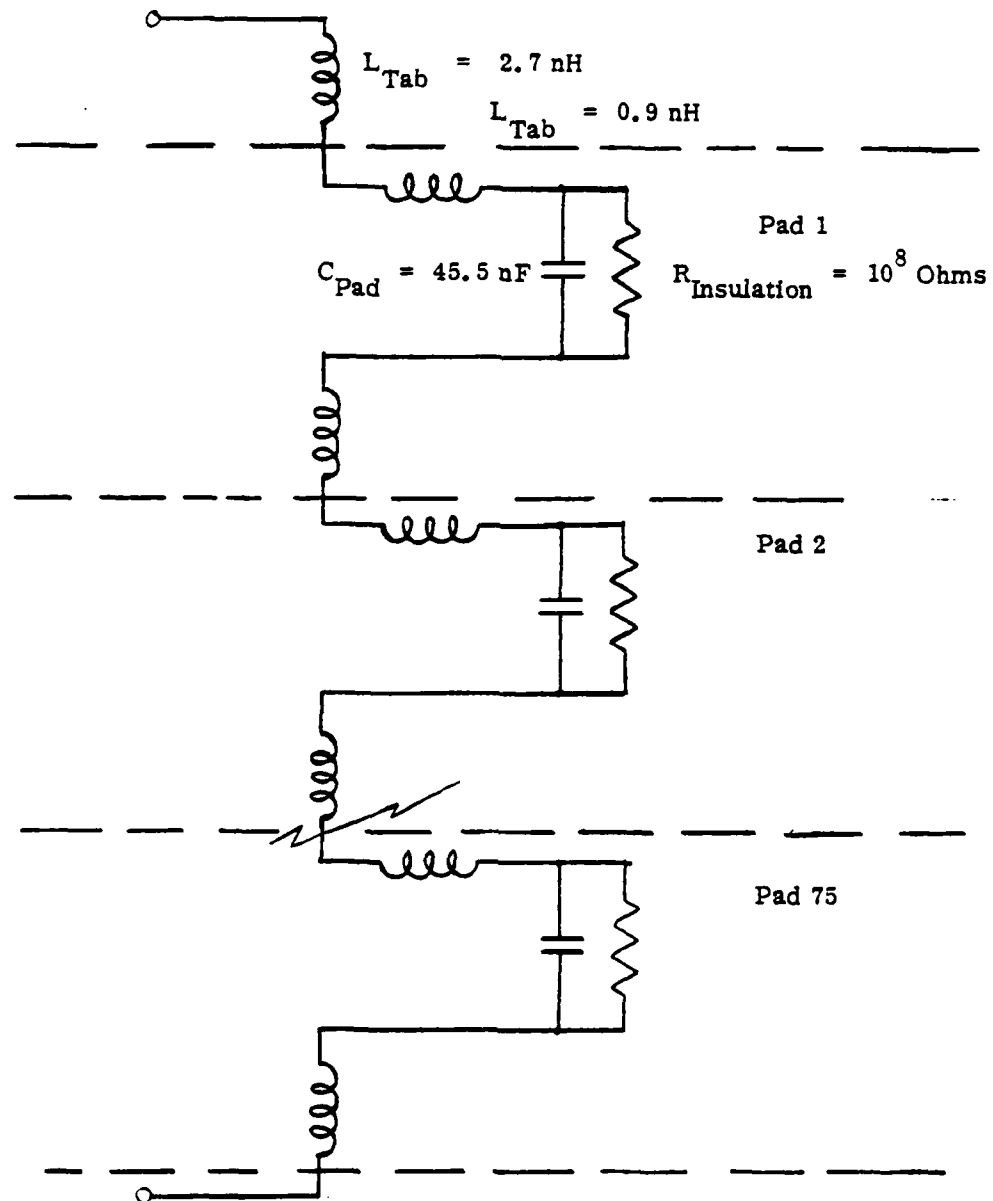


Figure A6. Lumped element equivalent circuit of peaking capacitor.

TABLE A1. RESULTS OF AMPLITUDE/PHASE TEST

Freq. MHz	SINGLE BREAKING CAPACITOR				9 CAPS SERIES		
	V <sub>out</sub> V <sub>in</sub>	Phase Shift Out	ns/deg	Total Delay ns	V <sub>out</sub> V <sub>in</sub> Calculated	V <sub>out</sub> V <sub>in</sub> Measured	Atten. db
1	.34	+73.4	2.780	-200.0	.00	.01	40.0
2	.57	+60.6	1.390	- 84.0	.01	--	--
3	.72	+49.4	.926	- 46.0	.05	--	--
4	.76	+39.9	.694	- 28.0	.08	--	--
5	.87	+31.5	.556	- 18.0	.29	.05	26.0
6	.90	+24.3	.463	- 11.0	.30	--	--
7	.93	+18.6	.397	- 7.4	.52	--	--
8	.94	+13.0	.347	- 4.5	.57	--	--
9	.95	+ 7.9	.309	- 2.4	.63	--	--
10	.96	+ 3.2	.278	- .9	.69	.17	15.4
11	.97	- 1.1	.253	.3	.76	.22	13.2
12	.97	- 5.2	.231	1.2	.76	.30	10.5
13	.98	- 9.6	.214	2.1	.83	.40	8.0
14	.98	-13.4	.198	2.7	.83	.44	7.1
15	.98	-17.8	.185	3.3	.83	.66	3.6
16	.98	-22.1	.174	3.8	.83	.72	2.9
17	.97	-27.2	.163	4.4	.76	.70	3.1
18	.96	-32.3	.154	5.0	.69	.61	4.3
19	.92	-37.3	.146	5.5	.47	.45	6.9
20	.83	-43.2	.139	6.0	.19	.22	13.2
21	.70	-37.5	.132	5.0	.04	.04	28.0
22	.67	-30.0	.126	3.8	.03	.01	40.0
23	.69	-21.8	.121	2.6	.04	.00	>40.0
24	.72	-24.1	.116	2.8	.05	.02	34.0
25	.68	-18.0	.111	2.0	.03	.02	34.0
26	.79	-12.2	.107	1.3	.12	.06	24.4
27	.87	-18.0	.103	1.9	.29	.18	14.9
28	.90	-21.5	.099	2.4	.39	.34	9.4
29	.93	-28.7	.096	2.8	.52	.48	6.4
30	.94	-32.5	.093	3.0	.57	.54	5.4
35	.96	-47.3	.079	3.7	.60	.60	3.2
40	.96	-59.3	.069	4.2	.69	.60	3.2
45	.97	-72.1	.062	4.5	.76	.70	3.1
50	.97	-88.0	.056	4.9	.76	.69	3.2
55	.98	-92.2	.051	4.7	.83	.67	3.5
60	.98	-100.4	.046	4.6	.83	.65	3.7
65	.97	-109.4	.043	4.7	.76	.60	4.4
70	.95	-121.9	.040	4.9	.63	.54	5.4
75	.93	-137.0	.037	5.1	.52	.45	6.9
80	.87	-146.8	.035	5.1	.29	.22	13.2
85	.74	-151.4	.033	5.0	.07	.07	23.1
90	.83	-155.3	.031	4.8	.19	.25	12.0
95	.90	-165.8	.029	4.8	.39	.36	8.9
100	.92	-177.6	.028	5.0	.47	.42	7.5
105	.93	-188.0	.026	4.9	.52	.43	7.3
110	.94	-200.0	.025	5.0	.57	.38	8.4

APPENDIX B  
LOW VOLTAGE SPRING TESTS  
(March - April 1974)

In this Appendix, we have reproduced with the kind permission of Mr. Floyd R. Graham of Maxwell Laboratories, the Appendix D of Maxwell Lab.'s Report No. MLR-483, dated November 1975. The results of the prototype pulser module testing in the PTF were discussed in that report and the Appendix deals with the three basic experimental tests performed in the PTF.

## LOW VOLTAGE SPRING TESTS (MARCH-APRIL 1974)

### A. INTRODUCTION

#### 1. Background

This appendix presents the results of three basic tests performed at the PTF and referred to collectively as the low voltage spring tests. The three tests were sequential in nature directed at the establishment of a decision making data base relative to design changes for improving pulser performance and establishing ideal pulse performance in the PTF versus the horizontal simulator. The experiments discussed in this appendix were executed in parallel with an analytical effort directed at providing a similar data base to that provided experimentally so that compatibility between analytical and experimental results can be demonstrated. Once this basic compatibility has been demonstrated, the prediction of the expected pulser performance in the horizontal simulator can be made with established confidence levels.

The three experimental tasks covered in this appendix can be summarized as follows:

- (1) Conic Test - Peakers and switch replaced with conic section having best impedance match with output transition for the PTF geometry (125 ohms).
- (2) Peaker Test - Peakers replaced with 2-1/2-inch aluminum tubes and tube geometry varied to minimize the impedance mismatch.
- (3) Cone Test - Vary monocone impedance and tilt angle to minimize impedance mismatch and compare with the bicone configuration.

## 2. Objectives

The objectives of the three basic test configurations considered in this appendix are summarized according to each test in the following:

- (1) Conic Test - The objective of the conic test was to determine the effects of the output transition and angle bend on pulser performance.
- (2) Peaker Test - The objectives of this test were to determine the optimum peaker geometry and the difference, if any, between the optimum geometry for the actual peakers or conducting tubes.
- (3) Cone Test - The objective of the cone tests was to determine the optimum configuration and cone angle output switch cone. Waveform performance sensitivity to switch impedance was also investigated.

## 3. Evaluation Criteria

Two criteria were used to evaluate the various pulser configurations. One was risetime and the other was waveform integrity. A configuration yielding the smallest risetime with minimum waveform perturbations due to reflected or diffracted components was judged as superior.

The time of arrival of a waveform perturbation due to diffraction or reflection relative to the waveform epoch can help identify the source of waveform degradation. Thus, time difference is used frequently in this appendix as a diagnostic tool.

Four field monitor locations were used in these tests. These locations provide two functions. One is to remove ambiguities in the time difference diagnostic. The other is to record the waveform variation as a function of position.

## B. PULSER CONFIGURATIONS

### 1. PTF Geometry

The geometry and dimensions of the PTF, giving the relative field sensor locations, is illustrated in Figure D-1. This figure indicates that there are three basic field measurement locations  $P_1$ ,  $P_2$ , and  $P_3$ . Locations  $P_1$ , and  $P_2$  were specified in the statement of work while  $P_3$  was added to facilitate the interpretation of the data. Sensors were added at locations  $P_a$  and  $P_b$  to provide primarily diagnostic information on pulser performance.

### 2. Pulser Geometries

To facilitate the interpretation of the test results, the geometry and dimensions of each of the test configurations used during these tests will be presented here.

#### a. Conic Test

Figure D-2 illustrates the geometry and dimensions in the vicinity of the pulser during the 125-ohm matched plate tests. All dimensions are given in feet. The matched plate conic consisted of two sections bolted together, a triangular section 8 feet long and a trapezoidal section 16 feet long.

#### b. Conducting Tube Tests

##### 1) Tubes Level With Bottom of Output Transition

Figure D-3 illustrates the geometry and dimensions of the test setup during the tests conducted with aluminum tubes replacing the peakers and installed level with the bottom of the output transition. The aluminum tubes were 2-1/2 inches in diameter and approximately 15 feet long. Connection to the switch and pulser unit was accomplished using the same short triangular conic section (8 feet long) as for the matched plate tests.

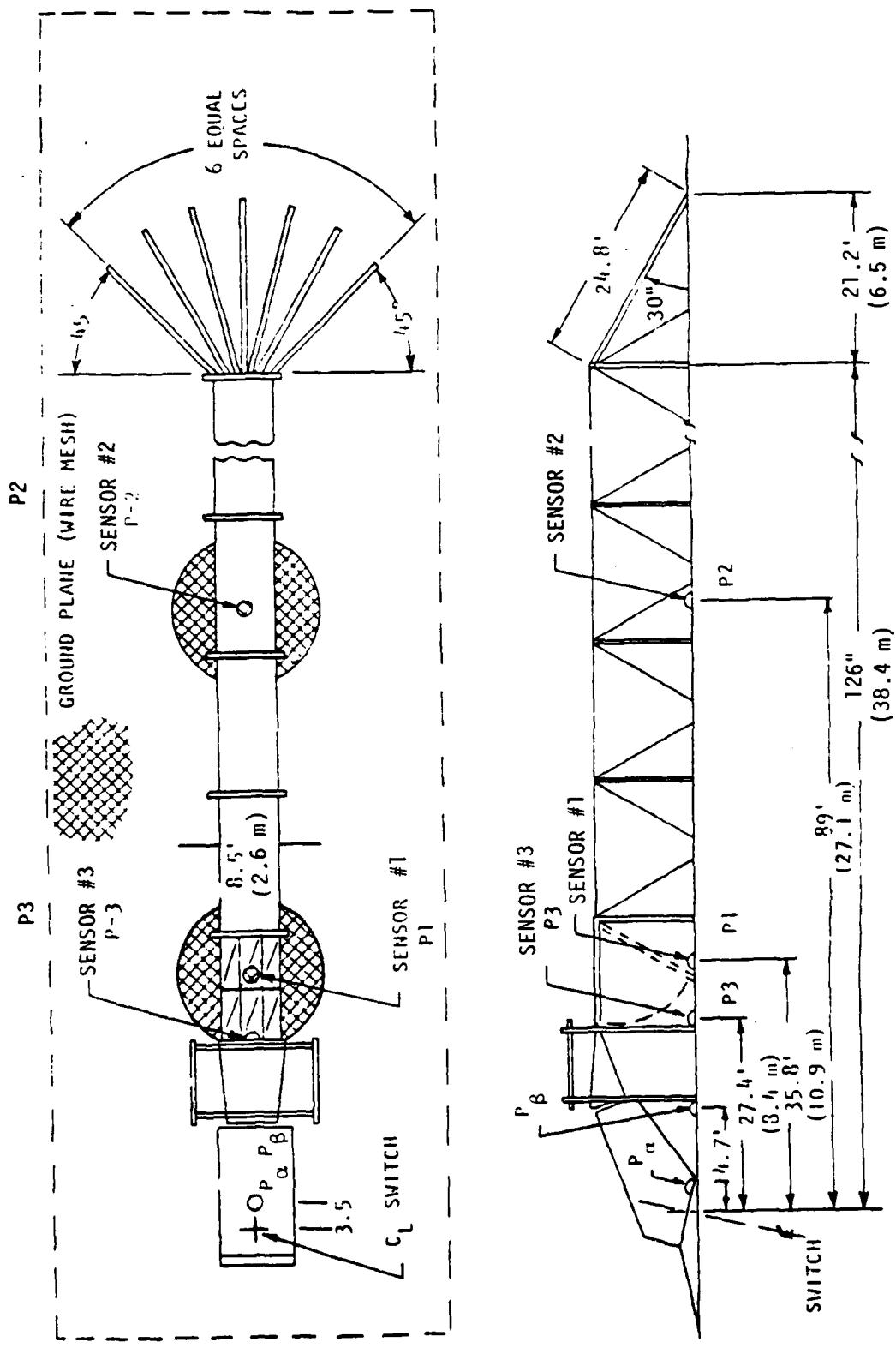


Figure D-1. Geometry and Dimensions of the PTF (December 1973 - January 1974) fanned termination.

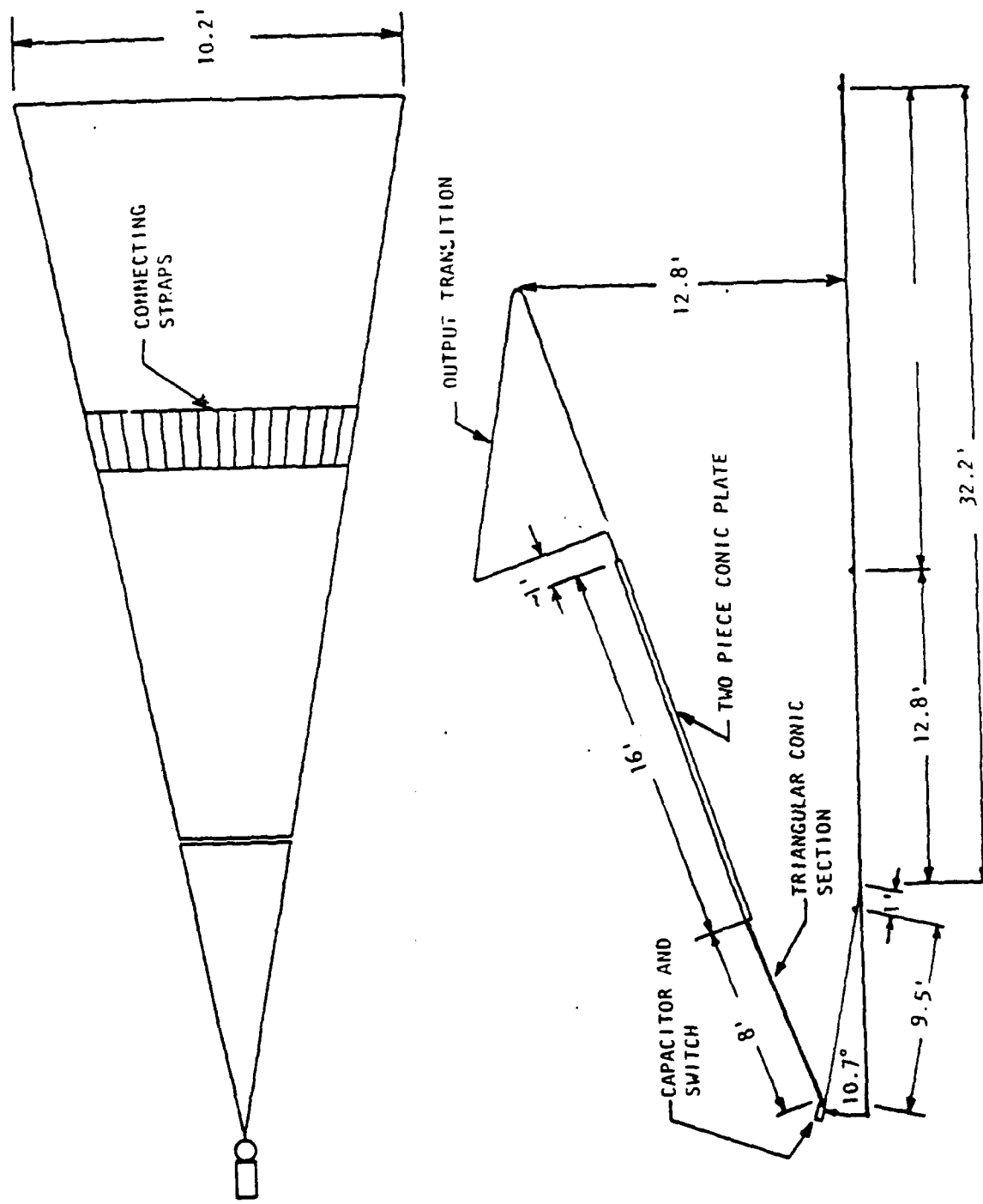


Figure D-2. 125-Ohm matched plate configuration.

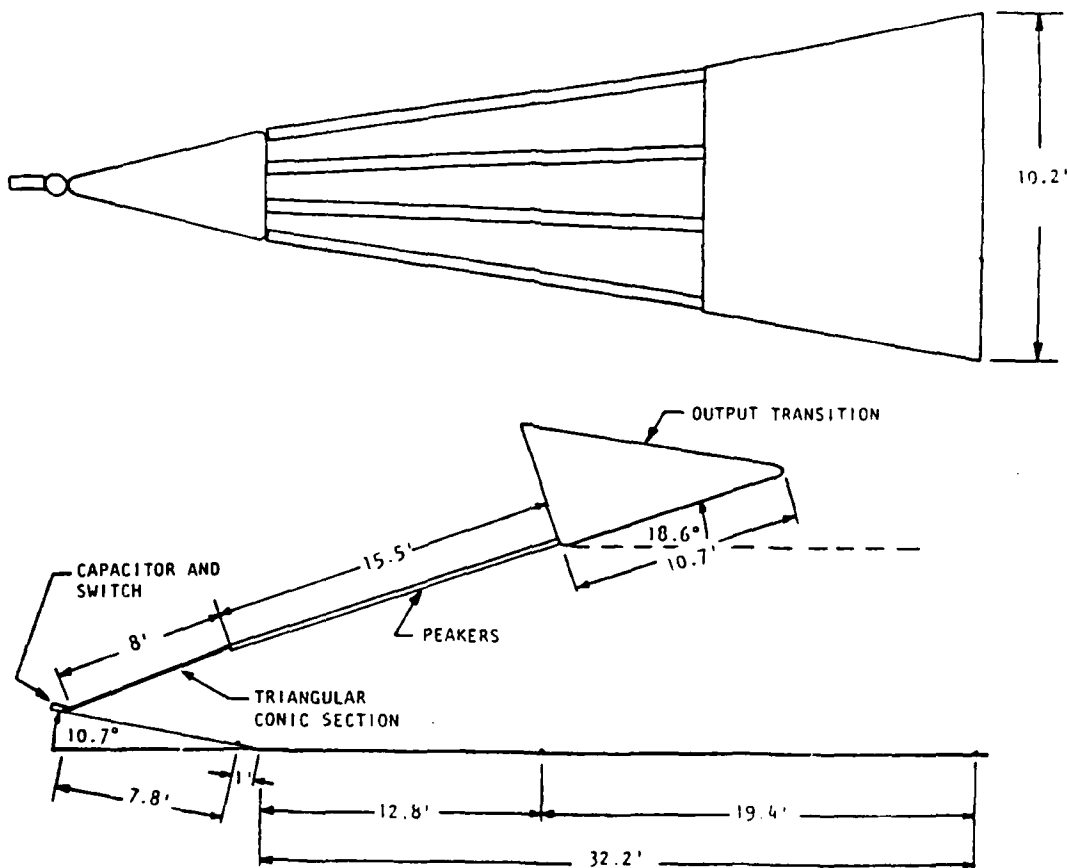


Figure D-3. Test configuration for peaker/conducting tube evaluation (aluminum tubes level with bottom of output transition).

2) Tubes 14 Inches Below Bottom of Output Transition

The geometry and dimensions of the test setup used during the tests performed with aluminum tubes mounted 14 inches below the bottom of the output transition are illustrated in Figure D-4. Wire braid straps connected the tubes to the back of the output transition.

c. Cone Tests

1) Bicone

Figure D-5 illustrates the geometry and dimensions of the test setup using the bicone switch. Connection between the bicone and peaker arms was accomplished with wire braid.

2) 88-Ohm Monocone - vertical

The geometry and dimensions of the test setup during the 88-ohm "vertical" monocone tests is depicted in Figure D-6. The monocone was connected to the peaker arms by wire braid. The cone half-angle for the 88-ohm monocone was approximately 21°.

3) 88-Ohm Monocone - Tilted

Figure D-7 illustrates the geometry and dimensions of the tilted 88-ohm monocone test configuration. The inclination of the cone axis with the local ground plane vertical was about 47°.

4) 125-Ohm Monocone - Vertical

The geometry and dimensions associated with the 125-ohm "vertical" monocone test configuration are illustrated in Figure D-8. The 125-ohm half-angle is about 15°.

5) 125-Ohm Monocone - Tilted

Figure D-9 illustrates the geometry and dimensions of the test configuration associated with the 125-ohm tilted monocone tests. The inclination of the cone axis from the local ground plane vertical was approximately 50°.

3. Switch Geometry

Figure D-10 illustrates the test configuration of the pulsing unit and switch typical of all the low voltage tests. The pulser consisted of a pair of charged capacitors which were discharged. The

AD-A111 506

MISSION RESEARCH CORP ALBUQUERQUE NM

F/G 9/5

ELECTROMAGNETIC CHARACTERIZATION OF A MARX PULSE GENERATOR.(U)

JUL 81 D V GIRI, F R GRAHAM

F29601-7R-C-0082

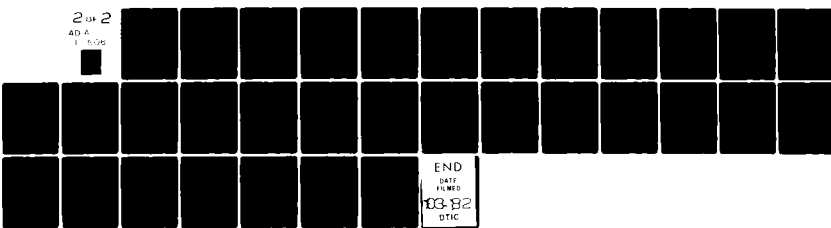
UNCLASSIFIED

AFWL-TR-81-31

NL

2 LM 2

AD A  
E 6-08



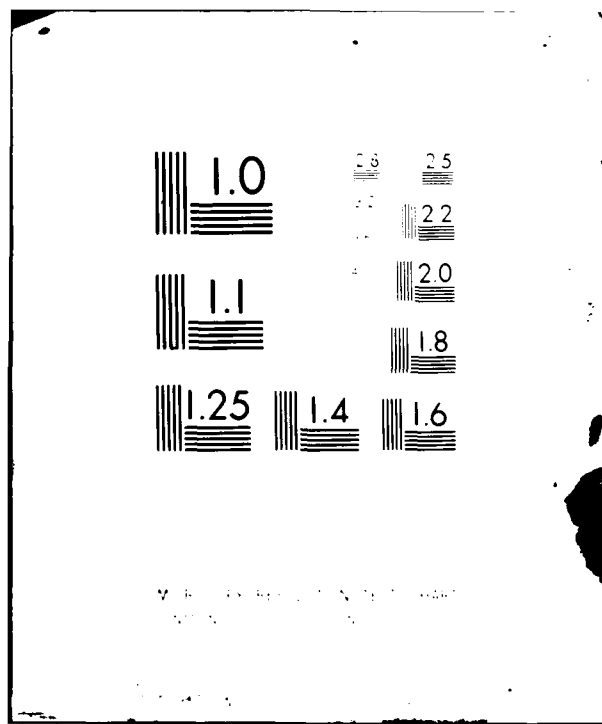
END

DATA

FILED

103-82

DTIC



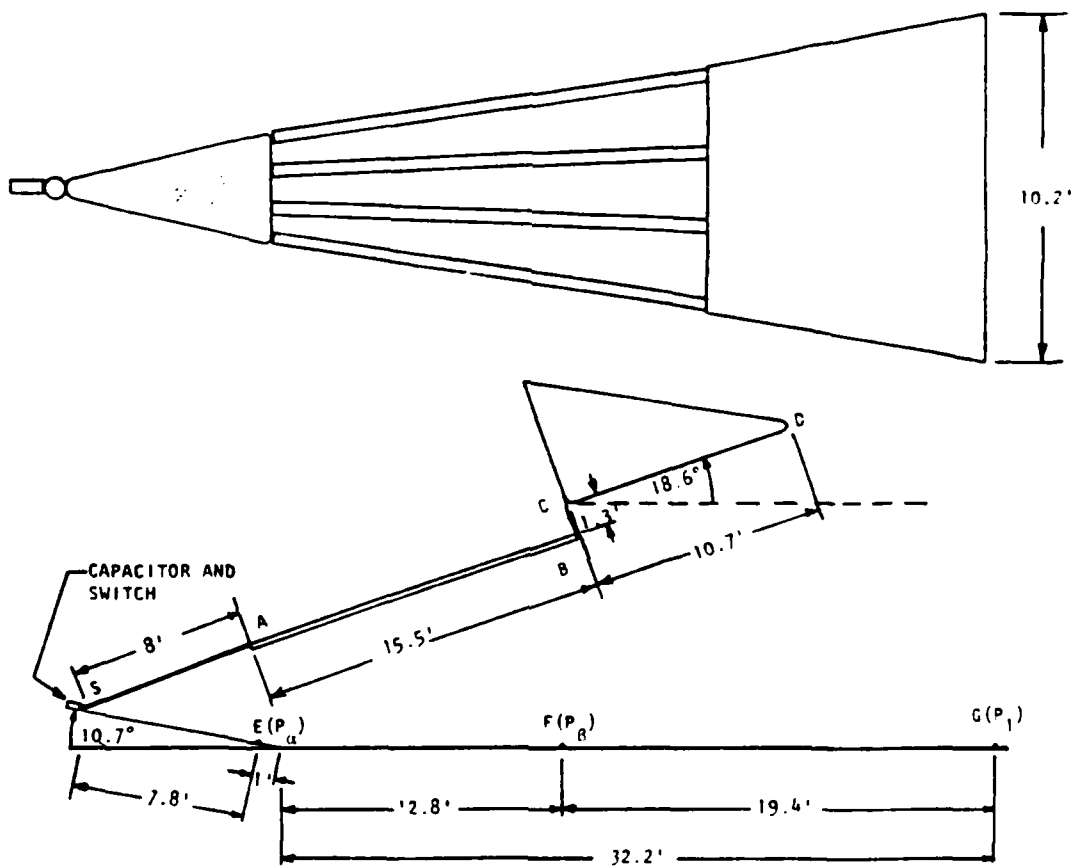


Figure D-4. Test configuration for peaker/conducting tube evaluation (aluminum tubes 14 inches below bottom of output transition).

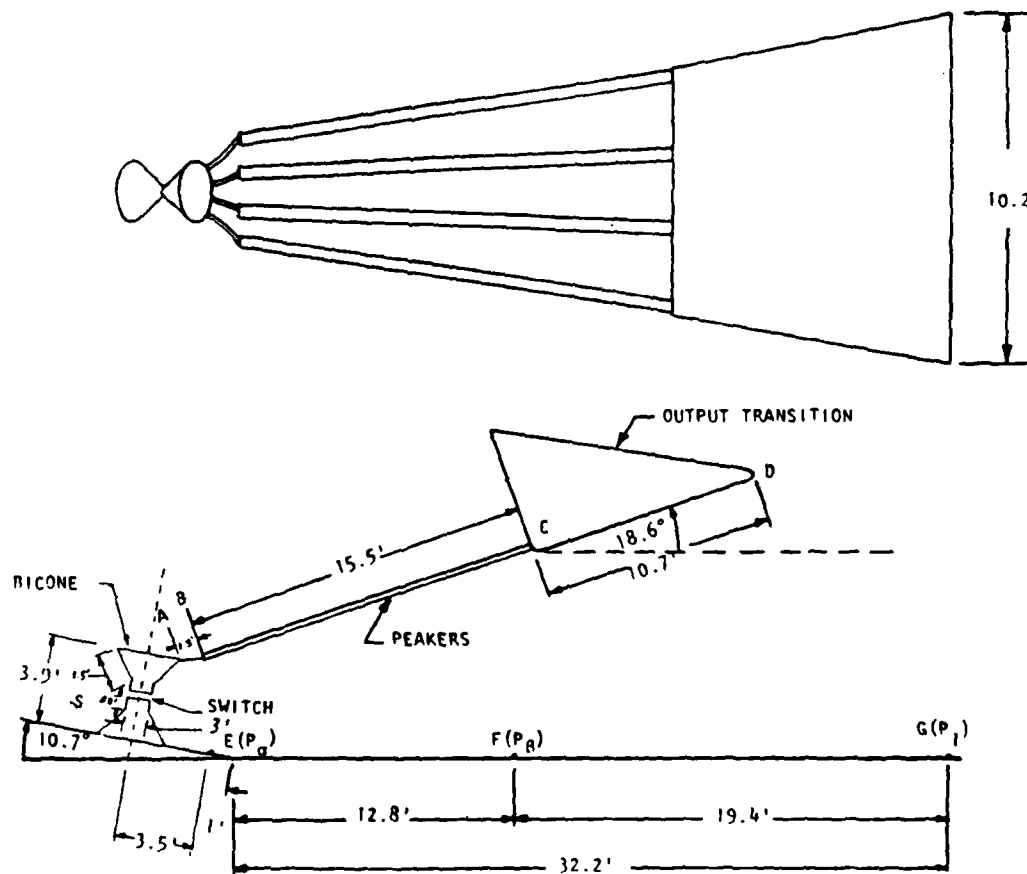


Figure D-5. Test configuration for bicone evaluation.

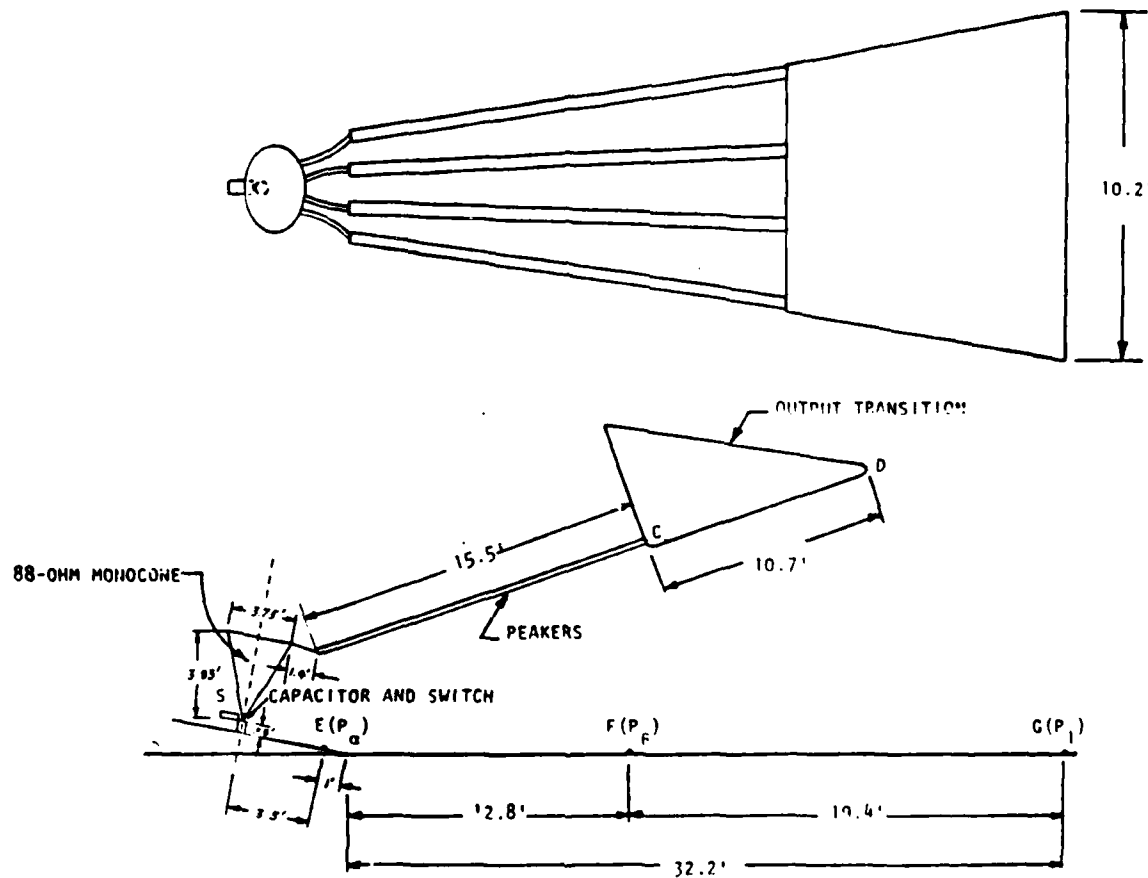


Figure D-6. Test configuration for 88-Ohm vertical monocone evaluation.

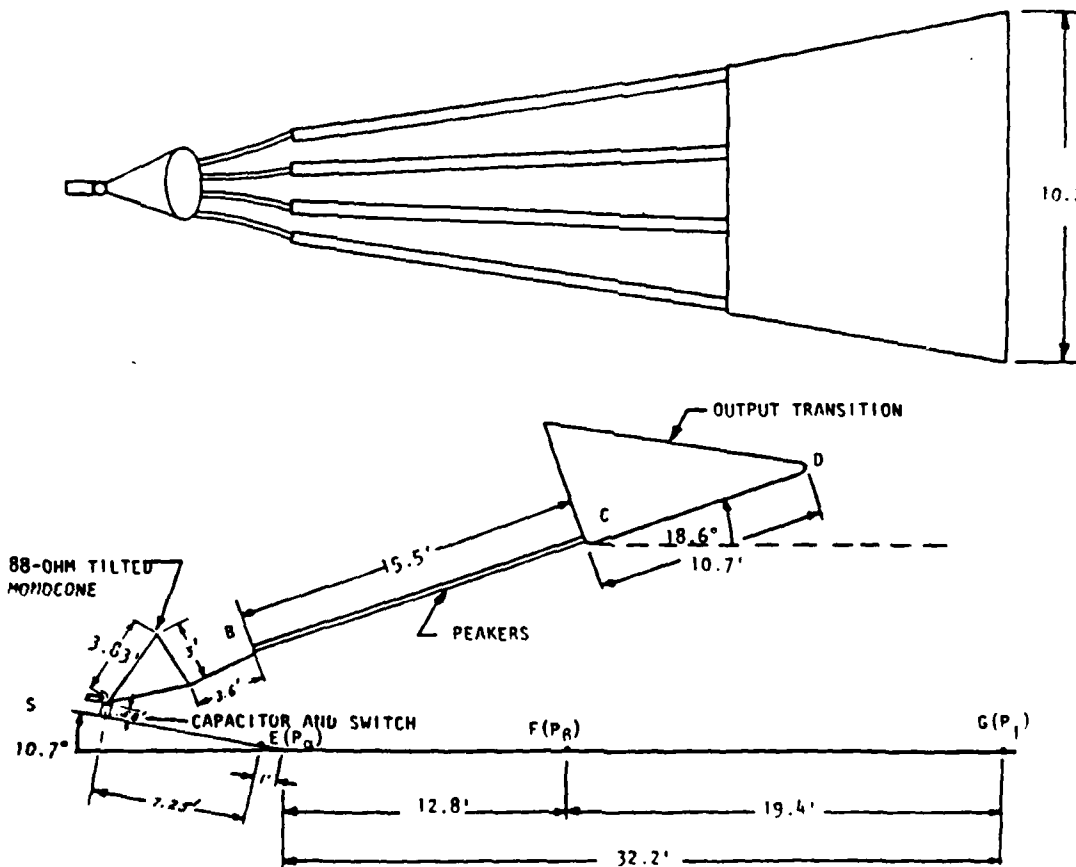


Figure D-7. Test configuration for 88-Ohm tilted monocone evaluation.

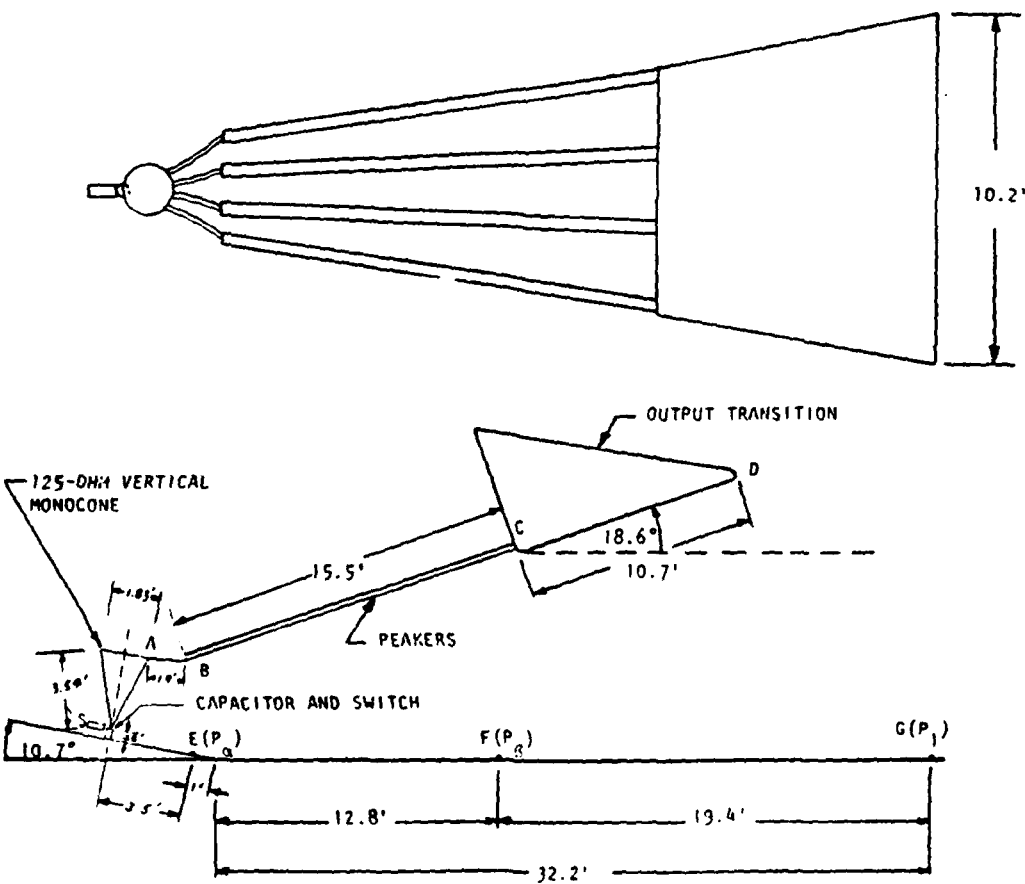


Figure D-8. Test configuration for 125-Ohm vertical monocone evaluation.

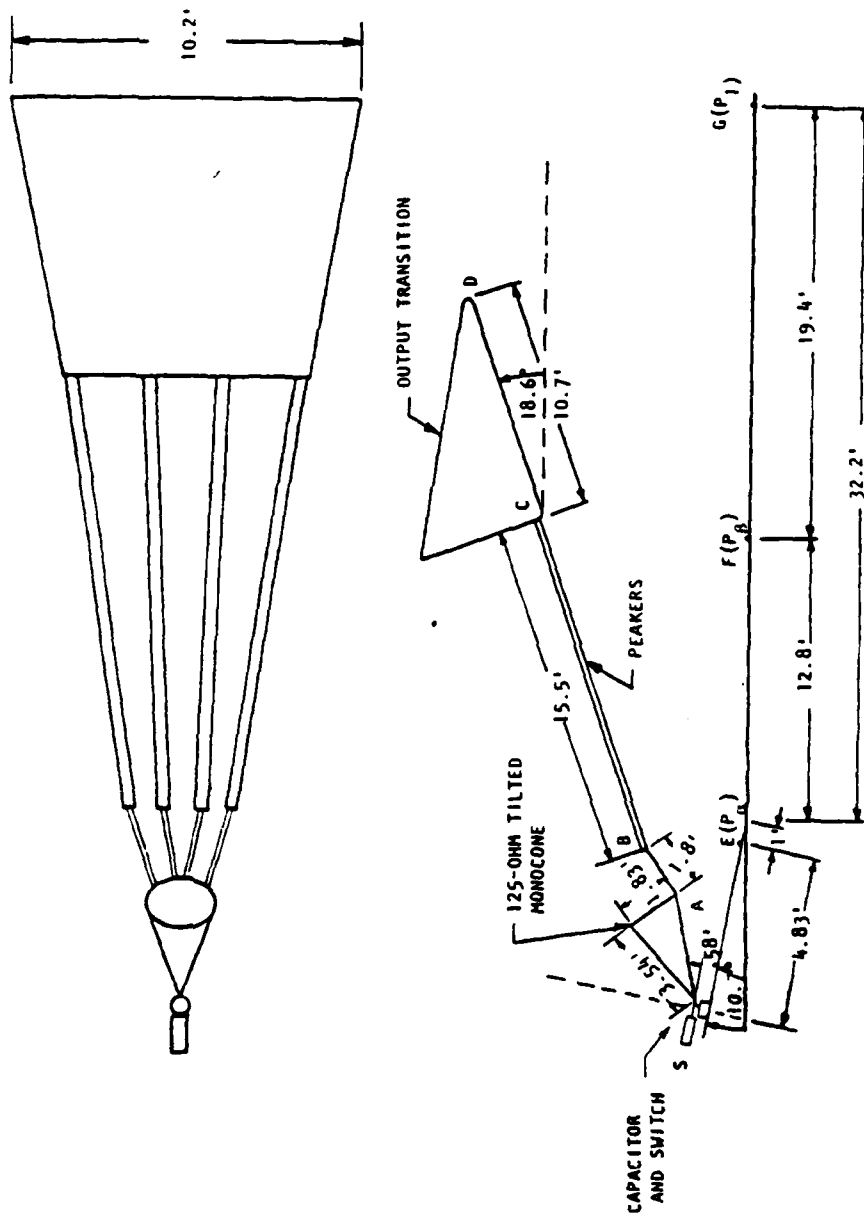


Figure D-9. Test configuration for 125-0hm tilted moncone evaluation.

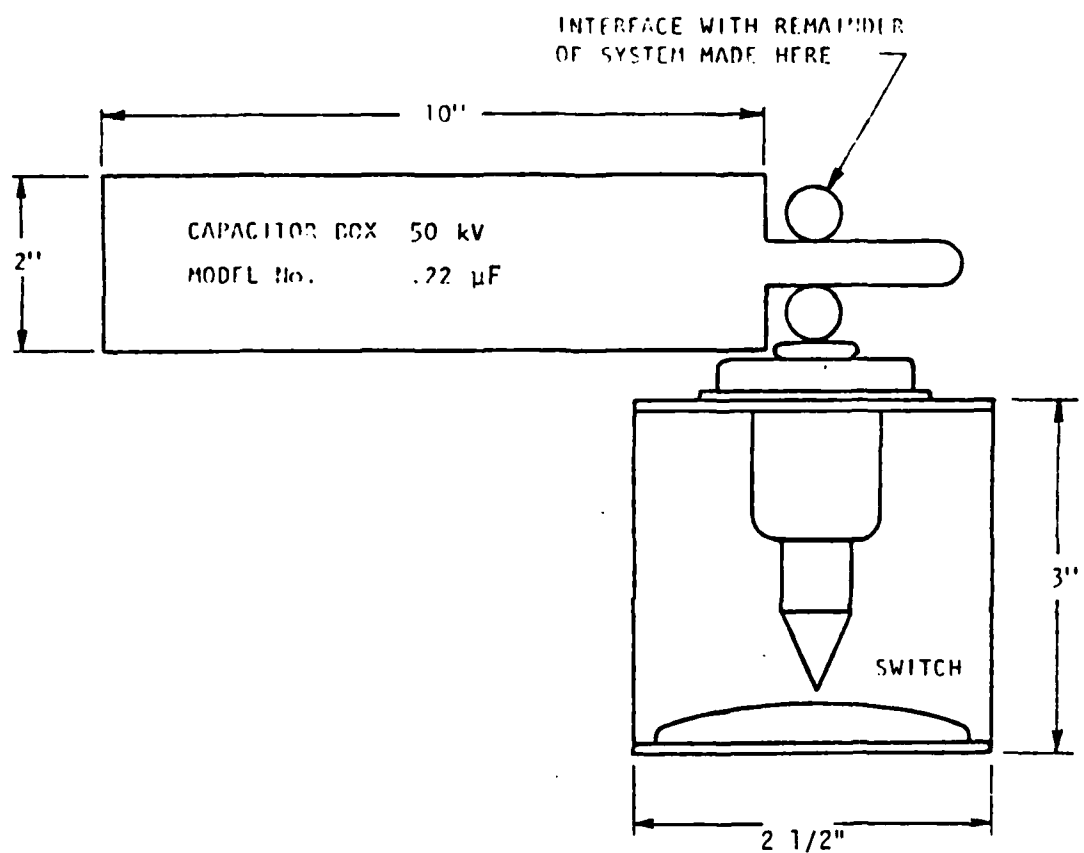


Figure D-10. Switch geometry.

charging voltage across the switch was approximately 42 kV for those tests. A summary of the electrical characteristics of the low voltage spring test configurations appears in Table D-1.

### C. INSTRUMENTATION

#### 1. Sensor Locations

Figure D-1 illustrates the geometry and dimensions of the PTF along with the locations of all sensors used during the low voltage spring tests. The locations of the sensors relative to the bend in the ground plane are summarized below.

<u>SENSOR DESIGNATION</u>	<u>DISTANCE FROM BEND IN GROUND PLANE (FEET)</u>
OUTPUT SWITCH	VARIABLE (NOMINALLY 4.5 FEET)
P <sub>a</sub>	1.0
P <sub>B</sub>	12.8
P <sub>1</sub>	32.2
P <sub>2</sub>	85

#### 2. System Schematic

Figure D-10 is a simplified schematic of the time domain data acquisition system at the PTF applicable to all the low voltage spring tests.

#### 3. Instrumentation System Performance

Instrumentation system performance can be summarized in terms of its sensitivity, accuracy, bandwidth, and risetime. The only significant performance criteria for this test series are the risetime degradation due to the instrumentation. The system sensitivity and accuracy is essentially the same as that described in Appendix B. System bandwidth is a corollary to system risetime which is described below.

TABLE D-2. SUMMARY OF ELECTRICAL CHARACTERISTICS

CHARACTERISTICS	VALUE
PEAKING CAPACITANCE	270 pF
NUMBER OF PEAKING CAPACITOR ASSEMBLIES	4
NUMBER OF SERIES CAPACITORS PER PEAKING CAPACITOR ASSEMBLY	9
PULSER OUTPUT VOLTAGE	~ 42 kV
RISETIME OF PULSER	~ 2 ns
CAPACITANCE OF PULSER	.22 $\mu$ F
SWITCH INDUCTANCE	.25 $\mu$ H

System risetime degradation calculations are described in Appendix B and its addendums\*. In the present case, degradation due to the oscilloscope, a Tektronic 485 with a 350 MHz bandwidth, and the sensors, either a MGL-4 or MGL-5 with upper frequency cutoffs of 230 MHz and 700 MHz respectively, provide negligible risetime degradation when considering inputs with risetimes greater than 3 nanoseconds. The remaining source is the approximately 300 feet of 7/8-inch Foamflex cable. Thus cable has about 1.5 dB attenuation at 100 MHz. The worst case risetime degradation is about 2 nanoseconds. More detail is given in the addendum to Appendix B.

#### D. TEST RESULTS

##### 1. Test Data

###### a. Introduction

Addendum 1 of this appendix presents the photo reproductions of all pertinent test data for the low voltage spring tests. No further pictorial presentation of this data will be provided here except as required in emphasis of particular points concerning the waveforms.

Addendum 2 summarizes, in table form, the waveform characteristics of the photo reproductions of the test data. These tables summarize the primary characteristics of the data such as peak voltage, risetime, e-fold time, and reflection and diffraction peaks. Figure 1 of Addendum 2 shows definitions used in those parameters. Also summarized is the identification and scale information concerning each piece of data presented.

Finally, Addendum 3 presents a summary of the times of transit, either transmission line or diffraction, for each of the configurations of this set of tests. Where it is felt applicable, both the transmission line transit times and the diffraction transit times are listed. The characters across the top horizontal row and down the first column represent locations of various interfaces of each configuration.

\*Addendums 1, 2 and 3 are not included in this report. Refer to Maxwell Laboratory Report No. MLR-483, Nov 1975.

The tables are read by choosing an origin from the set of characters in the first column and then moving along the row to which this character belongs until the appropriate terminal block is reached. This block gives the one-way transit time (transmission line or diffraction) from the origin character to the terminal character. The character representation of each configuration is keyed to the sketch of the configuration appearing at the bottom of each summary table as well as on the detailed configuration figures presented earlier.

b. Summary of Reflection/Diffraction Results

Tables D-1 through D-9 are provided to combine the results of Addendums 1, 2, and 3 concerning the specific waveform characteristics of reflection and diffraction peaks. The first column of each table lists the location at which the results apply, while the next two columns indicate the measured time delays between the initial incidence of the pulse at the sensor and the time of the arrival of the first contributions from a reflection or diffraction in the configuration under study. The fourth column lists the calculated arrival times from the most probable sources of reflection or diffraction as derived from the delay times presented in Addendum 3. Finally the last column gives a possible interpretation in general terms concerning reflection or diffraction at various interfaces within the configuration.

c. Evaluation of Interface Problem Areas

1) 125-Ohm Matched Plate (Reference Figure D-2)

Table D-2 summarizes the information necessary for evaluating the quality of interfaces in the 125-ohm matched plate geometry. Due to the nature of this configuration, it is particularly well suited for interpreting the effects of the output transition on the pulse waveform characteristics.

As one should expect from a geometry such as that associated with the matched plate, the only major diffraction or reflection peaks on the transmitted waveforms occur in the region where both impedance

TABLE D-2. WAVEFORM INTERPRETATION OF 125 OHM MATCHED PLATE

SENSOR LOCATION	MEASURED 1ST TIME OSCILLATION	CALCULATED NEAREST TRANSIT TIME S	INTERPRETATION
P <sub>11</sub>	31.5 or 31.5	32.6	DIFFRACTION FROM BACK OF OUTPUT TRANSITION
	50.5 or 50.5	30.6	DIFFRACTION FROM INTERFACE OF MATCHED PLATE WITH STRAPS CONNECTING TO OUTPUT TRANSITION
		51.0	REFLECTION BETWEEN BACK OF OUTPUT TRANSITION AND OUTPUT SWITCH
		50.6	REFLECTION FROM FRONT OF OUTPUT TRANSITION
SWITCH	48	48	MULTIPLE REFLECTION BETWEEN LOWER END OF MATCHED PLATED AND CONNECTING STRAPS TO OUTPUT TRANSITION
		5.5	- UNPREDICTABLE
P <sub>B</sub>	9.0	11.0	Possible DIFFRACTION FROM INTERFACE AT TOP END OF OUTPUT TRANSITION WITH TRANSMISSION LINE. UNPREDICTABLE
	7.4 46	7.4 50.2	MULTIPLE REFLECTION BETWEEN TOP END OF MATCHED PLATE AND OUTPUT SWITCH.
P <sub>1</sub>	8.4	8.3	DIFFRACTION FROM FRONT END OF OUTPUT TRANSITION UNPREDICTABLE
	5.5	-	
	25.0	24.8	REFLECTION BETWEEN FRONT OF OUTPUT TRANSITION AND TOP END OF MATCHED PLATE
P <sub>2</sub>	47.3 49 or 49	48	MULTIPLE REFLECTION BETWEEN TOP END OF MATCHED PLATE AND OUTPUT SWITCH
		11.8	POSSIBLE REFLECTION FROM TOP CORNER OF OUTPUT TRANSITION. REFLECTION BETWEEN TOP END OF MATCHED PLATE AND OUTPUT SWITCH
		48	REFLECTION BETWEEN BACK OF OUTPUT TRANSITION AND OUTPUT SWITCH
		50.2	REFLECTION BETWEEN BACK OF OUTPUT TRANSITION AND OUTPUT MATCH.

TABLE D-3. WAVEFORM INTERPRETATION OF 2-1/2-INCH ALUMINUM TUBES - LEVEL WITH BOTTOM OF OUTPUT TRANSITION

SENSOR LOCATION	MEASURED (ns)		CALCULATED NEAREST TRANSIT TIMES	INTERPRETATION
	1ST TIME OSCILLATION	REPETITIVE OSCILLATION		
$P_a$	7.5 31	6.5 46	- 31 47	UNPREDICTABLE REFLECTION FROM BACK OF OUTPUT TRANSITION MULTIPLE REFLECTION BETWEEN BACK OF OUTPUT TRANSITION AND OUTPUT SWITCH
			- 47	UNPREDICTABLE MULTIPLE REFLECTION BETWEEN BACK OF OUTPUT TRANSITION AND OUTPUT SWITCH.
$P_b$		7.8 46	- 47	UNPREDICTABLE MULTIPLE REFLECTION BETWEEN BACK OF OUTPUT TRANSITION AND OUTPUT SWITCH.
	47			
$P_1$	8.6 8.6	7.8 45	- 8.8 47	UNPREDICTABLE DIFFRACTION FROM FRONT END OF OUTPUT ELECTRODE MULTIPLE REFLECTION BETWEEN BACK OF OUTPUT TRANSITION AND OUTPUT SWITCH
	46			
$P_2$	48		47	MULTIPLE REFLECTION BETWEEN BACK OF OUTPUT TRANSITION AND OUTPUT SWITCH

TABLE D-4. WAVEFORM INTERPRETATION OF 2-1/2-INCH ALUMINUM TUBE  
14-INCH BELOW BOTTOM OF OUTPUT TRANSITION

SENSOR LOCATION	MEASURED REPETITIVE OSCILLATION		CALCULATED NEAREST TRANSIT TIMES	INTERPRETATION
	1ST TIME OSCILLATION	TIME		
$P_A$	8.8	-	-	UNPREDICTABLE
	31.0	31	REFLECTION FROM BACK OF OUTPUT TRANSITION	
$P_B$	47	47	MULTIPLE REFLECTION BETWEEN BACK OF OUTPUT TRANSITION AND OUTPUT SWITCH	
	7.9	-	UNPREDICTABLE	
$P_1$	45	47	MULTIPLE REFLECTION BETWEEN BACK OF OUTPUT TRANSITION AND OUTPUT SWITCH	
	8.0	8.8	DIFFRACTION FROM FRONT END OF OUTPUT TRANSITION	
$P_2$	46	-	UNPREDICTABLE	
	48	47	MULTIPLE REFLECTION BETWEEN BACK OF OUTPUT TRANSITION AND OUTPUT SWITCH	
	9.5	-	UNPREDICTABLE	
	46	47	MULTIPLE REFLECTION BETWEEN BACK OF OUTPUT TRANSITION AND OUTPUT SWITCH	
	55	55	REFLECTION BETWEEN FRONT OF OUTPUT TRANSITION AND TUBE CONNECTION TO CONIC PLATE	

TABLE D-5. WAVEFORM INTERPRETATION OF BICONIC (VERTICAL)

SENSOR LOCATION	MEASURED		CALCULATED NEAREST TRANSIT TIMES	INTERPRETATION
	1ST TIME OSCILLATION	REPETITIVE OSCILLATION		
$P_a$	6.8		6.8	REFLECTION BETWEEN LOWER END OF PEAKERS AND OUTPUT SWITCH
		8.5 42	-- 39.6	UNPREDICTABLE REFLECTION FROM UPPER END OF PEAKERS TO OUTPUT SWITCH
$P_b$	6.5		6.8	REFLECTION BETWEEN LOWER END OF PEAKERS AND OUTPUT SWITCH
		8.2 43	-- 38.6	UNPREDICTABLE MULTIPLE REFLECTION BETWEEN UPPER END OF PACKERS AND OUTPUT SWITCH
$P_1$	6.8		6.8	REFLECTION BETWEEN LOWER END OF PEAKERS AND OUTPUT SWITCH
		8.5 38	-- 39.6	UNPREDICTABLE REFLECTION BETWEEN UPPER END OF PEAKERS AND OUTPUT SWITCH
$P_2$	42	42	39.6	MULTIPLE REFLECTION BETWEEN UPPER END OF PEAKERS AND OUTPUT SWITCH

TABLE D-6. WAVEFORM INTERPRETATION OF 88-OHM MONOCONE (VERTICAL)

SENSOR LOCATION	MEASURED		CALCULATED NEAREST TRANSIT TIMES	INTERPRETATION
	1ST TIME OSCILLATION	REPETITIVE OSCILLATION		
SWITCH	8.6		8.8	REFLECTION FROM INTERFACE OF MONOCONE AND CONNECTING STRAP.
	11.8		11.6	REFLECTION FROM INTERFACE OF CONNECTING STRAP WITH LOWER END OF PEAKERS
	43	42.5	42.6	REFLECTION FROM INTERFACE OF PEAKING CAPACITOR AND OUTPUT TRANSITION
P <sub>a</sub>	5.6		5.6	DIFFRACTION FROM INTERFACE OF MONOCONE AND CONNECTING STRAP
		4.6	-	UNPREDICTABLE
	34.0 or 34.0		31.0	REFLECTION FROM INTERFACE OF PEAKERS WITH OUTPUT TRANSITION
		42	33.6	DIFFRACTION FROM INTERFACE OF PEAKERS WITH OUTPUT TRANSITION
			42.6	MULTIPLE REFLECTION BETWEEN UPPER END OF PEAKERS AND OUTPUT SWITCH
P <sub>b</sub>	7.6		7.6	POSSIBLE REFLECTION BETWEEN MONOCONE APEX AND END OF MONOCONE
	42	42	42.6	MULTIPLE REFLECTION BETWEEN UPPER END OF PEAKERS AND OUTPUT SWITCH
P <sub>1</sub>	9.3		9.4	DIFFRACTION FROM FRONT END OF OUTPUT TRANSITION
	32.4		31.0	REFLECTION BETWEEN UPPER AND LOWER ENDS OF PEAKERS
	or 32.4		32.8	REFLECTION BETWEEN UPPER END OF PEAKERS AND INTERFACE WITH TOP OF MONOCONE
		43	42.6	MULTIPLE REFLECTION BETWEEN UPPER END OF PEAKERS AND OUTPUT SWITCH
P <sub>2</sub>	43	44	42.6	REFLECTION BETWEEN UPPER END OF PEAKERS AND OUTPUT SWITCH

TABLE D-7. WAVEFORM INTERPRETATION OF 88-OHM MONOCONE (TILTED)

SENSOR LOCATION	MEASURED		CALCULATED NEAREST TRANSIT TIMES	INTERPRETATION
	1ST TIME OSCILLATION	REPETITIVE OSCILLATION		
SWITCH	8 47	47	8.8 47	REFLECTION FROM END OF MONOCONE MULTIPLE REFLECTIONS BETWEEN UPPER END OF PEAKERS AND OUTPUT SWITCH
P <sub>a</sub>	6.8 31.5 52		7.2 31.0 52.4	REFLECTION BETWEEN ENDS OF CONNECTING STRAP FOR MONOCONE/PEAKERS REFLECTION BETWEEN ENDS OF PEAKERS
P <sub>b</sub>	7.6 46.5	47	7.6 47	REFLECTION BETWEEN APEX OF MONOCONE AND END OF MONOCONE MULTIPLE REFLECTIONS BETWEEN UPPER END OF PEAKERS AND OUTPUT SWITCH
P <sub>1</sub>	8 47.5	46	7.9 47	DIFFRACTION FROM FRONT END OF OUTPUT TRANSITION MULTIPLE REFLECTIONS BETWEEN UPPER END OF PEAKERS AND OUTPUT SWITCH
P <sub>2</sub>	48		47	REFLECTION BETWEEN UPPER END OF PEAKERS AND OUTPUT SWITCH

TABLE D-8. WAVEFORM INTERPRETATION OF 125-OHM MONOCONE (VERTICAL)

SENSOR LOCATION	MEASURED		CALCULATED NEAREST TRANSIT TIMES	INTERPRETATION
	1ST TIME OSCILLATION	REPETITIVE OSCILLATION		
$P_a$	6		5.5	DIFFRACTION FROM CONE/CONNECTING STRAP INTERFACE
	38	42	43	MULTIPLE REFLECTION BETWEEN UPPER END OF PEAKERS AND OUTPUT SWITCH
$P_b$		8.5	--	UNPREDICTABLE
	46	44	43	MULTIPLE REFLECTIONS BETWEEN UPPER END OF PEAKERS AND OUTPUT SWITCH
$P_1$	9.9		9.2	DIFFRACTION FROM FRONT END OF OUTPUT TRANSITION
	46.5	46	43	MULTIPLE REFLECTIONS BETWEEN UPPER END OF PEAKERS AND OUTPUT SWITCH
$P_2$	43	43	43	MULTIPLE REFLECTIONS BETWEEN UPPER END OF PEAKERS AND OUTPUT SWITCH

TABLE D-9. WAVEFORM INTERPRETATION OF 125-OHM MONOCONE (TILTED)

SENSOR LOCATION	MEASURED		CALCULATED NEAREST TRANSIT TIMES	INTERPRETATION
	1ST TIME OSCILLATION	REPETITIVE OSCILLATION		
$P_1$	6	4.9	--	UNPREDICTABLE
	34		34.6	REFLECTION BETWEEN UPPER END OF PEAKERS AND END OF MONOCONE
		43	42.8	MULTIPLE REFLECTIONS BETWEEN UPPER END OF PEAKERS AND OUTPUT SWITCH
$P_B$	8.2		8.2	REFLECTION BETWEEN END OF MONOCONE AND OUTPUT SWITCH
		7.5	--	UNPREDICTABLE
	34		34.6	REFLECTION BETWEEN UPPER END OF PEAKERS AND END OF MONOCONE
$P_1$		43	42.8	MULTIPLE REFLECTIONS BETWEEN UPPER END OF PEAKERS AND OUTPUT SWITCH
	8.3	8.2	8.2	REFLECTIONS BETWEEN END OF MONOCONE AND OUTPUT SWITCH
	or		7.6	DIFFRACTION FROM FRONT END OF OUTPUT TRANSITION
$P_2$	43	43	42.8	MULTIPLE REFLECTION BETWEEN UPPER END OF PEAKERS AND OUTPUT SWITCH
	63	43	42.8	MULTIPLE REFLECTIONS BETWEEN UPPER END OF PEAKERS AND OUTPUT SWITCH

and/or geometric discontinuities are present, the output transition. Clearly from Table D-2, it is evident that the primary impedance discontinuities are at the back of the output transition and at the straps connecting the transition to the matched plate. It also appears that diffraction from the geometric discontinuity at the bend between the output transition and transmission line produces an early time diffraction peak on the waveform. Reflections from impedance discontinuities are apparently also detectable from the interface between the output transition and transmission line.

An estimate of the magnitude of the major impedance discontinuity at the end of the matched plate can be obtained from measurements of the amplitude of the reflected component and a simple calculation. Perhaps the most unequivacable data from which this estimate can be made are from the current monitor directly under the switch. Figure D-11 is the digitization of the 20 ns/div curve from the set of data at the switch during the matched plate tests. The period of the major oscillation seen on this curve corresponds to the two-way transit time from the output switch to the output transition region. From the figure, the relative amplitudes of the incident and reflected peaks are 1.45 and 4.55 divisions, respectively. The reflection coefficient ( $\rho$ ) is the ratio of the reflected to incident amplitudes hence

$$\rho \approx .319$$

The current reflection coefficient is also given by

$$\rho_L = \frac{Z_o - Z_L}{Z_L + Z_o}$$

where  $Z_L$  is the effective load impedance provided by the output transition interface and  $Z_o$  is the characteristic impedance of the matched plate (125 ohms). Therefore, the effective impedance of the output transition region is given by

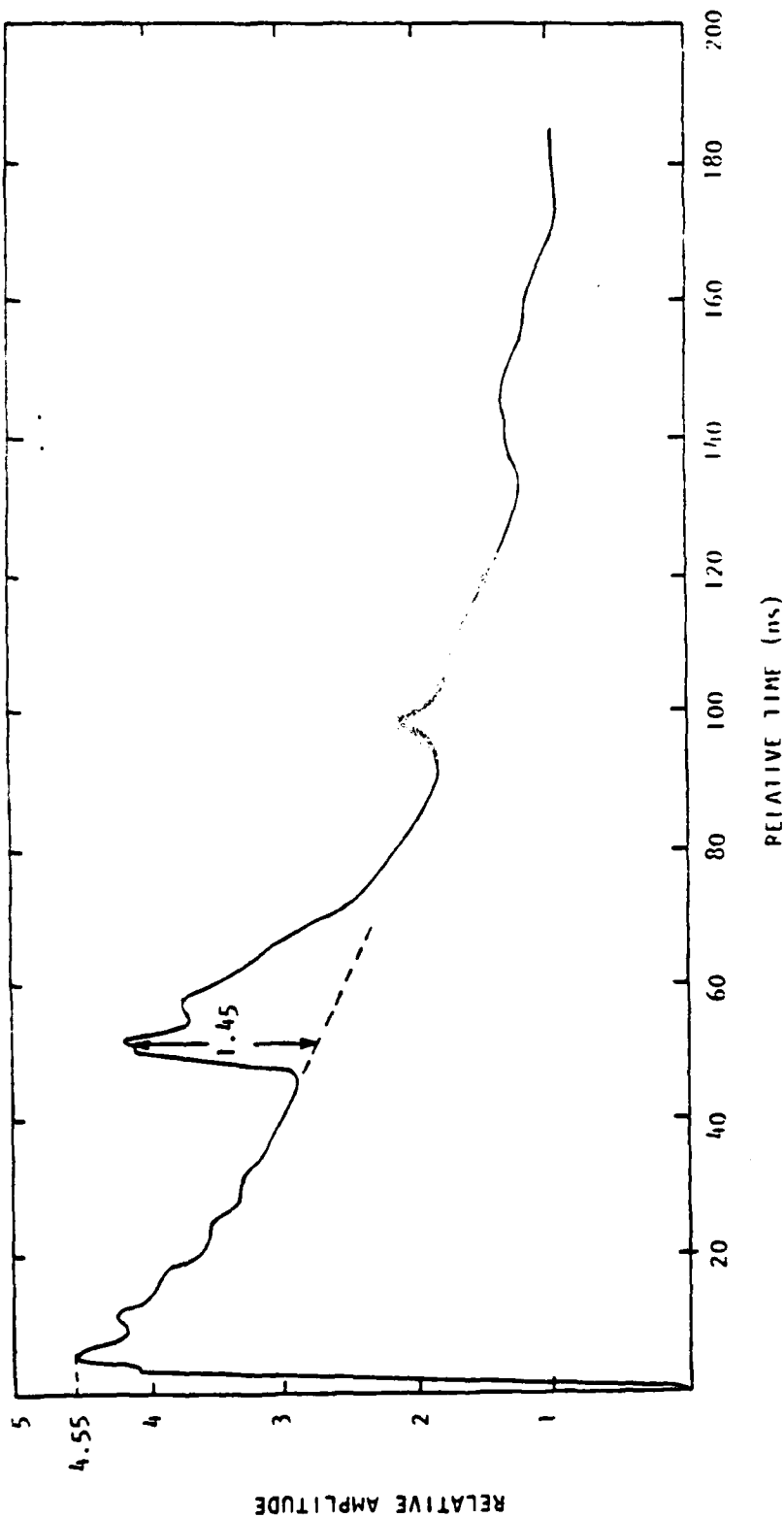


Figure D-11. Digitized matched plate data (Shot 46, 3/26/74).

$$Z_L = Z_0 \left( \frac{1-\rho}{1+\rho} \right)$$

$$Z_L = 64.5 \text{ ohms}$$

The foregoing analysis of the impedance discontinuity at the matched plate/output transition interface is, of course, a grossly over-simplified one. In reality, the actual impedance of the output transition at its interface with the matched plate is probably more nearly 100 to 110 ohms. An alternate explanation of this mismatch might consider the time required for the wave or current sheet to completely traverse the surface of the output transition section. This time can be roughly equated to the charging time of a capacitor. Such an equivalent representation would predict an initially low impedance and qualitatively explain the observed data.

This mismatch phenomena will be present in the Horizontal TRESTLE although in reduced magnitude. The top of the output transition for the production pulsers has been truncated to provide a shorter transit time and a higher quasi-static impedance. It should be noted that effects of this discontinuity are not apparent at the locations,  $P_1$  and  $P_2$ . Thus this large discontinuity produces field perturbations that are apparently overcome by other mechanisms so that its influence is minor outside the confines of the pulser.

2) Two and One-Half Inch Aluminum Tubes (Reference Figures D-3 and D-4)

Both sets of data on the aluminum tubes installed in place of the peakers (tubes level with bottom of output transition and 14 inches below bottom of output transition) show the same reflection and diffraction peaks as might be expected. Tables D-3 and D-4 summarize these results indicating that the primary source of reflections is the impedance discontinuity between the tubes and the output transition. It is also evident that at sensor location  $P_1$  in front of the output transition, diffraction from the geometric discontinuity at the upper end of

the output transition leads to early time degradation to the pulse waveform. There is no apparent difference in the measured waveform using either of these configurations.

3) Cone Tests

a) Bicone

Table 0-5 summarizes the reflection/diffraction peaks and oscillations observed in the output waveforms associated with the bicone configuration. The primary peaks correspond to reflections between both ends of the peakers and the output switch. Due to the complexity of this particular geometry, it is not clear whether or not any diffraction effects are present.

b) 88-0hm Monocone - Vertical

Table 0-6 summarizes the reflection and diffraction peaks evident on the waveforms obtained in the 88-ohm vertical monocone configuration. Clear evidence is given in the table that reflections due to impedance discontinuities occur at every interface in the configuration except that of the output transition to the transmission line. A large reflection (~60 percent of incident) appears to be occurring at the interface between the monocone and straps connecting to the peakers. Another smaller reflection occurs at the interface of the monocone/peaker connecting strap and the lower end of the peakers. Finally, there is a reflection apparently coming from the interface of the peakers with the back of the output transition.

In addition to the reflection peaks there are apparent diffraction peaks resulting from diffraction from three different interfaces. First there is diffraction from the monocone/connecting strap interface which appears to be quite a large contribution (about 70 percent of incident peak). Next there is possible diffraction from the peaker/output transition interface and finally there is diffraction from the interface of the output transition with the transmission line. Both the first and last diffraction effects are early time contributions to waveform degradation.

c) 88-Ohm Monocone - Tilted

Table D-7 summarizes the reflection/diffraction contributions to the output waveform for the 88-ohm tilted monocone. Among the major reflection peaks which are apparent are a reflection from the monocone/connecting strap interface; one from the interface between the upper end of the peakers and the output transition and, apparently, reflections between the ends of the peakers; and one from the tip of the output transition to the lower end of the peakers. In addition, there appears to be diffraction from the connection of the output transition to the transmission line as measured at sensor location P<sub>1</sub>.

d) 125-Ohm Monocone - Vertical

Table D-8 summarizes the reflection/diffraction contributions to the output waveform for the 125-ohm vertical monocone. The only major reflection peaks for this configuration correspond to reflection from the interface between the upper end of the peakers and the output transition. And again for sensor location P<sub>1</sub>, there is an apparent early time diffraction peak originating from the tip of the output transition.

e) 125-Ohm Monocone - Tilted

A summary of the reflection/diffraction peaks for the 125-ohm tilted monocone appears in Table D-9. The major categories of reflections which appear in this table are: one corresponding to a reflection between the upper end of the peakers and the top of the monocone, reflection from the top of the monocone to the output switch, and a reflection between the upper end of the peakers and the output switch. In addition, there is an apparent diffraction peak corresponding to diffraction from the tip of the output transition.

d. Summary of Interface Problem Areas

A summary of all interface problem areas is presented in Table D-10. The major interfaces associated with the various configurations of the low voltage spring tests are listed across the top of the table.

TABLE D-10. SUMMARY OF INTERFACE PROBLEM AREAS

CONFIGURATION	V	T	CON/CONNECTING STRAPS			CONNECTING STRAPS/OUTPUT			PEAKS/OUTUT TRANSITION			OUT/IT TRANSITION/LINE		
			REF	DIFF	MAG	REF	DIFF	MAG	REF	DIFF	MAG	REF	DIFF	MAG
125 OHM MATCHED PLATE	S					R		M						
	P <sub>2</sub>						P	C	S			S		
	P <sub>3</sub>				R	M								
	P <sub>1</sub>				R	S						P	C	L
	P <sub>4</sub>				R	S	A							
125 OHM TWO-SEG. REFL.	F								R		S			
	F <sub>2</sub>										Z			
	F <sub>3</sub>								R	S	Z			
	P <sub>1</sub>								R	S	Z			
	P <sub>2</sub>								R	S				
ALUMINUM USES IN DOOR	P <sub>1</sub>								R	S				
	P <sub>2</sub>								R	S				
	P <sub>3</sub>								R	S	C	P		
	P <sub>4</sub>		R	S					R	S	R	C		
	F <sub>3</sub>		D	M					R	M				
88 OHM MONOCONE	P <sub>2</sub>		R	M					R	M				
	P <sub>3</sub>		R	M					R	M				
	P <sub>4</sub>		R	M					R	M	C	L		
	S <sub>1</sub>	R	S						R	M				
	P <sub>3</sub>	R	M	R	M				R	M				
125 OHM MONOCONE	P <sub>4</sub>	R	L						G	S				
	P <sub>1</sub>								R	M				
	P <sub>2</sub>								R	M				
	P <sub>3</sub>		D	L					R	M				
	P <sub>4</sub>								R	M				

The configurations are listed in the first column followed by designations of the sensor locations either in the second or third column according to the orientation of the switch (vertical - V, or tilted - T). The remainder of the table lists the major reflection and/or diffraction originating interfaces (R and D, respectively) along with an estimate of the relative magnitude of the effect of each reflection and/or diffraction on the output pulse waveform. The relative magnitudes are categorized into three classes; large effects (L) of greater than 50 percent of incident peak amplitude, medium effects (M) of less than 50 but more than 20 percent of incident peak amplitude, and small effects (S) of 20 percent of incident peak amplitude or less.

The table presents an overview of all the low voltage spring tests together and clearly points out that the major interface contributing to reflection effects is the interface at the back of the output transition. Similarly, it is evident that the interface contributing most severely to diffraction effects is the interface of the output transition with the transmission line.

For the cases where some kind of switch cone is present (bicone or monocone), the table also indicates that, in general, the interface between the top of the cones and the connecting straps to the peakers appears to be the origin of reflection problems in the vicinity of the switch. Also, for the vertical monocone configurations (88-ohm and 125-ohm), there appears to be evidence indicating that diffraction from the geometric discontinuity at the bend between the cone and peaker directions may be a problem.

The sensor location most obviously effected by the early time degradation effects of diffraction is  $P_1$ . Diffracted fields arrive at this location at times on the rising incident waveform which cause severe degradation in pulse risetime as clearly evident in the data presented in Addendum 1. It should be pointed out here, also, that although Table D-10 does not indicate any diffraction effects at sensor location  $P_2$ , the presence of diffraction from the end of the output

transition in particular is quite probably a major contributor to the slow risetime observed at this sensor location. This is felt to be the case despite the fact that the diffraction signature from that interface cannot be extricated from the general waveform.

e. Risetime Considerations

Table D-11 summarizes the measured risetimes for the various configurations of the low voltage spring tests as a function of sensor location. All risetimes are given in nanoseconds and represent the time required for the pulses to rise from 10 percent of their maximum amplitude to 90 percent. A figure is referenced in column two of the table for each of the configurations.

1) Risetime Versus Configuration

Figure D-12 illustrates the dependence of the measured 10 to 90 percent risetime on the configuration of the test setup at each sensor location. The configuration numbers along the horizontal axis correspond to the number designations for the configurations listed in Table D-11.

This figure displays two definite groupings of data according to sensor location.  $P_\alpha$  and  $P_\beta$  both lie together for the most part well below the curves for  $P_1$  and  $P_2$ . The reason for this grouping is at once evident in that both  $P_\alpha$  and  $P_\beta$  lie within the confines of the geometry of the pulser module while  $P_1$  and  $P_2$  lie outside this geometry. The increased risetimes for the outer sensors over the inner sensors can be attributed to a combination of diffractive effects and the loss of some of the high frequency components of the pulse by radiation as the pulse progresses away from the switch. One explanation of the increased risetime at  $P_2$  over that of  $P_1$ , then, is simply that it is more distant and hence suffers more degradation in risetime due to radiation of the high frequency components.

2) Risetime Versus Sensor Location

The dependence of the measured 10 to 90 percent risetime on the sensor location for each of the configurations studied

TABLE D-11. SUMMARY OF RISETIME MEASUREMENT (10-90 PERCENT)

CONFIGURATION	REFERENCE FIGURE	RISE TIME (NANOSECONDS)			
		P <sub>A</sub>	P <sub>B</sub>	P <sub>1</sub>	P <sub>2</sub>
1 125 OHM MATCHED PLATE	D-2	3	4.8	16.5	16.5
2 2-1/2" ALUMINUM TUBES FOR PEAKERS LEVEL WITH BOTTOM OF OUTPUT TRANSITION	D-3	4	5.5	11.5	17.9
3 2-1/2" ALUMINUM TUBES FOR PEAKERS 1/4" BELOW BOTTOM OF OUTPUT TRANSITION	D-4	4.8	4.0	14.3	17.1
4 BICONIC	D-5	9.2	9.7	12.3	16.5
5 88 OHM MONOCONE VERTICAL	D-6	8.4	9.2	11.0	16.5
6 88 OHM MONOCONE TILTED	D-7	7.4	7.6	10.3	14.4
7 125 OHM MONOCONE VERTICAL	D-8	8.0	10.8	13.2	16.3
8 125 OHM MONOCONE TILTED	D-9	8.0	8.0	14.3	18.5

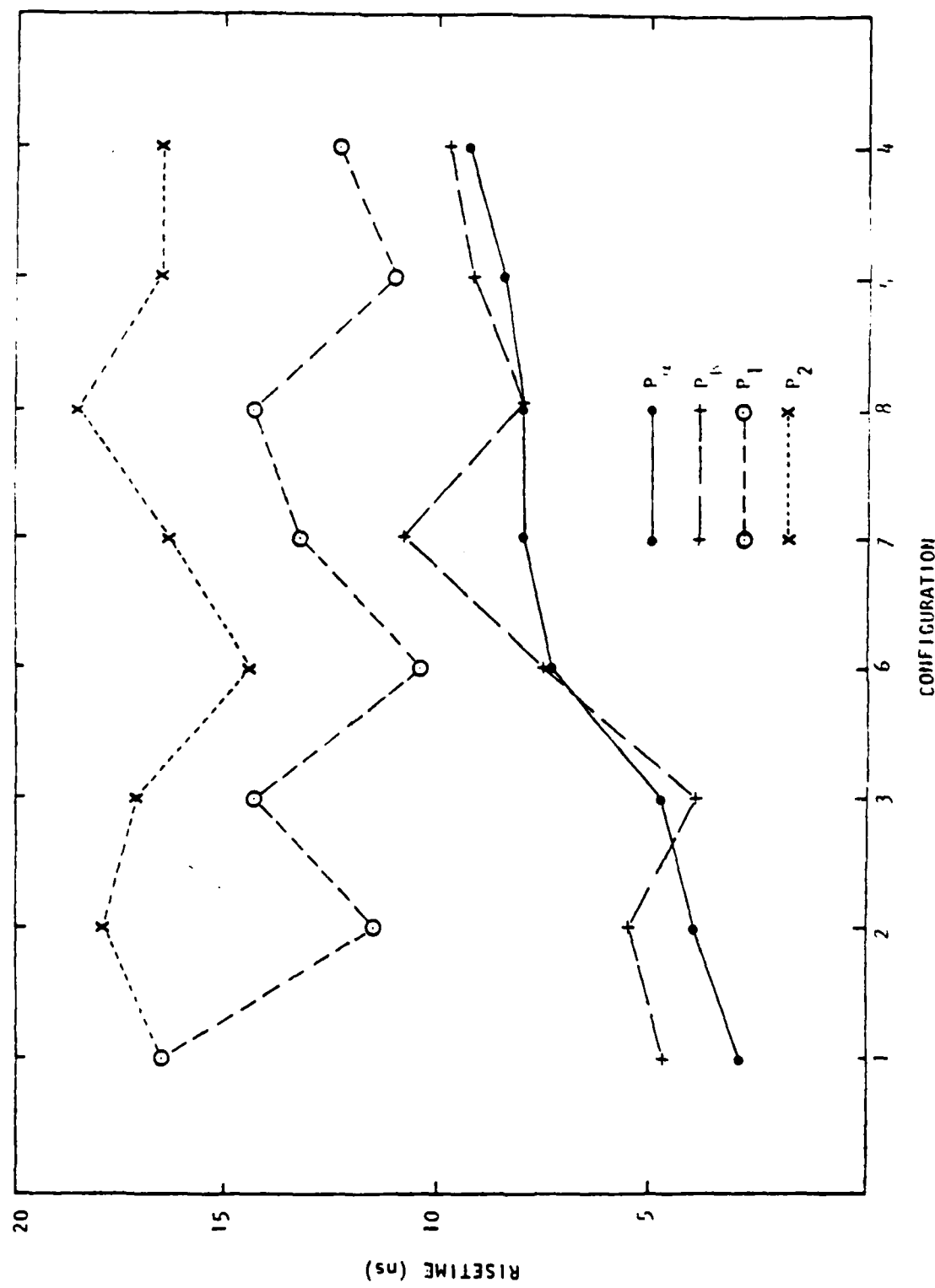


Figure D-12. Risetime versus configuration.

is illustrated in Figure D-13. The sensor locations are listed along the horizontal axis and the risetime in nanoseconds along the vertical. This figure illustrates quite clearly the trend for all configuration data toward increasing risetimes the further the sensor is from the pulse source. Again the probable cause for a large degree of this risetime degradation lies in diffraction from various interfaces although primarily it is in the interface between the output transition and the transmission line.

Notable here again is a definite grouping, particularly at the sensor locations  $P_A$  and  $P_B$ . The reason for this grouping is obvious, the three configurations in the lower group consists solely of "clean" geometry configurations, that is, all of the component elements lie primarily in a common plane along the same axis (125-ohm matched plane and aluminum tube configurations). The remaining configurations all consist of switches feeding either a bicone or monocone geometry, inherently a much more complex situation. The differences in risetime for these two groupings at sensor locations  $P_A$  and  $P_B$  can be attributed to some extent to differences in diffraction between the two basic geometries since any diffraction effects in the clean geometry cases is primarily observed only after the sensor at  $P_1$  is reached. However, it has been shown in a detailed analysis of the TRESTLE pulser at the PTF<sup>1</sup> that a more fundamental consideration enters into this difference. It was shown in the analysis that, independent of any diffraction effects, the simpler and smaller the output switch geometry the better the risetime. The differences in risetimes between a virtually ideal practical switch such as used in the "clean" geometry tests and a typical bicone or monocone was found to be approximately a factor of two.

Another feature worthy of note in Figure D-13 is the rapid risetime degradation in the "clean" geometry configurations in going from sensor location  $P_B$  to  $P_1$ . It is felt that a virtually complete explanation of this effect lies in the apparent large amount of diffraction occurring at the output transition/transmission line interface.

---

<sup>1</sup>Fisher, R. TRESTLE Pulser Analysis Final Report, BDM/A-27-75-TR, 1975.

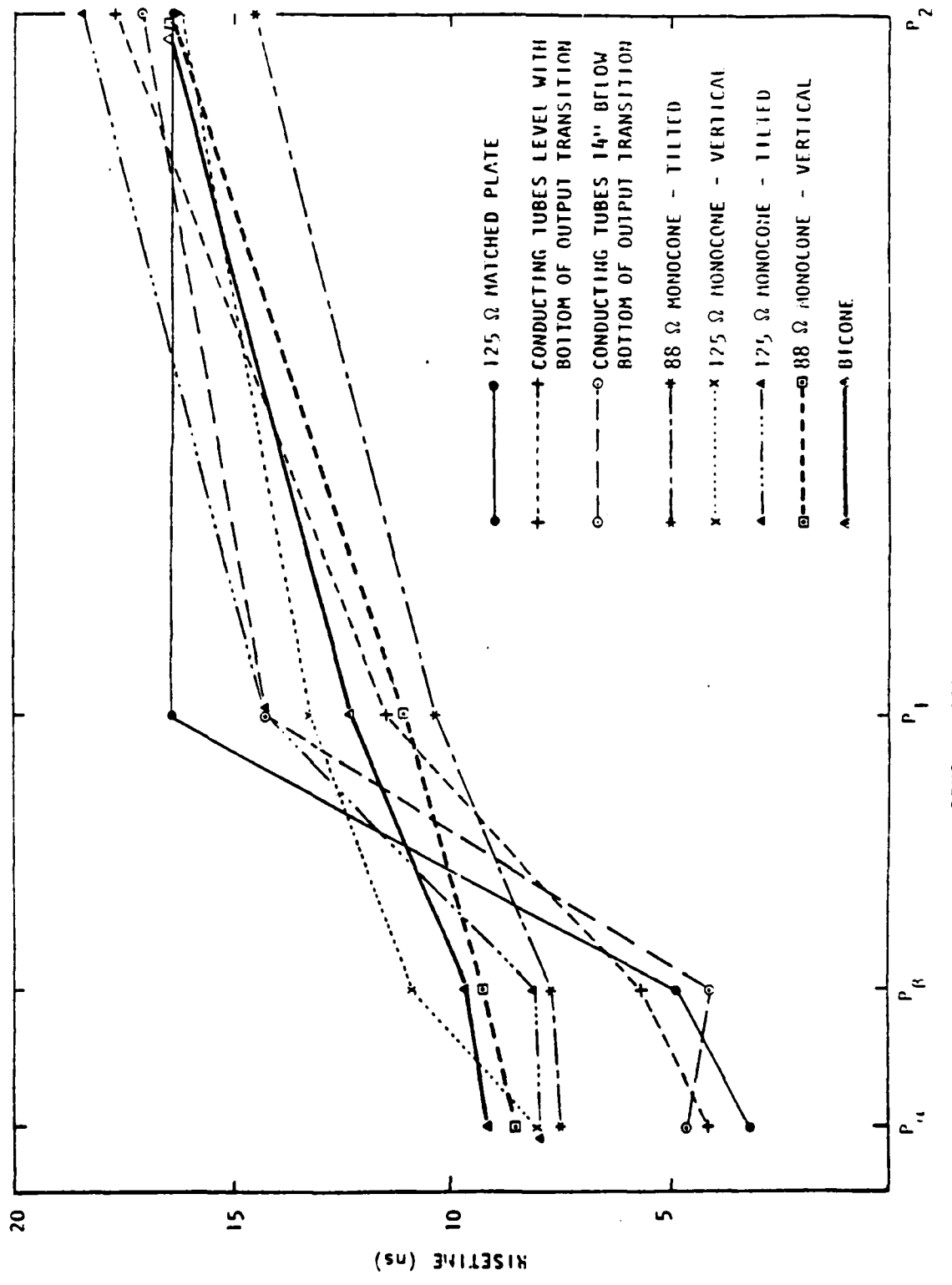


Figure D-13. Risetime versus sensor location.

Consideration of Figure D-13 in detail shows that, as far as risetime is concerned, the best two candidates for minimizing risetime of the cone geometries studied are the 88-ohms tilted monocone and the 88-ohm vertical monocone. The tilted geometry is only marginally superior to that of the vertical. The "clean" geometry configurations were discarded in this inspection of the figure since it is the realistically applicable switch geometries (cones) that are of interest in selecting the optimum switch for the pulser.

#### E. SUMMARY, CONCLUSIONS, AND RECOMMENDATIONS

##### 1. Summary

In summary:

- (1) The 125-ohm matched plate test indicates that risetime is degraded to 17 nanoseconds in the PTF with a 3-nanosecond switch risetime.
- (2) There is little difference in risetime or waveform perturbations between the two peaker configuration tests.
- (3) The monocone risetimes are superior to that of the 125-ohm bicone.
- (4) The 88-ohm monocone tests gave better risetimes than the 125-ohm monocone tests.
- (5) The tilted 88-ohm monocone risetime was slightly superior to that of the 88-ohm vertical monocone. The evidence was opposite for the 125-ohm monocone.

##### 2. Conclusions and Recommendations

Conclusions and recommendations are:

- (1) There is almost a zero probability of measuring a risetime less than 10 nanoseconds in the PTF working volume at positions  $P_1$  and  $P_2$ . This limitation is apparently due to the geometry of the PTF.
- (2) It is the judgment of the authors that less than 10 nanosecond risetimes in the Horizontal TRESTLE are impossible to achieve. The geometry of the PTF is similar to that

of the Horizontal TRESTLE. In addition, the Horizontal TRESTLE has additional mechanisms that could degrade the risetime further.

- (3) There is no apparent advantage in lowering the peakers below the plane of the bottom of the output transition. Simple theory indicates that lowering the peakers will reduce impedance mismatch. However, experimental data at  $P_1$  and  $P_2$  shows little or no sensitivity on risetime or other significant waveform parameters to this variation. Furthermore, a lowering of peakers is undesirable from a corona enhancement consideration. Therefore an approximate flush mounted peaker configuration is desired.
- (4) The bicone switch should be replaced by a monocone switch to improve risetime and to reduce reflections.
- (5) The 88-ohm monocone is preferred over a 125-ohm model due to superior risetime performance. This is fortunate since the 88-ohm model can use the existing switch pressure housing.
- (6) The difference in risetime between the vertical and tilted 88-ohm monocones is small. Since the vertical cone is easier to fabricate, it is preferred over the tilted cone model.

